

Western  Graduate&PostdoctoralStudies

Western University
Scholarship@Western

Electronic Thesis and Dissertation Repository

12-15-2010 12:00 AM


Mapping the Flip Angle in Magnetic Resonance Imaging Using the Accelerated 3D Look-Locker Sequence

Trevor P. Wade
The University of Western Ontario

Supervisor
Dr Brian Rutt
The University of Western Ontario

Graduate Program in Biomedical Engineering
A thesis submitted in partial fulfillment of the requirements for the degree in Doctor of Philosophy
© Trevor P. Wade 2010

Follow this and additional works at: <https://ir.lib.uwo.ca/etd>

 Part of the [Analytical, Diagnostic and Therapeutic Techniques and Equipment Commons](#), and the [Biomedical Engineering and Bioengineering Commons](#)

Recommended Citation

Wade, Trevor P., "Mapping the Flip Angle in Magnetic Resonance Imaging Using the Accelerated 3D Look-Locker Sequence" (2010). *Electronic Thesis and Dissertation Repository*. 73.
<https://ir.lib.uwo.ca/etd/73>

This Dissertation/Thesis is brought to you for free and open access by Scholarship@Western. It has been accepted for inclusion in Electronic Thesis and Dissertation Repository by an authorized administrator of Scholarship@Western. For more information, please contact wlsadmin@uwo.ca.

**Mapping the Flip Angle in Magnetic Resonance Imaging Using the
Accelerated 3D Look-Locker Sequence**

(Spine title: Flip Angle Mapping Using Accelerated 3D Look-Locker)

(Thesis format: Integrated article)

by

Trevor P. Wade

Biomedical Engineering Graduate Program

Submitted in partial fulfillment
of the requirements for the degree of
Doctor of Philosophy

The School of Graduate and Postdoctoral Studies
The University of Western Ontario
London, Ontario, Canada

December 2010

© Trevor P. Wade, 2010

THE UNIVERSITY OF WESTERN ONTARIO
School of Graduate and Postdoctoral Studies

CERTIFICATE OF EXAMINATION

Supervisor

Examining Board

Dr. Brian K. Rutt

Dr. Giles E. Santyr

Advisory Committee

Dr. Jean Theberge

Dr. Blaine A. Chronik

Dr. Terry M. Peters

Dr. Charles A. McKenzie

Dr. Greg Stanisz

Dr. Giles E. Santyr

The thesis by

Trevor P. Wade

entitled

**Mapping the Flip Angle in Magnetic Resonance Imaging Using the
Accelerated 3D Look-Locker Sequence**

is accepted in partial fulfillment of the
requirements for the degree of
Doctor of Philosophy

Date: _____

Chair of the Thesis Examination Board

Abstract

In the ongoing quest to extract more information from MRI images, there has arisen a need to rapidly map the flip angle. This has been primarily driven by the shift to stronger main field strengths, which bring with them improved SNR, but also new difficulties. In particular, the radio frequency field used to excite the magnetization can no longer be assumed uniform at field strengths of 3 Tesla and above. New rapid quantitative imaging techniques, such as DESPOT1 and DESPOT2, rely on accurate knowledge of the flip angle, and while this could safely be assumed to be the prescribed value at 1.5 Tesla, the same can no longer be said at 3 Tesla and above.

In this thesis, a new technique for mapping the flip angle in 3D will be introduced. This technique is based on a highly time efficient T_1 mapping technique, known as Look-Locker, which was adapted to map the flip angle using either a double angle (DALL) or dual repetition time (D τ LL) approach. The technique introduced is capable of producing 3D maps of the flip angle in less than one minute.

As part of the development of this flip angle mapping technique, a theoretical framework was developed to allow the optimization of the imaging parameters to achieve the best possible measurement of the flip angle. This framework also made it possible to compare the performance of the Look-Locker approaches to other techniques currently in use, which confirmed that, for imaging times less than one minute, the Look-Locker approach was optimal.

This fast imaging led to the development of a new approach to spoiling. While conventional spoiling approaches are optimized for imaging in the steady-state, they can lead to significant errors and artefacts if used when sampling the transients of the Look-Locker method, especially with the short repetition times and large flip angles used. A newly developed spoiling technique using randomized RF phase and gradient crusher amplitudes was shown to significantly reduce the deviations from ideally spoiled transients, and thereby reduce the errors associated with the quantitative values derived from them.

Key words: magnetic resonance imaging, B1+ mapping, radiofrequency field, flip angle, high field imaging, RF spoiling, random spoiling, optimization, efficiency

Dedicated to

Audrey and Thomas

may you never tire of looking under stones

Acknowledgments

Four years ago (and a few months, but who's counting) I had an idea, an encouraging wife and a brilliant supervisor, Brian Rutt, so I started a PhD. Through the passing years, life got a little more complicated. The idea took on a life of its own, my wife and I had two children, and Brian moved to the other side of the continent. It is thanks to the dedication and support of these people and many more that I made it to this point.

The Rutt lab was a diverse bunch. There was always something interesting developing in either the “soft” or the “hard” science group. Somehow we all managed to get together in one group meeting and learn something from each other. This trend has continued in my adoptive group, the McKenzie Mob, who continue to expand my horizons.

Of course there were lots of others along the way. Diana Timmermans for making sure I got paid on time. Jeff Stainsby, thank you (I think) for trying to teach me EPIC. Paco for tolerating me when I muttered and grumbled while trying to program in EPIC. Lanette for proofreading, and thoughts of the day. Cyndi for putting up with us all when we broke the scanner.

An accessible supervisor is crucial to the successful completion of a PhD. Brian, even though you moved to a new position two years ago, you were always available and interested. Your thirst for knowledge and enthusiasm for exploring new ideas are truly inspiring. Charlie, thank you for filling in for Brian when the distance was just too great and making sure the ball kept rolling.

I certainly wouldn't be the person I am today without the support of my family. My parents who encouraged me to explore the world, and always believed in me. My wife, Tara, thank you for everything.

Contents

Certificate of Examination	ii
Abstract	iii
Acknowledgements	vi
List of Tables	xi
List of Figures	xii
List of Symbols	xvii
List of Acronyms & Abbreviations	xix
1 Introduction	1
1.1 Nuclear Magnetic Resonance	4
1.2 Radio Frequency Pulses	6
1.3 Conventional B_1^+ Mapping Techniques	8
1.3.1 Multi-Point Intensity Methods	9
1.3.2 Stimulated Echo Ratios	11
1.3.3 Double Angle Methods	12
1.3.4 Phase Based Methods	13
1.3.5 Interleaved Delay and Actual Flip Angle Mapping	15
1.4 Look-Locker	17
1.5 Spoiling	20
1.6 Thesis Outline	22
1.6.1 Chapter 2: Flip Angle Mapping With the Accelerated 3D Look-Locker Sequence	23
1.6.2 Chapter 3: Optimizing the Efficiency of Flip Angle Mapping Techniques	24
1.6.3 Chapter 4: Spoiling for Accelerated 3D Look-Locker Acquisitions	25
1.6.4 Appendix A: Error Propagation	26

1.6.5	Co-Authorship	26
	References	28
2	Flip Angle Mapping With the Accelerated 3D Look-Locker Sequence	33
	Abstract	34
2.1	Introduction	35
2.2	Theory	38
2.2.1	Double Angle Look-Locker (DALL)	39
2.2.2	Interleaved Inverted DALL (intDALL)	40
2.2.3	Interleaved Non-Inverted Look-Locker (niDALL)	41
2.2.4	Dual τ Look-Locker (D τ LL)	42
2.2.5	Summary of Look-Locker Acquisition Schemes	42
2.3	Methods	43
2.3.1	Validation	44
2.3.2	Slab Selection	44
2.3.3	T_1 Correction	45
2.4	Results	46
2.4.1	The Phantom	46
2.4.2	Transients	48
2.4.3	Accuracy	50
2.4.4	Slab Selection	50
2.4.5	T_1 Correction	52
2.5	Discussion	54
2.6	Conclusion	56
	References	57
3	Optimizing the Efficiency of Flip Angle Mapping Techniques	60
	Abstract	61
3.1	Introduction	62
3.2	Theory	64
3.2.1	DAM Efficiency	66
3.2.2	AFI Efficiency	67
3.2.3	Double Angle Look-Locker	68
3.2.4	Dual τ Look-Locker	74
3.3	Methods	75
3.4	Results	76
3.4.1	Double Angle Method Optimization	76
3.4.2	AFI Optimization	77
3.4.3	Double Angle Look-Locker Optimization	80
3.4.4	Optimizing the Number of Effective TI Images	83

3.4.5	T_1 Sensitivity	85
3.4.6	Practical Scan Time	86
3.4.7	Experimental Validation	89
3.5	Discussion	90
3.6	Conclusion	94
3.7	Appendix	94
3.7.1	DAM	95
3.7.2	AFI	95
3.7.3	DALL	96
	References	98
4	Spoiling for Accelerated 3D Look-Locker Acquisitions	101
	Abstract	102
4.1	Introduction	103
4.2	Theory	105
4.3	Materials and Methods	107
4.3.1	Simulation	107
4.3.2	Experimental	108
4.3.3	Theoretical PSF	109
4.3.4	Quantitative Imaging	110
4.4	Results	111
4.4.1	Optimal Spoiler Gradient	111
4.4.2	Validation	113
4.4.3	PSF	117
4.4.4	T_1^* Error	120
4.5	Discussion	126
4.6	Conclusion	126
	References	128
5	Discussion and Future Work	131
5.1	Thesis Summary	131
5.2	Limitations of Developed Methods	134
5.2.1	Diffusion and Spoiling	134
5.2.2	RF Amplifier Drift	135
5.3	Future Research and Applications	136
5.3.1	Hyperpolarized Media T_1 Quantification	136
5.3.2	B_1^+ Shimming	139
	References	140

A	Error Propagation	142
A.1	Double Angle Method	143
A.2	AFI	144
A.3	Error Matrix	146
A.4	Double Angle Look-Locker	147
A.5	Dual τ Look-Locker	149
A.6	Interleaved, Non-Inverted DALL	150
	References	154
B	Ethics Approval	155
	Vita	157

List of Tables

1.1	RF wavelength in tissue (grey matter) at typical imaging strengths [1,4].	2
2.1	Acquisition schemes for the different Look-Locker approaches to flip angle mapping, with the parameters that are required in the non-linear least squares fitting of the transients.	43
3.1	Optimum imaging parameters for the various DALL flip angle mapping techniques.	83
4.1	Error between experimental samples and theoretically ideally spoiled samples for quadratically spoiled and randomly spoiled transients. Only the first 64 samples were used to highlight the errors during the transient phase.	116
4.2	Relaxation times (in ms) and errors (also in ms) measured using the accelerated 3D Look-Locker technique with $\alpha = 15^\circ$, spoiled either quadratically or randomly.	124
4.3	Relaxation times (in ms) and errors (also in ms) measured using the accelerated 3D Look-Locker technique with $\alpha = 30^\circ$, spoiled either quadratically or randomly.	124
5.1	Results of fitting hyperpolarized carbon-13 Look-Locker decay curve either with a mono-exponential curve, or using Bloch simulations. . .	138

List of Figures

1.1	(a) The laboratory frame of reference (x, y, z) and a frame of reference rotating at the Larmor frequency (x', y', z') , and (b) the precession of \mathbf{M} about \mathbf{B}_1 in the rotating reference frame.	7
1.2	Timing diagram of the stimulated echo acquisition.	11
1.3	Timing diagram of the saturated double angle method.	12
1.4	Pulse sequence for mapping the flip angle based on a composite pulse.	15
1.5	Off resonance pulse used in the Bloch-Siegert B_1 mapping technique.	15
1.6	Timing diagram of the AFI pulse sequence.	16
1.7	Timing diagram of the conventional Look-Locker acquisition. An image is created for each α sampling pulse.	18
1.8	Timing diagram of the accelerated 3D Look-Locker sequence. N_α pulses along the recovery train are segmented into N_{TI} effective TI volumes.	19
2.1	Cross section of the phantom containing multiple T_1 samples. (a) T_1 map in ms based on the 2D IR FSE images. (b) and (c) are the $T_{1,1\alpha}^*$ and $T_{1,2\alpha}^*$ maps in ms from fitting transients to the accelerated 3D Look-Locker acquisitions. (d) is the result of combining the $T_{1,1\alpha}^*$ and $T_{1,2\alpha}^*$ maps to form a flip angle map (α/α_{nom} with $\alpha_{nom} = 6^\circ$). (e) is a flip angle map using the AFI technique (α/α_{nom} with $\alpha_{nom} = 60^\circ$).	47
2.2	The transients measured in a sample with $T_1 = 740$ ms for the (a) DALL, (b) interleaved DALL, (c) non-inverted DALL and (d) $D\tau$ LL flip angle mapping techniques. The nominal 1α flip angle was 6° . Solid lines are the curves fit to the data points in the flip angle analysis.	49
2.3	The accuracy of the Look-Locker based flip angle mapping techniques for T_1 values ranging from 271 to 2952 ms. (a) is the standard DALL implementation, (b) is the interleaved DALL, (c) is non inverted DALL using reduced parameter fitting, and (d) is an interleaved $D\tau$ LL approach.	51

2.4	Sensitivity of DALL method to slab selective pulses. (a) shows an image of the flip angle in degrees across the slab excited with the 10kHz bandwidth pulse. Despite the phantom extending outside the imaged slab, only the excited slab is visible. (b) the experimentally measured slab profile matches the theoretical slab profile.	52
2.5	Flip angle maps for a sagittal (top row) and axial (bottom row) in the head at 3T. From left to right the methods of acquisition are intDALL, niDALL, D τ LL and AFI. Units are α/α_{nom}	53
2.6	Sagittal (top row) and axial (bottom row) T_1 and flip angle maps in the head. The left column contains T_1 maps constructed assuming the nominal flip angles throughout the head. The middle column is the flip angle for the corresponding slices, and the right column is the flip angle corrected T_1 map. Units in ms for T_1 maps and α/α_{nom} for flip angle.	54
2.7	Sources of error in Look-Locker fitting. (a) Transient acquired with reduced B_1^+ ($\alpha = 2^\circ$) in a sample with $T_1 = 740$ ms. The reduced B_1^+ prevents complete inversion, and the TI points only sample a portion of recovery curve. (b) Transient acquired assuming large B_1^+ ($\alpha = 20^\circ$) in saline. The inversion pulse is effective, however, much of the exponential decay is complete by the second TI	55
3.1	Optimum efficiency (in $s^{-1/2}$) available using the double angle methods. (a) Efficiency at different recovery times for the saturated DAM and (b) the optimized efficiency of the saturated DAM compared to conventional DAM.	77
3.2	Efficiency of AFI with n optimized. (a) Efficiency (Γ in $s^{-1/2}$) at different values of T_{seq} and α with n optimized for each combination, and (b) the error ($(\alpha_{AFI} - \alpha)/\alpha$) associated with the optimum efficiency).	78
3.3	(a) Efficiency and (b) error of the AFI technique as a function of n , with $T_{seq} = 1.3T_1$. Low flip angles ($< 90^\circ$) are optimized when n is maximized. At higher flip angles this behavior changes.	79
3.4	Optimal flip angle mapping efficiency (in $s^{-1/2}$) achievable using the accelerated 3D Look-Locker sequence for different repetition time, and flip angle combinations. (a) efficiency based on a sequential acquisition of α and 2α , (b) interleaved DALL, (c) non-inverted DALL, fitting reduced parameter set, and (d) interleaved D τ LL acquisition.	81
3.5	The best efficiency of the Look-Locker based methods achievable at each flip angle, assuming all other parameters are optimized for that flip angle.	82

3.6	Parameters required to optimize the niDALL method. (a) The optimum repetition time is lower with decreasing flip angle. (b) Lower flip angles with correspondingly shorter repetition times require longer read-out trains. (c) The ratio of the flip angle to the Ernst angle based on optimum efficiency at that angle is relatively constant, as is (d) the time taken for the read-out train relative to the T_1^* for that angle. . .	84
3.7	Effect of the number of effective TI images on the flip angle mapping efficiency of Look-Locker methods with τ set to 3.7 ms. (a) Efficiency is independent of N_{TI} above a certain threshold as the additional TI volumes behave like averages N_α and α are fixed. (b) The additional TI volumes lead to a broader flip angle sensitivity with N_α fixed. . .	85
3.8	Efficiency (in $s^{-1/2}$) of the niDALL technique optimized for a T_1 of 1500 ms over a range of T_1 and flip angle values ($\tau = 3.7$ ms, $N_{TI} = 8$, $N_\alpha = 328$).	86
3.9	Optimized efficiency as a function of restricted effective sequence time for the niDALL, AFI and satDAM flip angle mapping techniques. . .	87
3.10	Efficiency of flip angle mapping techniques with a scan time limited to one minute for (a) the DALL techniques, and (b) the AFI and DAM techniques.	88
3.11	Effect of EPI acceleration on the efficiency of the (a) satDAM and (b) AFI methods.	89
3.12	Noise properties of the AFI and niDALL techniques. (a) AFI flip angle map (α/α_{nom}) with $\alpha_{nom} = 120^\circ$, and $TR_1/TR_2 = 5/55$ ms (b) ANR map of (a). (c) niDALL flip angle with $\alpha_{nom} = 6^\circ$ and $\tau = 3.7ms$ and (d) the ANR map of the niDALL image.	91
3.13	Performance of the AFI and non-inverted DALL techniques. (a) shows the ANR for a range of T_1 values is ms, and (b) shows the bias in the measurement. (c) is the ANR for the niDALL technique, and (d) is the bias in the niDALL flip angle measurement. Lines are the ANR predicted by propagation of noise.	92
4.1	The steps used to determine sources of artefact in simulated accelerated 3D Look-Locker acquisitions. A point is represented by a constant in k-space. This is modulated by sampling along the transient, and any fluctuations from the transient caused by imperfect spoiling, resulting in the distorted image of the point.	110
4.2	Root mean square error between ideally spoiled and simulated transient. Shown are the conventional quadratic spoiling, random phase with fixed crusher, and random phase with crushers randomized over different intervals. 64 samples post inversion, $\tau = 3.5$ ms, $T_1/T_2 = 2000/200$ ms. Ranges shown are a fraction of C_{max}	112

4.3	Bloch simulations and experimental data for approach to steady-state employing quadratic or random spoiling schemes. (a and b) Real and imaginary components respectively of the signal for a transient acquired using quadratic spoiling and a small amplitude crusher (2 cycles/voxel) and a $\phi_{seed} = 84^\circ$. (c and d) Real and imaginary signal for a transient acquired using random phase and crusher gradients randomized over interval [10,20] cycles/voxel. The standard deviation in the transient points is 0.0042 for quadratic spoiling and 0.021 for the random spoiling.	114
4.4	Noise and diffusion effects on spoiling. (a) error properties of random and quadratic spoiling for sample 23. (b) Effect of increasing the crusher amplitude to 15 cycles/voxel in the quadratic spoiling case. .	116
4.5	Effective TI magnitude images of the CuSO ₄ phantom. Top row (a,b,c) are images using quadratic sampling for the first, third and eighth effective TI image respectively. Bottom row (d,e,f) are images based on random spoiling for the same effective TI values as the above quadratically spoiled images. The first TI images are scaled by 1/6th but the third and eighth have same window and level.	118
4.6	ky-kz space modulation (magnitude) due to a centric accelerated 3D Look-Locker acquisition for the first TI volume. (a) K-space filled with signal equal to the first post-inversion sample. (b) Modulation due to transient, $(M_{trans}(k_y, k_z) / M_{trans}(0, 0))$. (c) Modulation due to spoiling, $(M_{spoil}(k_y, k_z) / M_{trans}(k_y, k_z))$. (d) Combined effect of (b) and (c) on (a). The modulation of k-space due the transient and spoiling lead to the 2D PSFs shown in (e) and (f) respectively.	119
4.7	Point spread function indicating sources of error and artefact in accelerated 3D Look-Locker acquisitions. (a) The PSF due to transient effects alone for the first and last effective TI image. (b) The PSF due to spoiling effects for the first effective TI image, (c) for the third effective TI image, and (d) for the last effective TI image.	121
4.8	Effective TI images from a transient sampled with $N_\alpha = 48$, 15° segmented into 8 effective TI volumes. (a) and (b) are the first and last effective TI images using quadratic spoiling respectively, while (c) and (d) are the same, but randomly spoiled.	122
4.9	T_1^* maps (in ms) of the multi- T_1 phantom. (a) and (b) are derived from images spoiled using quadratic spoiling after (a) 1 Nex and (b) 20 Nex. (c) and (d) are based on images spoiled using random spoiling.	123
4.10	Flip angle measurement based on the DALL approach. (a) is the flip angle measured using quadratic spoiling and (b) is the mean absolute error. (c) and (d) respectively are the flip angle map and error respectively based on random spoiling. Units are degrees in the range $[10^\circ - 20^\circ]$ for flip angle maps and $[0^\circ - 5^\circ]$ for errors.	125

5.1 Carbon-13 Look-Locker transient and the results from two fitting approaches. (a) With a mono-exponential fit to the experimental data points, significant deviations from the model still remain. (b) The residuals after fitting either with a mono-exponential fit or based on Bloch simulations and assuming no spoiling of the transverse magnetization. 138

List of Symbols

α	Flip angle
α_{nom}	Nominal (or prescribed) flip angle
b	Dimensionless noise propagation factor
B_0	Main static magnetic field
B_1^{eff}	Effective amplitude of Bloch-Siegert RF pulse
B_1^+	Circularly polarized magnetic field of RF pulse
E_1	$\exp(-TR/T_1)$
E_Δ	DALL T_1^* difference exponential
E_Λ	D τ LL T_1^* difference exponential
E_τ	$\exp(-\tau/T_1)$
γ	Gyromagnetic ratio
Γ	Flip angle imaging efficiency ($\text{ANR}/\sqrt{T_{exam}}$)
k	α/α_{nom}
M_0	Equilibrium magnetization
M_{xy}	Transverse magnetization
M_z	Longitudinal magnetization
n	Repetition time ratio (TR_2/TR_1) or (τ_2/τ_1)
N_α	Number of α pulses in Look-Locker sampling train
N_{ex}	Number of averages
N_{TI}	Number of effective TI volumes
ϕ	Phase of radio frequency pulse

ϕ_{seed}	Quadratic phase increase
r	AFI signal ratio (S_2/S_1)
τ	Repetition time of the α pulses in LL sampling train
t_d	Time between inversion and first α pulse in LL sampling train
t_r	Time between last α pulse and next inversion in LL sampling train
T_1	Longitudinal recovery constant
T_1^*	Driven longitudinal LL recovery constant
T_{exam}	Total sequence scan time
T_{seq}	Effective sequence repetition time
TI	Inversion time
TR	Repetition time
TR_1, TR_2	Interleaved repetition times in AFI
T_{SR}	Time after saturation pulse
ω_{RF}	Frequency of RF pulse

List of Acronyms & Abbreviations

3D	Three dimensional
2D	Two dimensional
a.u.	Arbitrary units
AFI	Actual flip angle imaging
ANR	Flip angle to flip angle noise ratio
BW	Acquisition bandwidth
DALL	Double angle Look-Locker
DAM	Double angle method
DESPOT1	Driven equilibrium single pulse observation of T_1
DESPOT2	Driven equilibrium single pulse observation of T_2
D τ LL	Dual repetition time Look-Locker
FID	Free induction decay
FOV	Field of view
FSE	Fast spin echo
GRE	Gradient recalled echo
intDALL	Interleaved inverted DALL
LL	Look-Locker
MRI	Magnetic resonance imaging
niDALL	Interleaved non-inverted DALL
PSF	Point spread function
RF	Radio frequency

RMSE	Root mean square error
ROI	Region of interest
satDAM	Saturated DAM
SAR	Specific absorption rate
SE	Spin echo
SNR	Signal to signal noise ratio
SPGR	Spoiled gradient recalled echo
SSFP	Steady-state free precession
STE	Stimulated echo
T	Tesla

Chapter 1

Introduction

Magnetic resonance imaging (MRI) has proven to be a very useful medical imaging technique largely due to its excellent contrast to noise properties. The same equipment, with only a change in the software control can be tuned to image a wide range of physical properties, such as proton density, diffusion or the time constants T_1 , T_2 , or T_2^* to name just a few. Thus, while MRI may not have the signal to noise (SNR) of computed tomography, it is none-the-less a highly adaptable and useful technique as it is possible to isolate a single tissue parameter of interest, especially in soft tissue.

An MRI scanner relies on a large, uniform magnetic field to polarize nuclear magnetic spins. The polarization of the sample is proportional to the main magnetic field strength and this leads to a signal to noise ratio increase that is approximately linear with the main magnetic field [1]. This has led to a constant push to stronger main magnets, allowing for improvements in SNR to be traded off for higher resolution images and/or shorter scan times.

In their equilibrium state, the nuclear spins produce no detectable signal. Images are produced by interacting with these spins using radio frequency (RF) coils. The transmit coils produce a time varying magnetic field, B_1^+ , perpendicular to the main field that tips the magnetization away from the equilibrium state by a flip angle, α . The signal can then be read by the same or another set of RF coils to produce the

images.

The RF coils used to excite the magnetization in the sample are generally designed to produce a uniform excitation field. This makes interpretation of qualitative and quantitative images straightforward. At low field strengths, producing a uniform excitation field is possible, as the wavelength of the RF field in tissue is significantly longer than the scale of the object being imaged, as indicated by Table 1.1. Difficulties are encountered at high field strengths because, not only does the polarization increase with field strength, but so too does the frequency used to interrogate the sample. This leads to a decrease in wavelength, and destructive interference from different elements in the excitation coil, leading to a non-uniform excitation at higher field strengths [2, 3]. For field strengths up to 3 Tesla, the excitation field can usually be assumed uniform for a wide range of applications. At 3 Tesla, though, the non-uniformity begins to reach unacceptable levels, especially for quantitative imaging techniques, and above 3 Tesla, it is essential to find some way to mitigate the non-uniform excitation.

Field Strength (T)	Wavelength	
	Air (cm)	Tissue (cm)
1.5	468	40
3.0	234	25
7.0	100	12

Table 1.1: RF wavelength in tissue (grey matter) at typical imaging strengths [1, 4].

This problem is not unique to high fields. A non-uniform excitation may arise due to use of a non-uniform excitation coil, for example when a surface coil is used for transmission. Even if the B_1^+ field is uniform, slice and slab selective pulses are generally not capable of perfectly uniform excitation. The artefact has often been characterized as a dielectric resonance phenomena. In samples with low conductivity, it is possible to set up standing waves leading to non-uniform excitation, though these are typically damped out as the conductivity approaches values seen in tissue [5].

There are two general approaches to mitigating the effects of the non-uniform transmit field. First, particularly if the non-uniformity is not too great, the spatially varying flip angle may be mapped. This measurement of the artefact can then be used to correct qualitative or quantitative images. Second, attempts can be made to flatten the transmit B_1^+ field. This requires that a map of B_1^+ field of the transmit coil or coils be made, and then spatially selective pulses are applied to compensate for the non-uniformity [6]. These shaped pulses typically require longer RF pulses with a higher specific absorption rate (SAR), and are only effective provided the B_1^+ field is still relatively uniform and non-zero in the volume of interest. Some of these limitations may be overcome by using B_1^+ shimming [7,8], where the same pulse shape is applied to the different elements of the transmit coil, but with varying phase and/or amplitude. This approach can be further generalized by allowing the pulse shapes for each element to vary in a fully parallel excitation [9,10].

What both of the above approaches to the B_1^+ artefact have in common is a need to map the excitation field profile. Fortunately, this is typically a spatially very slowly changing feature, thus, a low resolution map of the flip angle is typically sufficient, but the existing techniques for mapping artefact are typically slow and thus unable to map in 3D in a reasonable scan time.

Most of the existing techniques are designed to map the flip angle, and not specifically the B_1^+ field, and depending on which correcting technique is used, either the flip angle or B_1^+ will be desired. However, these are related [11] so the two terms can be used interchangeably, and for the rest of this thesis we will focus on flip angle mapping. Also, many times only relative values are required, and so the scaling factor k is used [12,13]:

$$k = \frac{\alpha}{\alpha_{nom}} \quad (1.1)$$

In the second chapter a new technique for mapping the flip angle based on the accelerated 3D Look-Locker sequence is introduced. The Look-Locker technique has

proven to be a highly time efficient technique for mapping the T_1 of tissue and was adapted to map the flip angle. By using the accelerated 3D sequence it is possible to acquire 3D volumes in a very quick acquisition.

In the third chapter, the Look-Locker techniques are optimized using a theoretical approach to assess the noise propagation into the flip angle maps. Two of the more common conventional approaches to mapping the flip angle are also investigated. This provides a theoretical basis from which to optimize and compare the techniques, especially for time constrained applications.

Paramount to the Look-Locker flip angle mapping technique, and most other rapid flip angle mapping techniques, is the assumption that the transverse magnetization is fully spoiled. Conventional spoiling techniques [14, 15] were designed for the steady-state, and do not have optimal properties for spoiling along the transient, as is required in the Look-Locker acquisition. A new approach based on random RF phase and magnetic field gradients [16] is adapted to the Look-Locker technique. Its effect on the resulting measurement of T_1^* and flip angle is investigated in Chapter 4, in addition to the effect of non-ideal spoiling and sampling along the transient to the point spread function (PSF).

1.1 Nuclear Magnetic Resonance

Nuclei possess a fundamental property known as spin. Associated with this spin is an angular momentum and a nuclear magnetic dipole moment:

$$\mu = \gamma \hbar I \tag{1.2}$$

where \hbar is Planck's constant divided by 2π , and γ is the gyromagnetic ratio. I is the spin quantum number, and its value is determined by the configuration of neutrons and protons into nuclear orbitals. Its value is $1/2$ for 1H and it is non-zero for nuclei with an odd number of protons and/or neutrons.

In diamagnetic matter, the individual nuclear magnetic dipole moments are usually randomly distributed, leading to no net magnetization. In the presence of an external magnetic field, \mathbf{B}_0 , however, the z component of the individual magnetic moments becomes quantized. This process is characterized by energy states aligned with or against the external field, with a preference for the lower energy state aligned with the external field. Energy from thermal collisions causes transitions between the energy states, resulting in a slightly larger population in the lower energy state, which manifests itself in bulk matter as a net magnetic moment, \mathbf{M} .

Just like a bar magnet or compass needle experiences a torque when placed in an external field, so too does the magnetic dipole moment, only the dipole moment also has an associated angular momentum. This torque induces the magnetic moment to precess about the external field at a frequency known as the Larmor frequency:

$$\omega = \gamma B_0 \quad (1.3)$$

where γ depends on the particular nucleus being studied. Hydrogen is the most commonly used nucleus for imaging largely because it is the most numerous in the body and produces the greatest signal. For ^1H , $\gamma = 2.675 \times 10^8 \text{s}^{-1}\text{T}^{-1}$. The value $\gamma = \gamma/(2\pi)$ is 42.57MHz/T is also commonly used.

In equilibrium, \mathbf{M} is aligned entirely along \mathbf{B}_0 . The $\hat{\mathbf{x}}$ and $\hat{\mathbf{y}}$ components of the individual nuclear magnetic moments are randomly distributed and cancel. If the bulk magnetization is tipped away from \mathbf{B}_0 , only then does the precession become evident. The transverse component lasts only a short time and decays to zero according to the time constant T_2 . At the same time, the longitudinal magnetization relaxes back to its equilibrium state along $\hat{\mathbf{z}}$. These processes are described by the Bloch equation [17]:

$$\frac{d\mathbf{M}}{dt} = \mathbf{M} \times \gamma \mathbf{B} - \frac{M_x \hat{\mathbf{x}} + M_y \hat{\mathbf{y}}}{T_2} - \frac{(M_z - M_0) \hat{\mathbf{z}}}{T_1} \quad (1.4)$$

The slowest process is the longitudinal relaxation, the restoration of the magnetization along $\hat{\mathbf{z}}$. It is a result of exchanges in energy between nuclei and the surrounding

lattice, which is enhanced by field fluctuations. Hence, the constant governing the return to equilibrium, T_1 , is known as the spin-lattice relaxation time constant.

Transverse relaxation results from the same processes as longitudinal relaxation, but in addition, fluctuations in the z component of the field due to interactions of the spins with each other may make this process faster than longitudinal relaxation, and the spin-spin time constant, T_2 , is less than or equal to T_1 .

1.2 Radio Frequency Pulses

So far the details of how the magnetization is tipped away from \mathbf{B}_0 have been left vague, and will be discussed in more detail here. Magnetic fields induce torques on magnetic moments. We can see this by looking at the Bloch equation. Neglecting the relaxation terms, it becomes:

$$\frac{d\mathbf{M}}{dt} = \mathbf{M} \times \gamma\mathbf{B} \quad (1.5)$$

This implies that \mathbf{M} can be forced away from its equilibrium position along \mathbf{B}_0 by applying an additional magnetic field, \mathbf{B}_1 , such that the total magnetic field is given by:

$$\mathbf{B} = \mathbf{B}_0 + \mathbf{B}_1 \quad (1.6)$$

This process is best understood by entering a reference frame rotating at the Larmor frequency as in Figure 1.1(a) In this reference frame, \mathbf{B}_0 can be neglected, leaving just \mathbf{B}_1 . If we choose to place \mathbf{B}_1 along the \mathbf{x}' direction, it becomes apparent that \mathbf{M} will precess about \mathbf{B}_1 with an angular frequency given by Equation 1.3 as in Figure 1.1(b). The angle through which it precesses, the tip angle, α , will then be determined by the magnitude of this RF pulse, B_1 , and its duration, τ_{RF} :

$$\alpha = \gamma B_1 \tau_{RF} \quad (1.7)$$

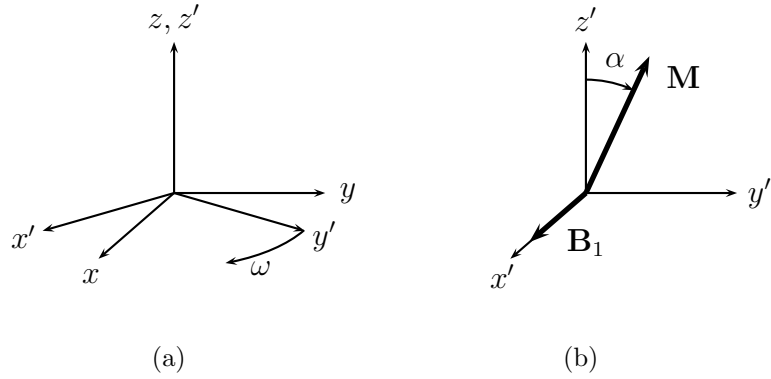


Figure 1.1: (a) The laboratory frame of reference (x, y, z) and a frame of reference rotating at the Larmor frequency (x', y', z') , and (b) the precession of \mathbf{M} about \mathbf{B}_1 in the rotating reference frame.

Since the signal produced depends on the transverse component of the magnetization, M_{xy} , the signal produced will be proportional to $\sin \alpha$.

Moving back to the laboratory frame, it becomes apparent that \mathbf{B}_1 is actually rotating about \mathbf{B}_0 at the Larmor frequency. This is a circularly polarized radio frequency (RF) pulse. In general, any RF pulse can be broken down into two counter rotating components, \mathbf{B}_1^+ which is rotating in the same direction as the precession and is responsible for exciting the magnetization, and \mathbf{B}_1^- rotating in the opposite direction which does not affect \mathbf{M} .

So far we have considered only a very simple pulse, a fixed amplitude, single frequency pulse known as a hard pulse. By combining gradients and RF pulses with a range of frequencies it is possible to create pulses capable of selecting an almost arbitrary pattern in the sample [11]. The most common application is for slice or slab selection, using sinc like shaped pulses with constant gradients. These however are sensitive to off-resonance effects and imperfections in the \mathbf{B}_1^+ field. These limitations have led to the development of adiabatic pulses that are relatively insensitive to these effects [18].

The relationship between the RF pulse shape and the resulting $M_{xy}(\mathbf{x})$ profile

in general requires numeric integration of the Bloch equation. By making a few assumptions, it can be shown that there is a Fourier relationship between an RF pulse, with duration T , and the profile created [11]:

$$M_{xy}(\mathbf{x}) = i\gamma M_0 \int_0^T B_1^+(t) e^{i\mathbf{x}\cdot\mathbf{k}(t)} dt \quad (1.8)$$

where $\mathbf{k}(t)$ is the trajectory through k-space determined by the gradient pulses:

$$\mathbf{k}(t) = -\gamma \int_t^T \mathbf{G}(s) ds \quad (1.9)$$

The above relationship is based on the assumption that the duration of the pulse is short relative to T_1 and T_2 , and thus the relaxation terms can be ignored in the Bloch equation. It is also based on the assumption that $M_z = M_0 = \text{constant}$ for the duration of the pulse. This is true for small tip angles, and hence is known as the *small tip angle assumption*. Remarkably, using the small tip angle assumption to find M_{xy} seems to work well up to 90° [11].

Since the transverse magnetization, M_{xy} , is produced from the initial magnetization, M_z , several features relevant to flip angle mapping can be gleaned from Equation 1.8. In the small tip angle assumption $\alpha \propto B_1^+$. Also the flip angle produced depends not only on B_1^+ , but also the spatially selective nature of the RF pulse.

1.3 Conventional B_1^+ Mapping Techniques

Techniques for mapping the the B_1^+ field can be classed broadly into image intensity based techniques, and phase based techniques [19–21]. The intensity based techniques in turn are either based on signal acquired from applications of a single pulse at different nominal amplitudes [12, 14, 22–26], or by comparing the intensities of stimulated echoes [22, 27, 28].

1.3.1 Multi-Point Intensity Methods

A conventional approach to setting the B_1^+ transmit amplitude is to use an RF pulse that excites a bulk sample and then acquire the free induction decay (FID) from the bulk sample. With a long repetition time ($TR \gg T_1$), the signal is largely independent of the relaxation times. This implies $S \propto \sin \alpha$. The transmit attenuation is then incremented to look for the first maximum in the signal which corresponds to a 90° pulse. Other pulse amplitudes and slice and slab selective pulses of different shape would then be set based on their amplitude relative to this calibration pulse. In sample, coil and pulse combinations that have a uniform excitation profile this can work quite well in setting the correct pulse amplitude to achieve the desired flip angles.

At larger fields, or using non-uniform transmit coils, and even using spatially selective pulses, the above procedure no longer works. The flip angle becomes spatially dependent. Ninety degrees will not be achieved throughout the sample at a single value of transmit attenuation. Instead the signal maximum corresponds to a global average signal where the flip angle is around 90° for much of the sample, but not necessarily 90° at any given point. This raises the need for a spatially sensitive method of measuring the flip angle.

The earliest spatially sensitive techniques were essentially extensions of the incremented approach used in the prescan to either gradient recalled echo (GRE) or spin echo (SE) imaging [22]. In the GRE sequence signal relative to the 90° maximum is given by:

$$\frac{S}{S_{max}} = \frac{B_1^+}{B_{1,max}^+} \sin(\gamma B_1^+ \tau) \quad (1.10)$$

In the SE sequence, signal will vary according to:

$$\frac{S}{S_{max}} = \frac{B_1^+}{B_{1,max}^+} \sin^3(\gamma B_1^+ \tau) \quad (1.11)$$

If the B_1^+ amplitude is incremented through a sufficiently large range, a spatial map of $B_{1,max}^+$ can be found and the relative local B_1^+ field found either using a look-up-table

approach based on Equations 1.10 or 1.11, or by fitting those equations to all points along the incremented flip angle calibration curve. The main disadvantage of these techniques is that they are inherently slow. To avoid T_1 bias, TR must be kept long relative to T_1 .

As repetition times become shorter, the signal can no longer be assumed independent of T_1 and TR , and is given by the spoiled, gradient recalled echo (SPGR) steady-state value:

$$\begin{aligned} S &\propto M_0 \sin \alpha \frac{1 - E_1}{1 - E_1 \cos \alpha} \\ E_1 &= \exp(-TR/T_1) \end{aligned} \quad (1.12)$$

This speed limitation inherent in the above technique can be partially overcome by focusing on the signal null at 180° [12]. Assuming there is no refocusing of the transverse magnetization, there will always be a signal null for a flip angle that produces a 180° pulse. Moreover, the signal curve is approximately linear with flip angle near the null. Thus the B_1^+ calibration factor, $k = 180^\circ/\alpha_{null}$, can be estimated with as little as two points.

Using the signal null as the calibration point does have its disadvantages. As TR/T_1 becomes short, the magnetization becomes saturated, leading to very little signal. In addition, stimulated echoes may start to contribute to the signal leading to a loss in accuracy. The technique also has limited dynamic range. It relies on signals in the linear region near the 180° null. Much away from this point and either more calibration points or a more complex fitting routine will be required. By the nature of the inversion pulse, it will also tend to be a high SAR technique. The technique will also have limited ability to measure slab profiles, as the profile at 180° is far from the small tip angle regime.

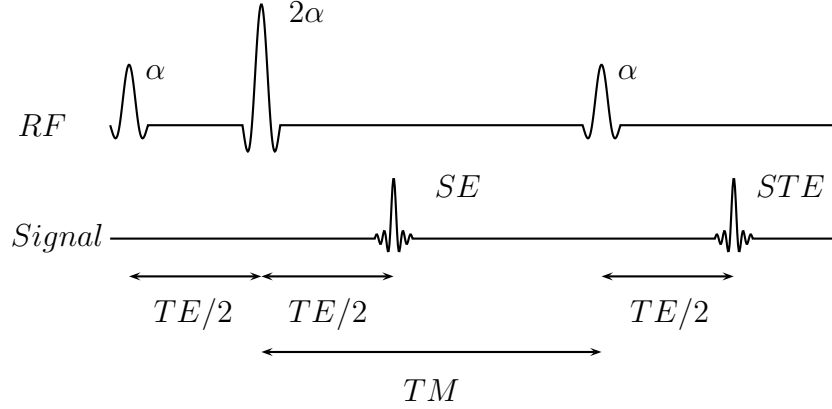


Figure 1.2: Timing diagram of the stimulated echo acquisition.

1.3.2 Stimulated Echo Ratios

In contrast to the above techniques that acquire a single echo from either a gradient echo or spin echo sequence using an incremented flip angle, it is possible to acquire multiple echoes from a train of RF pulses [27–29]. For a pulse sequence with RF pulses as shown in Figure 1.2, the first two echoes are the spin echo (SE) and stimulated echo (STE) respectively, and have amplitudes given by:

$$S_{SE} \propto \exp(-TE/T_2) \sin^3 \alpha \quad (1.13)$$

$$S_{STE} \propto 0.5 \exp(-TE/T_2) \exp(-TM/T_1) \sin^2 \alpha \sin(2\alpha) \quad (1.14)$$

Taking the ratio of the two echoes produces an expression for the flip angle:

$$\alpha = \arccos \left(\exp(TM/T_1) \frac{S_{STE}}{S_{SE}} \right) \quad (1.15)$$

Slice profile artefacts were identified as a potential source of error in the original implementation for α values greater than 100° [27]. By replacing the second and third pulses with non-selective pulses, this problem can be mitigated [28]. While the measured flip angle does not depend directly on the repetition time, TR must still be large enough to allow the transverse magnetization to decay, and M_z to recover,

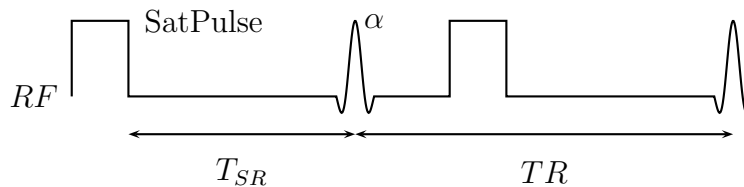


Figure 1.3: Timing diagram of the saturated double angle method.

restricting how quickly the sequence can be run. The flip angle is, however, influenced by TM . Either some assumption as to the tissue T_1 must be made (such as $TM \ll T_1$), leading to potential T_1 biases, or a T_1 map must be acquired to correct the flip angle.

1.3.3 Double Angle Methods

The incremented flip angle approach can be reduced to a two point method by making use of the of the trigonometric double angle formula and hence came to be known as the double angle method (DAM) [14, 22]. If a limited tip angle pulse of unknown excitation angle, α , is applied to a fully relaxed magnetization, the signal is given by:

$$S_1 \propto M_0 \sin \alpha \quad (1.16)$$

If the same experiment is repeated with twice the flip angle, $\alpha_2 = 2\alpha$, the signal in the second experiment will be given by:

$$S_2 \propto M_0 \sin 2\alpha \quad (1.17)$$

Using the double angle formula, $\sin 2\alpha = 2 \sin \alpha \cos \alpha$, and combining equations 1.16 and 1.17 it is possible to determine what α actually is.

$$\alpha = \arccos \left(\frac{S_2}{2S_1} \right) \quad (1.18)$$

Assuming that relative image phase is maintained, the technique should be valid for excitation angles in the range $0 \rightarrow \pi$. This technique does have several limitations, the first being that it is inherently slow. The magnetization before each RF pulse must be fully relaxed. This typically requires a repetition time on the order of $5T_1$. Secondly, it requires an assumption on the linearity of the RF pulse. That is, if twice the flip angle is prescribed, twice the excitation angle must be achieved. This assumption generally holds for non-selective pulses and selective pulses in the small tip angle regime ($< 90^\circ$). The technique does, however, begin to break down at very small tip angles. At this point, $\sin \alpha \approx \alpha$, and Equation 1.18 reduces to $\alpha = \arccos 1$.

The speed limitation of the DAM can be partially overcome by using additional pulses to “reset” the magnetization so that M_z is the same prior to the α or 2α pulse regardless of the repetition time [23,25]. The earliest form [23] used an additional 2α pulse in the α acquisition, and vice versa, to “compensate” for the different steady-state values. Later, saturation pulses were applied to “reset” the magnetization prior to each α or 2α sampling pulse [25]. The pulse sequence would then look like Figure 1.3. The magnetization preceding each sampling pulse would then be given by:

$$M_z = M_0 (1 - \exp(-T_{SR}/T_1)) \quad (1.19)$$

where T_{SR} is the time given for the longitudinal magnetization to recover before the α or 2α sampling pulse. Thus, some time would still be required for longitudinal recovery, but waiting for full recovery would no longer be required. This allows the DAM to be run more rapidly, at the expense of lost SNR and greater noise in the flip angle maps.

1.3.4 Phase Based Methods

The above methods work on the principle of encoding flip angle information into the intensity of MR images. It is also possible to make use of image phase to determine the flip angle. These techniques are based on composite pulses [19,20] and typically

employ large flip angles. These phase based techniques also require a baseline subtraction image to remove other sources of image phase such as B_0 inhomogeneity and receive phase.

A spin echo method [19] makes use of a composite $90_y^\circ - \alpha_x - 90_y^\circ$ inversion pulse to refocus transverse spins and additionally encode flip angle information. The pulse sequence is repeated twice, with the nominally 180° α pulse omitted from one of the repetitions, as shown in Figure 1.4. Assuming on resonance spins, with the α pulse omitted, the $90_y^\circ - 90_y^\circ$ composite pulse causes a spin echo to be refocussed along the $+\hat{y}'$ direction. With the α pulse included, a spin echo will be formed with a phase given by the angle of the α pulse. Subtracting the phase of the two images allows for the removal of receiver image phase, and in principle an additional acquisition would be required to remove B_0 related image phase. The flip angle, α , is then determined from the image phase by a complex relationship and is found using a look-up-table approach [19]. There is an approximately linear relationship between image phase and flip angle in the region near 180° .

A simplified approach is to use a single, non-selective, $2\alpha_x - \alpha_y$ composite pulse [20]. Extraneous sources of phase are removed by repeating the sequence twice, once with a $2\alpha_x - \alpha_y$ composite pulse and once with a $2\alpha_{-x} - \alpha_y$ and using the difference in phase. The flip angle is still related to image phase in a relatively complex relationship, but is relatively linear at around 90° . Like the spin-echo technique, this technique is also sensitive to off resonances that in principle must be removed by mapping B_0 .

A novel phase based approach that doesn't require composite pulses makes use of the Bloch-Siegert Shift [21]. A preparation pulse initially tips magnetization into the transverse plane. This is then acted on by an off resonance pulse shown in Figure 1.5. The off resonance pulse causes the transverse magnetization to precess about \mathbf{B}_1^{eff} . With $\omega_{RF}/\gamma \gg B_1$, this pulse creates a phase shift that depends on ω_{RF} , B_1 , and the duration of the off resonance pulse. As in the above techniques, other sources of

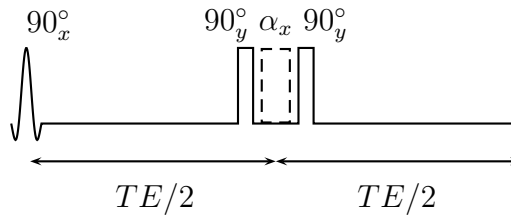


Figure 1.4: Pulse sequence for mapping the flip angle based on a composite pulse.

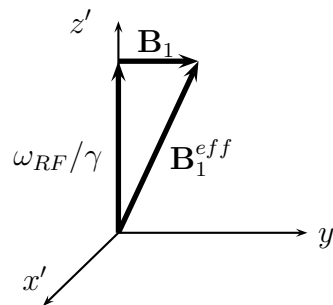


Figure 1.5: Off resonance pulse used in the Bloch-Siegert B_1 mapping technique.

image phase must still be removed. This is done by repeating the acquisition twice, once with off-resonance frequency $+\omega_{RF}$ and again with $-\omega_{RF}$ and then taking the phase difference between the two.

1.3.5 Interleaved Delay and Actual Flip Angle Mapping

The concept of using two images acquired using an interleaved delay is similar to the stimulated echo approach in that in one repetition, two signals are acquired, but it differs in that magnetization is not refocussed. Thus, in the pulse sequence shown in Figure 1.6, two images are created from the signals immediately following two identical RF pulses, but with interleaved, different delays. If the repetition time TR_1 is short enough that T_1 relaxation can be ignored entirely, the two signals will

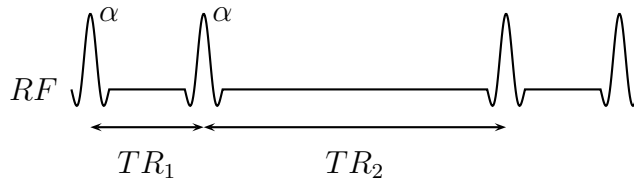


Figure 1.6: Timing diagram of the AFI pulse sequence.

have intensities given by [30]:

$$S_1 = M_z \sin \alpha \quad (1.20)$$

$$S_2 = M_z \cos \alpha \sin \alpha \quad (1.21)$$

The ratio of the two signals can then be used to find the flip angle:

$$\alpha = \arccos\left(\frac{S_2}{S_1}\right) \quad (1.22)$$

The actual flip angle imaging (AFI) sequence [26] is based on the same approach and basic concept as the above, but relaxation is not ignored entirely. Instead the repetition time constraint is relaxed somewhat, and so long as $TR_1 < TR_2 < T_1$, an expression for α can still be derived that is largely independent of relaxation:

$$\alpha = \arccos\left(\frac{rn - 1}{n - r}\right) \quad (1.23)$$

where $r = S_2/S_1$ and $n = TR_2/TR_1$.

While simple to implement, and a fast imaging technique in theory, this approach does have one significant limitation. The recommended range for α is $20 - 70^\circ$ [26] and with repetition times significantly less than T_1 , it becomes difficult to effectively spoil the transverse magnetization between acquisitions [16, 31, 32].

1.4 Look-Locker

The longitudinal recovery constant, T_1 , is often measured using an inversion recovery pulse sequence. After each inversion, a recovery period TI is allowed before the longitudinal magnetization is sampled. Additional time is then required to allow M_z to recover before the next inversion pulse. The measurement is then repeated several more times with different values for TI , thus giving multiple points along the inversion recovery curve, to which a signal equation can be fit, and the T_1 value determined. With each repetition of the pulse sequence, the signal at only one TI value can be determined. While robust, this approach is slow.

While in conventional inversion recovery, only one sample along the recovery curve is possible after each inversion, the Look-Locker approach [33] takes many samples while the longitudinal magnetization recovers. This experiment is shown in Figure 1.7. So long as the sampling angle is small, the recovery of M_z will be minimally perturbed. This leads to a modified longitudinal recovery constant:

$$\frac{1}{T_1^*} = \frac{1}{T_1} - \frac{\ln(\cos \alpha)}{\tau} \quad (1.24)$$

where α is the flip angle of the sampling pulse, and τ is the repetition time of the α pulses. In this way, samples at multiple points along the recovery curve can be acquired far more quickly than in the conventional inversion recovery approach.

While initially conceived as a NMR experiment, intended to only measure T_1 , the Look-Locker technique was soon adapted to 2D imaging [34, 35]. The inversion α -pulse-train is repeated for every k_y phase encode step. By using slice selective pulses and including phase and frequency encoding gradients, an image can be formed with signal corresponding to each α pulse. It was also demonstrated that, while a Look-Locker approach to acquiring T_1 maps allowed a shorter scan time, the technique still retained the high SNR efficiency of the gold standard inversion recovery technique [36].

The technique was then compressed into an accelerated 3D Look-Locker acquisition scheme [37]. Acquiring all the view and slice phase encodes if each α pulse

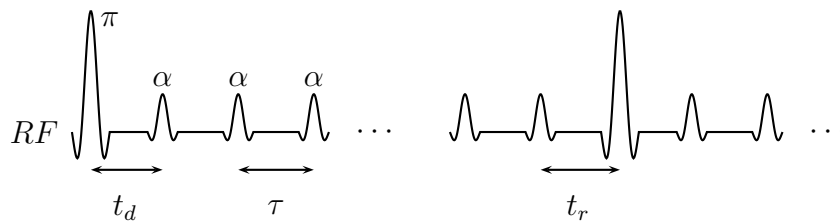


Figure 1.7: Timing diagram of the conventional Look-Locker acquisition. An image is created for each α sampling pulse.

was used to form one TI would require a prohibitively large number of repetitions of the inversion/ α -pulse train and a correspondingly long scan time. This problem was overcome by sampling the recovery curve even more quickly. If more samples along the longitudinal recovery curve are taken with reduced α and τ , the samples can then be segmented into effective TI volumes as in Figure 1.8. In this way an N_α long α -pulse-train can be used to form N_{TI} , 3D, effective TI images, with N_{ETL} fewer repetitions of the inversion/ α -pulse train.

Additional delays, t_d and t_r before and after the α -pulse train may be included to increase the dynamic range of the technique, and are to some extent unavoidable. In the accelerated 3D method, additional delays may also be included between effective TI volumes [38], though these complicate the signal equation. The original implementation also only accelerated the acquisition in one direction, along the G_y phase encode direction, using a sequentially increasing phase table, not the centric 2D acceleration shown in Figure 1.8. The choice of acceleration direction and order will have an effect on the resulting point spread function (PSF) [39].

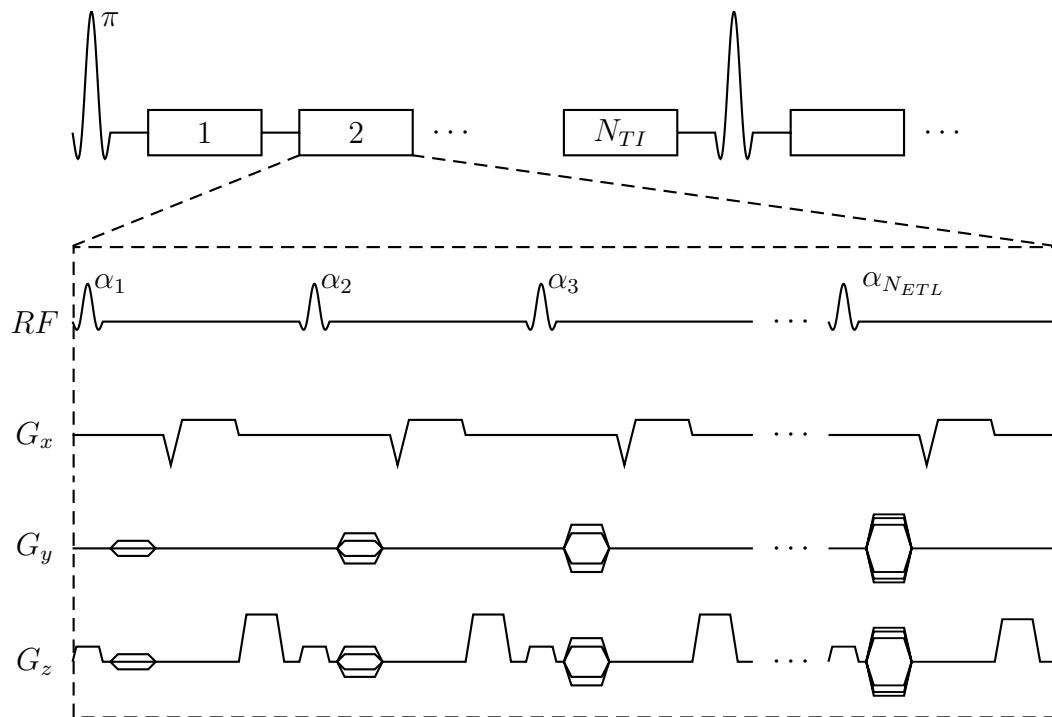


Figure 1.8: Timing diagram of the accelerated 3D Look-Locker sequence. N_α pulses along the recovery train are segmented into N_{TI} effective TI volumes.

1.5 Spoiling

To decrease scan times, it is possible to reduce repetition times to values less than T_2 . This complicates imaging, as there will still be some residual transverse magnetization at the end of each TR period, which will persist into and can be refocussed in the next TR period. Most often this fast imaging is conducted in the steady-state, and leads to two broad classifications based on how the residual transverse magnetization is handled. In the first, steady-state free precession (SSFP), the residual transverse magnetization is intentionally maintained and “refocussed”. This leads to an extremely efficient use of the available magnetization, though the signal will in general be given by a complex equation [40].

The other alternative is to “spoil”, or set to zero, the transverse magnetization at the end of each TR period. Setting the transverse magnetization to zero leads to a simpler expression for the theoretical signal, making qualitative and quantitative interpretation easier, but spoiling the magnetization is not always straightforward.

A simplistic approach would place a large gradient at the end of each TR interval. This would effectively dephase the spins from the immediately preceding RF pulse and lead to zero net M_{xy} , but repeated applications would lead to coherence pathways where the net induced phase of the gradients is balanced. Alternatively, gradients with random [41] or linearly increasing amplitude [42, 43] may be used. These techniques, however, are not sufficient. Random gradients will not lead to a true steady-state, leading to variations in signal from TR to TR . In conventional Cartesian acquisitions this will manifest itself as a ghosting artefact. Linearly increasing gradients on the other hand, may lead to a true steady-state, but with a spatially dependent spoiling efficiency [36], manifesting itself as a banding artefact.

The standard spoiling implementation on most scanners is based on radio frequency spoiling, using an RF phase that increases quadratically from TR to TR

combined with a constant amplitude crusher gradient [44]:

$$\phi_n = \phi_{n-1} + n\phi_{seed} \quad (1.25)$$

where ϕ_n is the phase of the n^{TH} RF pulse, and ϕ_{seed} is the quadratic increment. A quadratically increasing phase combined with a crusher gradient that creates a multiple of 2π phase variation across the imaging voxel ensures that the signal will enter steady-state. An appropriate choice of ϕ_{seed} (usually 117° or 123°) [44] will ensure that the accumulated coherence pathways will effectively cancel and give a signal that closely approximates a perfectly spoiled steady-state value.

The quadratically increasing phase has proven to be quite robust for a range of imaging applications, but it is not without its limitations. For quantitative imaging, the results may be highly sensitive to any deviation from ideal spoiling, and other values for ϕ_{seed} have been suggested for variable flip angle based T_1 imaging [45, 46]. For the approach to steady-state, different values again for ϕ_{seed} are optimal, depending on the circumstances [15, 47].

Phase spoiling becomes even more complicated with sequences that are not a simple repetition of the same RF pulse. For the AFI flip angle imaging technique [26], which employs an interleaved TR acquisition scheme, the quadratically increasing phase needs to be modified significantly [32], and there is evidence that for the short repetition times and large flip angles typically involved, the only effective spoiling method requires damping signal via large gradients to cause losses due to diffusion [31, 32].

For the above quantitative T_1 and flip angle mapping techniques, where accuracy of the measured signal is essential, there may be some incentive to revisiting random spoiling. By combining randomized RF phase and gradient crusher amplitudes it is possible to produce a signal that will on average match the ideally spoiled value [16]. The random nature of the spoiling means that the magnetization is never truly in steady-state. Thus in conventional imaging, there will be random oscillations from

TR to TR . These can manifest themselves as ghosting artefacts as in the early random spoiling implementations. In this case, however, they are overcome by employing a radial sampling trajectory, effectively oversampling the centre of k-space and thus averaging out the random fluctuations.

The primary motivation for quadratic RF spoiling is that it leads to magnetization in the steady-state. This produces no variation in magnetization from repetition to repetition and thus a good point spread function with no ghosting artefacts. In sequences that sample along the transient, quadratic spoiling is often still used, but now the motivation is somewhat different. If perfect spoiling were achieved there would be variation in signal from TR to TR by the nature of sampling during the transient phase. Even an optimized choice of ϕ_{spoil} is not capable of matching a slowly varying transient, and instead produces erratic deviation from the ideal transient. These deviations are consistent from transient to transient, but difficult to predict based on the physical and imaging parameters.

1.6 Thesis Outline

In this Thesis I introduce a new approach to mapping the flip angle in MRI. This approach is based on the Look-Locker sequence, which was conceived as a highly efficient method for measuring the longitudinal relaxation time, T_1 . By acquiring two transients, and altering either the flip angle, or the repetition time, the data can be used to solve for the actual flip angle achieved in tissue in a highly time efficient manner and in 3D.

Chapters 2, 3, and 4 of the Thesis were drafted as manuscripts intended for submission to Magnetic Resonance in Medicine, since this is the journal where most of the flip angle mapping techniques have been presented. The chapters themselves largely follow the logical development of the concept. Chapter 2 introduces the various new ways in which the accelerated 3D Look-Locker sequence can be used to measure the

flip angle. Chapter 3 presents a theoretical optimization of the techniques. As such, Chapter 3 is useful for understanding the choice of parameters used to acquire the images in Chapter 2, but this organization allows Chapter 2 and Chapter 3 to stand alone as independent manuscripts. Finally, Chapter 4 is an investigation of a new approach to spoiling for transients, and demonstrates a novel solution to address one of the primary limitations of the Look-Locker technique.

1.6.1 Chapter 2: Flip Angle Mapping With the Accelerated 3D Look-Locker Sequence

The Look-Locker technique is a very time efficient method of mapping the longitudinal recovery constant, T_1 . In Chapter 2, several novel ways in which the accelerated 3D Look-Locker pulse sequence can be adapted to measure the flip angle are introduced. The Look-Locker acquisition technique measures a modified longitudinal recovery constant, T_1^* that depends on the true T_1 , the flip angle and the repetition time, τ . By repeating the measurement of T_1^* twice, and altering either α or τ for the second measurement, it is possible to determine the true α from the two measurements of T_1^* .

The dual α approach (DALL) acquires the transient using a train of α pulses, and then repeats the measurement using pulses with twice the flip angle. By using this approach, the trigonometric double angle formula can be used to solve for the actual flip angle achieved. The dual τ approach (D τ LL), uses two repetition times related by the ratio $n = \tau_2/\tau_1$, with the flip angle held constant, and using the ratio n , and the two measured recovery constants, an expression for the true flip angle can also be derived.

The acquisition scheme of the accelerated 3D Look-Locker technique presents other unique opportunities for acquisition of the transients. Typically the inversion- α -train combination would have to be repeated several times to fully sample k-space.

Thus the two T_1^* values can be acquired sequentially. In other words, the inversion- α -train is repeated until the first T_1^* data set is fully acquired, and then the second would be acquired. Alternatively, the datasets may be acquired in an interleaved sense. In this case, an inversion- α -train is interleaved with a inversion- 2α -train (or τ_2), and this intereaved combination is repeated to fully sample the image. This second approach presents a novel opportunity. The two data sets may be acquired with the inversion pulses omitted entirely, as the end of one transient acts as the preparation for the next.

1.6.2 Chapter 3: Optimizing the Efficiency of Flip Angle Mapping Techniques

The accelerated 3D Look-Locker imaging technique is inherently a fairly complex image acquisition scheme, with many image acquisition parameters that can affect the acquired images. This condition is further complicated by adapting it to image flip angles either through the DALL or $D\tau$ LL approaches. It was, however, shown to be a very efficient method of mapping T_1 [36]. The concept of imaging efficiency (flip angle to noise ratio normalized by scantime) is adapted to flip angle mapping, making it possible to optimized the imaging parameters of the accelerated 3D Look-Locker sequence. These imaging parameters include the repetition time τ , flip angle α , number of effective TI volumes N_{TI} , and the length of the read-out train N_α , as well as the choice of how the transients are prepared and interleaved.

The double angle and interleaved repetition time flip angle mapping methods are also included in this chapter. An attempt is made to optimize their imaging parameters, making it possible to compare them to the Look-Locker based methods. Interestingly, the results imply that the DAM and AFI approaches may be acquired more efficiently with flip angles and parameters significantly different from those conventionally used. Experimental flip angle and noise maps are used to verify the

simulations.

The results of the optimizations indicate that for fast imaging (one minute scantime for a 3D matrix with 32 phase and 32 slice encodes) with the Look-Locker approaches, and in particular, the inverted, non-interleaved approach, have an efficiency that exceeds the more conventional methods. If this scantime restriction is relaxed, then the AFI approach would appear to be optimal. The simulation results presented in this chapter assume perfect spoiling of the transverse magnetization, and thus that image noise is the primary source of error on the flip angle maps. This is not entirely true, especially as repetition times become short and flip angles become larger. These issues are discussed further in Chapter 4.

1.6.3 Chapter 4: Spoiling for Accelerated 3D Look-Locker Acquisitions

In the development of Chapters 2 and 3, it was discovered that in fitting transients to the Look-Locker decay curves to measure T_1^* and thus determine the flip angle, that the deviations of the experimental points from the transients fit displayed a systematic error. Many times, especially for larger flip angles, the Look-Locker curves appeared decidedly non-exponential. This necessitated investigating the nature of spoiling for transient applications.

Much of the existing work on spoiling was based on a scheme developed for steady-state imaging applications. A quadratically increasing RF phase with a uniform gradient crusher would lead to a signal that reaches steady-state, and for an appropriate choice of quadratic increase, would lead to an effective cancellation of coherence pathways, and thus a signal that matched the ideally spoiled value for a large range of applications.

A quadratically increasing phase, however, does not have many redeeming qualities when used for spoiling transient acquisitions. The sampled data points will not match

the perfectly spoiled case, and instead will deviate from the ideal exponential in an erratic manner, leading to unpredictable, systematic errors in the exponential decay constant fit to the curve. A randomized phase and randomized gradient crusher are shown to be able to reduce the deviations from the ideally spoiled transient, and thus result in better accuracy in the exponential coefficient. These spoiling schemes were analyzed both through Bloch simulations and then verified with experiments, and the random spoiling was shown to produce a more accurate estimate of the exponential decay constant, and thus of the resulting flip angle.

1.6.4 Appendix A: Error Propagation

The theoretical flip angle imaging efficiency presented in Chapter 3 for the double angle method, interleaved repetition time, and Look-Locker based flip angle imaging techniques is based on a dimensionless noise propagation factor, b . This parameter is convenient, because it requires no *a priori* knowledge of the noise or signal levels. The relative signal levels of the different methods are determined from the Bloch equation, and b is then based on a theoretical analysis of the noise propagation from the signal through the signal equations and non-linear fitting procedures.

In this section, the dimensionless noise propagation factor is derived in detail for the 3 methods. This analysis makes use of standard noise propagation techniques, as well as an error matrix approach to analyze the noise propagation through the non-linear least squares fitting used in the Look-Locker techniques.

1.6.5 Co-Authorship

The concept of applying the double angle approach to the Look-Locker technique to map the flip angle was first suggested to me by my supervisors Drs. Brian Rutt and Charles McKenzie. All subsequent theory development and experimental design were conducted by myself, under the guidance and support of my supervisors. Data were

collected by myself, with the exception of the in vivo exams, which were conducted with the assistance of Cyndi Harper-Little, and the carbon-13 data, which were collected by Lanette Friesen-Waldner. For all chapters, I was the primary author.

References

- [1] Vaughan J, Garwood M, Collins C, Liu W, DelaBarre L, Adriany G, Andersen P, Merkle H, Goebel R, Smith M, and Ugurbil K. 7T vs. 4T: RF power, homogeneity, and signal-to-noise comparison in head images. *Magn Reson Med* 2001; 46:24–30.
- [2] de Moortele PFV, Akgun C, Adriany G, Moeller S, Ritter J, Collins CM, Smith MB, Vaughan JT, and Ugurbil K. B_1 destructive interferences and spatial phase patterns at 7 T with a head transceiver array coil. *Magn Reson Med* 2005; 54:1503–1518.
- [3] Collins CM, Liu W, Weston Schreiber M, Yang QX, and Smith MB. Central brightening due to constructive interference with, without, and despite dielectric resonance. *J Magn Reson Imaging* 2005;21:192–196.
- [4] Gabriel C. Compilation of the dielectric properties of body tissues at RF and microwave frequencies. Technical Report AL/OE-TR-1996-0037, Air Force Materiel Command, Brooks Air Force Base, Texas, 1996.
- [5] Yang QX, Wang J, Zhang X, Collins CM, Smith MB, Liu H, Zhu X, Vaughan JT, Ugurbil K, and Chen W. Analysis of wave behavior in lossy dielectric samples at high field. *Magn Reson Med* 2002;47:982–989.
- [6] Saekho S, Boada FE, Noll DC, and Stenger VA. Small tip angle three-dimensional tailored radiofrequency slab-select pulse for reduced B_1 inhomogeneity at 3 T. *Magn Reson Med* 2005;53:479–484.
- [7] Ibrahim TS, Lee R, Baertlein BA, Abduljalil AM, Zhu H, and Robitaille PML. Effect of RF coil excitation on field inhomogeneity at ultra high fields: a field optimized TEM resonator. *Magn Reson Imaging* 2001;19:1339–1347.

- [8] Vaughan T, DelaBarre L, Snyder C, Tian J, Akgun C, Shrivastava D, Liu W, Olson C, Adriany G, Strupp J, Andersen P, Gopinath A, van de Moortele P, Garwood M, and Ugurbil K. 9.4T human MRI: Preliminary results. *Magn Reson Med* 2006;56:1274–1282.
- [9] Katscher U, Börnert P, Leussler C, and van den Brink JS. Transmit SENSE. *Magn Reson Med* 2003;49:144–150.
- [10] Ullmann P, Junge S, Wick M, Seifert F, Ruhm W, and Hennig J. Experimental analysis of parallel excitation using dedicated coil setups and simultaneous RF transmission on multiple channels. *Magn Reson Med* 2005;54:994–1001.
- [11] Pauly J, Nishimura D, and Macovski A. A k-space analysis of small-tip-angle excitation. *J Magn Reson* 1989;81:43–56.
- [12] Dowell NG and Tofts PS. Fast, accurate, and precise mapping of the RF field in vivo using the 180° signal null. *Magn Reson Med* 2007;58:622–630.
- [13] Deoni SC. High-resolution T1 mapping of the brain at 3T with driven equilibrium single pulse observation of T1 with high-speed incorporation of RF field inhomogeneities (DESPOT1-HIFI). *J Magn Reson Imaging* 2007;26:1106–1111.
- [14] Insko E and Bolinger L. Mapping of the radiofrequency field. *J Magn Reson A* 1993;103:82–85.
- [15] Epstein FH, Mugler III JP, and Brookeman JR. Spoiling of transverse magnetization in gradient-echo (GRE) imaging during the approach to steady state. *Magn Reson Med* 1996;7:237–245.
- [16] Lin W and Song HK. Improved signal spoiling in fast radial gradient-echo imaging: Applied to accurate T_1 mapping and flip angle correction. *Magn Reson Med* 2009;62:1185–1194.

- [17] Bloch F. Nuclear induction. *Phys Rev* 1946;70:460–474.
- [18] Silver MS, Joseph RI, and Hoult DI. Highly selective $\pi/2$ and π pulse generation. *J Magn Reson* 1984;59:347–351.
- [19] Oh C, Hilal S, Cho Z, and Mun I. Radio frequency field intensity mapping using a composite spin-echo sequence. *Magn Reson Imaging* 1990;8:21–25.
- [20] Morrell GR. A phase-sensitive method of flip angle mapping. *Magn Reson Med* 2008;60:889–894.
- [21] Sacolick LI, Wiesinger F, Hancu I, and Vogel MW. B_1 mapping by Bloch-Siegert shift. *Magn Reson Med* 2010;63:1315–1322.
- [22] Hornak JP, Szumowski J, and Bryant RG. Magnetic field mapping. *Magn Reson Med* 1988;6:158–163.
- [23] Stollberger R and Wach P. Imaging of the active B_1 field in vivo. *Magn Reson Med* 1996;35:246–251.
- [24] Helms G. A precise and user-independent quantification technique for regional comparison of single volume proton MR spectroscopy of the human brain. *NMR Biomed* 2000;13:398–406.
- [25] Cunningham CH, Pauly JM, and Nayak KS. Saturated double-angle method for rapid B_1+ mapping. *Magn Reson Med* 2006;55:1326–1333.
- [26] Yarnykh VL. Actual flip-angle imaging in the pulsed steady state: A method for rapid three-dimensional mapping of the transmitted radiofrequency field. *Magn Reson Med* 2007;57:192–200.
- [27] Akoka S, Franconi F, Seguin F, and Le Pape A. Radiofrequency map of an NMR coil by imaging. *Magn Reson Imaging* 1993;11:437–441.

- [28] Jiru F and Klose U. Fast 3D radiofrequency field mapping using echo-planar imaging. *Magn Reson Med* 2006;56:1375–1379.
- [29] Hahn EL. Spin echoes. *Phys Rev* 1950;80:580–594.
- [30] Pan JW, Twieg DB, and Hetherington HP. Quantitative spectroscopic imaging of the human brain. *Magn Reson Med* 1998;40:363–369.
- [31] Yarnykh VL. Optimal radiofrequency and gradient spoiling for improved accuracy of T_1 and B_1 measurements using fast steady-state techniques. *Magn Reson Med* 2010;63:1610–1626.
- [32] Nehrke K. On the steady-state properties of actual flip angle imaging (AFI). *Magn Reson Med* 2009;61:84–92.
- [33] Look D and Locker D. Time saving in measurement of NMR and EPR relaxation times. *Rev Sci Instrum* 1970;41:250–251.
- [34] Graumann R, Deimling M, Heilmann T, and Oppelt A. A new method for fast and precise T1 determination. *SMRM, Book of Abstracts* 1986;:922–923.
- [35] Brix G, Schad LR, Deimling M, and Lorenz WJ. Fast and precise T_1 imaging using a TOMROP sequence. *Magn Reson Imaging* 1990;8:351–356.
- [36] Crawley AP and Henkelman RM. A comparison of one-shot and recovery methods in T1 imaging. *Magn Reson Med* 1988;7:23–43.
- [37] Henderson E, Mckinnon G, Lee TY, and Rutt BK. A fast 3D Look-Locker method for volumetric T_1 mapping. *Magn Reson Imaging* 1999;17:1163–1171.
- [38] Nkongchu K and Santyr G. An improved 3-D Look-Locker imaging method for T_1 parameter estimation. *Magn Reson Imaging* 2005;23:801–807.

- [39] Nkongchu K and Santyr G. Phase-encoding strategies for optimal spatial resolution and T_1 accuracy in 3D Look-Locker imaging. *Magn Reson Imaging* 2007; 25:1203–1214.
- [40] Ernst RR and Anderson WA. Application of Fourier transform spectroscopy to magnetic resonance. *Rev Sci Instrum* 1966;37:93–102.
- [41] Freeman R and Hill H. Phase and intensity anomalies in Fourier transform NMR. *J Magn Reson* 1971;4:366–383.
- [42] Frahm J, Hanicke W, and Merboldt KD. Transverse coherence in rapid FLASH NMR imaging. *J Magn Reson* 1987;72:307–314.
- [43] Wood ML, Silver M, and Runge VM. Optimization of spoiler gradients in flash MRI. *Magn Reson Imaging* 1987;5:455–463.
- [44] Zur Y, Wood M, and Neuringer L. Spoiling of transverse magnetization in steady-state sequences. *Magn Reson Med* 1991;21:251–263.
- [45] Treier R, Steingoetter A, Fried M, Schwizer W, and Boesiger P. Optimized and combined T_1 and B_1 mapping technique for fast and accurate T_1 quantification in contrastenhanced abdominal MRI. *Magn Reson Med* 2007;57:568–576.
- [46] Preibisch C and Deichmann R. Influence of RF spoiling on the stability and accuracy of T_1 mapping based on spoiled FLASH with varying flip angles. *Magn Reson Med* 2009;61:125–135.
- [47] Busse RF and Riederer SJ. Steady-state preparation for spoiled gradient echo imaging. *Magn Reson Med* 2001;45:653–661.

Chapter 2

Flip Angle Mapping With the Accelerated 3D Look-Locker Sequence

Abstract

A new approach to mapping the flip angle quickly and efficiently in 3D based on the Look-Locker technique is presented. The Look-Locker technique is a highly efficient method of mapping T_1 that allows significantly reduced scan times by sampling continuously during longitudinal recovery. This results in an exponential recovery that depends on T_1 , repetition time, and flip angle. By combining acquisitions in a double angle or dual TR approach, two values for the modified longitudinal recovery constant, T_1^* , are acquired. These can be combined to very quickly and efficiently map the flip angle in 3D. Being a 3D method, the technique is capable of mapping variations due to wavelength effects and RF slab profile selection.

The acquisitions may be acquired conventionally, interleaved, or interleaved with the preparation pulses removed entirely. This last option allows for direct fitting of the two recovery curves with a reduced number of parameters. The techniques are validated in vitro against the dual TR technique for a range of flip angles and T_1 values. In addition, an application to correcting in vivo DESPOT T_1 data is presented.

2.1 Introduction

At high magnetic fields, human sized, volume transmit, RF coils can no longer be assumed to produce uniform excitation of tissue. As the magnetic field increases, the wavelength of the excitation pulse decreases, and as it approaches the scale of the object being imaged, it becomes impossible to avoid destructive interference of the B_1^+ field [1]. This leads to non-uniform excitation of the desired imaging volume. The problem also exists in a wide variety of other imaging applications, anywhere the transmit coil has non-uniform B_1^+ sensitivity.

In the least obtrusive cases this non-uniform excitation manifests itself as an intensity variation across the sample, but when steady-state or quantitative imaging is considered, the problem becomes more serious. For steady-state imaging, differences in excitation angle may lead to different tissue contrast in different parts of the imaging volume, and for quantitative imaging, that relies on accurate knowledge of the flip angle, for example DESPOT1 and DESPOT2 [2], variations in flip angle will lead to inaccuracies in the quantitative measurements.

The non-uniform excitation can be dealt with by using a measured excitation profile to correct the quantitative imaging data. The excitation profile itself can also be flattened with tailored RF pulses [3], or using both coil profiles and spatially selective pulses as in transmit SENSE [4, 5]. What all these approaches require is a map of the transmit coil excitation profile, B_1^+ , which is determined by mapping the flip angle. For transmit SENSE in particular, for which a profile of each coil in the array is required, the flip angle mapping technique must also be fast.

Several methods of mapping the flip angle exist. A number of these are based on the double angle method (DAM) [6, 7]. These either require a long repetition time or use saturation pulses [8] to avoid a T_1 bias. Both lead to inefficient use of the available magnetization. A more general approach is to fit the signal over a wider range of applied excitation angles [9]. These methods assume linearity of the

transmitter, and are susceptible to slab and slice profile variations at the required large applied excitation angles. There are alternative methods that do not rely on the RF transmitter linearity assumption. These include a fast interleaved TR method [10], dubbed actual flip angle imaging (AFI), and encoding the flip angle using image phase [11–13].

The AFI method has emerged as a popular technique. It is relatively simple to implement, and extraction of flip angle information from the intensity images is relatively straight forward. It does, however, work best at moderate to large flip angles (40-60°) and short repetition times [10]. This poses a significant challenge in terms of spoiling the transverse magnetization to avoid a biased estimate of the flip angle [14–16], especially when the sequence is run rapidly.

The Look-Locker technique [17] was initially conceived as a technique to rapidly measure the longitudinal relaxation time, T_1 . In contrast to inversion recovery methods, that require waiting for the longitudinal magnetization to fully recover before the next sample is taken, the Look-Locker technique acquires multiple low flip angle spoiled, gradient recalled (SPGR) echoes during the longitudinal recovery phase. In this way, samples at multiple post inversion (TI) time points can be acquired far faster than conventionally possible. The sampling pulses not only sample the longitudinal relaxation, but in doing so, also perturb it, leading to a modified, or driven longitudinal relaxation time:

$$\frac{1}{T_1^*} = \frac{1}{T_1} - \frac{\ln(\cos \alpha)}{\tau} \quad (2.1)$$

where α is the tip angle of the sampling pulses, and τ is the repetition time of the α pulses.

T_1^* is measured by least squares fitting of an exponential recovery equation:

$$S(t) = A + (B - A) \exp(-t/T_1^*) \quad (2.2)$$

to the sampled points, and from this, assuming the flip angle is known, T_1 can be extracted. The signal, $S(t)$, will relax from the value B , which is a complicated term

that depends on the inversion preparation pulse accuracy, as well as characteristics of the previously applied α pulse train and other sequence parameters α pulses and sequence timing parameters [18–20]. A is more straightforward, as the transient relaxes towards the spoiled steady-state value:

$$A = \sin \alpha \frac{1 - E_\tau}{1 - \cos \alpha E_\tau} \quad (2.3)$$

where $E_\tau = \exp(-\tau/T_1)$

This technique is desirable as it provides the ability to measure T_1 very quickly while still retaining the SNR efficiency of the gold standard inversion recovery technique [21].

The Look-Locker technique was modified first into a 2D imaging technique [18], by adding imaging gradients to each sampling segment, and repeating the inversion sampling scheme multiple times to encode all the necessary lines of k-space. The technique was then further developed into the accelerated 3D Look-Locker (a3DLL) sequence [19]. Rather than producing one TI image for each α pulse in the sampling train, multiple contiguous α pulses can be used to accelerate the filling of one k-space, and the k-space acquisition segmented so that N_{TI} “effective TI ” images could be reconstructed from N_α pulses sampling the recovery curve, with $N_{TI} < N_\alpha$, leading to an acceleration factor $R = N_\alpha/N_{TI}$.

Measuring the T_1 value using the Look-Locker technique relies on accurate knowledge of the flip angle. The exponential fitting itself contains sufficient information to do this directly. Instead of fitting for T_1^* , A , and B in Equation 2.2 above, it is possible to fit for B , α and T_1 directly by combining Equations 2.2, 2.3, and the exact expression for B [18]. This approach, however, assumes that the flip angle ratio of the sampling pulse to the preparation pulse is known.

Parker [22] proposed a method of determining the flip angle by measuring T_1^* at multiple nominal flip angles related by a known ratio, and then minimizing the variation in the resulting T_1 values. In the special case where $\alpha_2 = 2\alpha_1$, the trigonometric

double angle formula can be used to form a closed form solution for the flip angle based on the two transients [23, 24].

Alternatively, rather than two different flip angles to untangle T_1 and α in the T_1^* measurement, two different values for the sampling repetition time, τ can also be used [23, 25].

Here we will investigate the properties of the accelerated 3D Look-Locker sequence, and several ways in which the flip angle can be extracted from the measured recovery curves.

2.2 Theory

The accelerated 3D Look-Locker sequence uses N_α low tip angle pulses with a short delay τ , between them to excite and sample the recovering longitudinal magnetization. These are grouped into N_{TI} effective inversion time images so that with each inversion- α -train repetition, $N_{ETL} = N_\alpha/N_{TI}$ lines of k-space are acquired for each effective TI image. The effective inversion time is given by the time after inversion at which the center of k-space is acquired for each of the N_{TI} effective TI images.

The inversion- α -train combination must then be repeated $N_{shots} = N_{ky,kz}N_{TI}/N_\alpha$ times to fully encode 3D k-space. Additional delays between the inversion pulse and the start of the α -train, and between the end of one α -train and the next inversion pulse are possible, and to some extent unavoidable, due to the finite time required for the inversion pulse as well as non-zero inversion delay and end-of-sequence delay. Additional delays between segments of the α -read-out train are also possible [20], but will not be considered here. All of these delays can be kept short compared to T_1 and therefore we will ignore them for purposes of simplifying theory in this Thesis.

Once several inversion- α -train combinations are run, the magnetization enters a dynamic steady-state whereby it relaxes towards, but does not necessarily reach, the steady-state value as defined by Equation 2.3. The starting value of the transient,

B is determined by the inversion of longitudinal magnetization at the end of the previous transient plus any extra delays. An exact solution for B is possible [18,19]:

$$B = \frac{-A \cos \alpha E_r E_d \left[1 - (\cos \alpha E_\tau)^{N_\alpha - 1} \right] - 2E_d + E_r + 1}{1 + \cos \alpha E_r E_d (\cos \alpha E_\tau)^{N_\alpha - 1}} \quad (2.4)$$

$$E_d = \exp(-t_d/T_1) \quad (2.5)$$

$$E_r = \exp(-t_r/T_1) \quad (2.6)$$

where t_d is the delay between the inversion pulse and first α pulse, t_r is the delay between the last α pulse and the next inversion pulse, as indicated in Figure 1.7. A perfect inversion has been assumed, which in the presence of B_1^+ inhomogeneity may not be realistic.

If the delays and time required to play out the inversion pulse are assumed short with respect to the longitudinal relaxation, the starting value for the signal can be simplified to:

$$B \approx -A \frac{1 - \exp(-N_\alpha \tau / T_1^*)}{1 + \exp(-N_\alpha \tau / T_1^*)} \quad (2.7)$$

Due to the short repetition time, τ , of these pulses, spoiling optimized for transients is necessary [26].

2.2.1 Double Angle Look-Locker (DALL)

If the accelerated Look-Locker sequence is repeated for two different values of the low flip angle α pulse, it will result in two different measurements of the recovery constant:

$$\frac{1}{T_{1,1}^*} = \frac{1}{T_1} - \frac{\ln(\cos \alpha_1)}{\tau} \quad (2.8)$$

$$\frac{1}{T_{1,2}^*} = \frac{1}{T_1} - \frac{\ln(\cos \alpha_2)}{\tau} \quad (2.9)$$

as well as values for the other fitting parameters in Equation 2.2, A_1 , A_2 , B_1 and B_2 .

If the two flip angles are chosen such that $\alpha = \alpha_1 = \alpha_2/2$, the trigonometric double angle formula can be used to derive a simple expression for the actual flip angle achieved in the double angle Look Locker (DALL) sequence:

$$\begin{aligned}\alpha &= \arccos \left[\frac{1}{4} \left(E_\Delta + \sqrt{E_\Delta^2 + 8} \right) \right] \\ E_\Delta &= \exp \left(\frac{\tau}{T_{1,1\alpha}^*} - \frac{\tau}{T_{1,2\alpha}^*} \right)\end{aligned}\tag{2.10}$$

The corrected α value can then be used in either equation 2.8 or 2.9 to find a corrected value for T_1 .

2.2.2 Interleaved Inverted DALL (intDALL)

To this point the approach has been general with respect to the actual sequence timing. The simplest approach is to acquire a full set of images using a3DLL and the flip angle α , and then a second data set using 2α . In these cases, Equation 2.7 produces two different B values for the two acquisitions corresponding to 1α and 2α flip angles. If however, either 1α or 2α are far from the Ernst angle, the corresponding A value will be small, and the dynamic range of the transient may be non-optimal for measuring the respective T_1^* value.

It is possible to interleave the acquisitions. In this interleaved double angle Look-Locker (intDALL) implementation, an inversion- α -train is interleaved with the inversion- 2α -train (see Table 2.1). This has the effect of equalizing the dynamic range of the transients in the $T_{1,1\alpha}^*$ $T_{1,2\alpha}^*$ measurements, and thus of the α measurement. Thus the starting value of the 1α acquisition is given by the magnetization at the end of the 2α acquisition and vice versa:

$$\begin{aligned}B_1 &\approx -\sin \alpha M_{z,2\alpha}(N_\alpha \tau) \\ B_2 &\approx -\sin 2\alpha M_{z,1\alpha}(N_\alpha \tau)\end{aligned}\tag{2.11}$$

Solving these gives:

$$B_1 = \frac{-(\sin \alpha / \sin 2\alpha) A_2 (1 - E_{N,2}) + A_1 E_{N,2} (1 - E_{N,1})}{(1 - E_{N,1} E_{N,2})}\tag{2.12}$$

$$B_2 = \frac{-(\sin 2\alpha / \sin \alpha) A_1 (1 - E_{N,1}) + A_2 E_{N,1} (1 - E_{N,2})}{(1 - E_{N,1} E_{N,2})} \quad (2.13)$$

$$E_{N,1} = \exp\left(-\frac{N_\alpha \tau}{T_{1,1\alpha}^*}\right) \quad (2.14)$$

$$E_{N,2} = \exp\left(-\frac{N_\alpha \tau}{T_{1,2\alpha}^*}\right) \quad (2.15)$$

The data is still analyzed as in conventional DALL, by fitting for A_1 , B_1 and $T_{1,1\alpha}^*$ from the 1α data set and A_2 , B_2 and $T_{1,2\alpha}^*$ for the 2α data set, and then using $T_{1,1\alpha}^*$ and $T_{1,2\alpha}^*$ to determine the flip angle.

2.2.3 Interleaved Non-Inverted Look-Locker (niDALL)

The interleaved option provides another interesting option. The end of one α train can act as the seed for the next. Thus it is possible to do without the inversion pulses entirely. The flip angle can still be extracted from the $T_{1,1\alpha}^*$ and $T_{1,2\alpha}^*$ measurements made by fitting to each transient independently as in the DALL and intDALL techniques above. While the fitting will be simplified by removing the need to maintain image phase in the inversion recovery curves, the results of doing this are likely to be inferior due to the reduced dynamic range of the transients.

In the non-inverted double angle Look-Locker (niDALL) technique, the expressions for B_1 and B_2 above are replaced with:

$$\begin{aligned} B_1 &= \frac{(\sin \alpha / \sin 2\alpha) A_2 (1 - E_{N,2}) + A_1 E_{N,2} (1 - E_{N,1})}{(1 - E_{N,1} E_{N,2})} \\ B_2 &= \frac{(\sin 2\alpha / \sin \alpha) A_1 (1 - E_{N,1}) + A_2 E_{N,1} (1 - E_{N,2})}{(1 - E_{N,1} E_{N,2})} \end{aligned} \quad (2.16)$$

In this case, if one train follows directly from the previous one, with no inter-train delays at all, such that RF pulses are spaced by τ even at the boundary between the 1α and 2α trains, the assumptions of ideal inversion and negligible delays are removed, and the expressions for B_1 and B_2 become exact. This makes it possible to directly fit 3 parameters; T_1 , α and M_0 , to the combined transients.

2.2.4 Dual τ Look-Locker (D τ LL)

In the above, T_1^* depends on T_1 , τ and the flip angle. The double angle methods are based on extracting T_1 and α from this value by using two different flip angles to give two different values for T_1^* . It is possible to accomplish the same thing using two different values for the repetition time, τ .

The procedure would require measuring T_1^* using two different values for τ :

$$\begin{aligned}\frac{1}{T_{1,\tau_1}^*} &= \frac{1}{T_1} - \frac{\ln(\cos \alpha)}{\tau_1} \\ \frac{1}{T_{1,\tau_2}^*} &= \frac{1}{T_1} - \frac{\ln(\cos \alpha)}{\tau_2}\end{aligned}\quad (2.17)$$

If the relationship between the two τ values is given by $\tau = \tau_1 = \tau_2/n$, with $n > 1$, the two can be solved for α as follows:

$$\begin{aligned}\frac{1}{T_{1,\tau}^*} - \frac{1}{T_{1,n\tau}^*} &= \frac{\ln(\cos \alpha)}{n\tau} - \frac{\ln(\cos \alpha)}{\tau} \\ \frac{\tau}{T_{1,\tau}^*} - \frac{\tau}{T_{1,n\tau}^*} &= \ln(\cos^{1/n-1} \alpha) \\ \exp\left(\frac{\tau}{T_{1,\tau}^*} - \frac{\tau}{T_{1,n\tau}^*}\right) &= \cos^{1/n-1} \alpha \\ \alpha &= \arccos\left\{\exp\left[-\frac{n\tau}{n-1}\left(\frac{1}{T_{1,\tau}^*} - \frac{1}{T_{1,n\tau}^*}\right)\right]\right\}\end{aligned}\quad (2.18)$$

T_1 can then be solved for by back substitution.

2.2.5 Summary of Look-Locker Acquisition Schemes

The above approaches to interleaving the acquisition of the Look-Locker flip angle mapping techniques are summarized in Table 2.1. Each $\pi - \boxed{\alpha, \tau}_N$ represents one read-out train indicated in Figure 1.8, while the $[\]_{\text{repeat}}$ indicates the block that is to be repeated until the images are fully acquired. While not presented here, the D τ LL approach could also be adapted to use an interleaved or non-inverted and interleaved approach as well. The precise choice of sequence parameters to optimize the measurement of α will be discussed further in Chapter 3.

Method	Acquisition Order	Parameters Fit
DALL	$\left[\pi - \boxed{1\alpha, \tau}\right]_N$ repeat then $\left[\pi - \boxed{2\alpha, \tau}\right]_N$ repeat	$T_{1,1\alpha}^*, T_{1,2\alpha}^*, A_1, A_2, B_1, B_2$
intDALL	$\left[\pi - \boxed{1\alpha, \tau}\right]_N - \pi - \boxed{2\alpha, \tau}\right]_N$ repeat	$T_{1,1\alpha}^*, T_{1,2\alpha}^*, A_1, A_2, B_1, B_2$
niDALL	$\left[\boxed{1\alpha, \tau}\right]_N - \boxed{2\alpha, \tau}\right]_N$ repeat	α, T_1^*, M_0
D τ LL	$\left[\pi - \boxed{\alpha, \tau}\right]_N$ repeat then $\left[\pi - \boxed{\alpha, n\tau}\right]_N$ repeat	$T_{1,\tau}^*, T_{1,n\tau}^*, A_1, A_2, B_1, B_2$

Table 2.1: Acquisition schemes for the different Look-Locker approaches to flip angle mapping, with the parameters that are required in the non-linear least squares fitting of the transients.

2.3 Methods

All experiments were performed on a GE 3T human system using a transmit and receive quadrature head coil. In all DALL experiments, 8 dummy inversion- α -read-out trains were applied before imaging commenced to ensure the magnetization was in a dynamic steady-state. An RF spoiling scheme using a phase increment of 84° [26] was used to best approximate an ideally spoiled transient.

To produce the DALL flip angle maps, the background was masked out using an intensity cut-off on the first post inversion image. The time constants $T_{1,\alpha}^*$ and $T_{1,2\alpha}^*$ were then determined by non-linear least square fitting of the data to Equation 2.2. These T_1^* maps were then combined to produce the experimental flip angle using Equation 2.10 maps as describe above. The D τ LL approach is similar, but yields $T_{1,\tau}^*$ and $T_{1,n\tau}^*$ which are combined using Equation 2.18.

The non-inverted approach is different, in that the two recovery curves are fit simultaneously, using the parameters T_1 , M_0 and α to minimize the least squares parameter:

$$\chi_{ni}^2 = \sum_{i=1}^{N_{TI}} \left\{ [S_{\alpha,i} - S(t_i, T_1, M_0, \alpha)]^2 + [S_{2\alpha,i} - S(t_i, T_1, M_0, 2\alpha)]^2 \right\} \quad (2.19)$$

using the Levenberg-Marquardt algorithm. In this case, this is possible by substitut-

ing Equations 2.3 and 2.16 into 2.2.

2.3.1 Validation

A small cylindrical saline phantom (12 cm diameter) containing 9 samples doped with NiCl to T_1 values ranging from approximately 180 to 3000 ms was used to validate the proposed B_1^+ mapping techniques over a range of parameters. Such a small phantom is expected to show minimal B_1^+ artefact at 3 T. T_1 was measured using a 2D inversion prepared fast spin echo sequence, with a 128x128 imaging matrix over an FOV of 12 cm, and acquired at $TI = \{50,100,15,200,300,600,1200,2400,4000\}$ ms.

The imaging matrix for intDALL flip angle mapping was 42x42 in plane with 24 phase encodes in the slab selective direction, giving a resolution of approximately 3x3 mm in plane, with 10 mm thick slices. The accelerated 3D Look-Locker recovery was sampled with 192 RF pulses segmented into 8 effective TI volumes. The inversion was a 16 ms, 2kHz Silver-Hoult pulse [27], and the α pulses were 1 ms hard pulses. Inversion and α pulse amplitudes were initially set using the standard prescan for $\alpha = 6^\circ$, and then varied between 2° and 10° by modifying the transmit attenuation. The choice of imaging parameters is based on the optimization analysis conducted in Chapter 3.

For comparison to the DALL approach, an AFI map [10] based on the same imaging matrix and resolution as the DALL approach was acquired using the repetition times $TR_1/TR_2 = 15/75$ ms.

2.3.2 Slab Selection

An important aspect of this technique is its inherent ability to map the flip angle in a fully 3D sense. Not only do wavelength effects produce a non-uniform B_1^+ field leading to variations in flip angle, but coil geometries and RF pulse shapes also

cause non-uniform excitation. To investigate this property, a cylindrical, silicone oil phantom (dielectric constant = 2.75 [28]) was chosen to minimize wavelength effects. It had a diameter of 16 cm and length of 27 cm with a T_1 of 230 ms at 3 Tesla. The imaging matrix was 40x40 in plane, with 40 phase encodes in the slab selective direction. The FOV in plane was 20 cm, and a 20 cm thick slab was acquired in the slab selective direction, giving 5 mm isotropic voxels.

Two different 800 μ s, minimum phase pulses were investigated which included a 3 kHz bandwidth pulse and a 10 kHz bandwidth pulse, set to acquire an axial slab, with A/P frequency encode. In addition, to the shaped pulses, a hard pulse was also used to excite the phantom, which should give an RF profile independent measure of the flip angle. For this pulse, the frequency encode direction was set parallel to the axis of the phantom to prevent aliasing. The flip angle measured using the hard pulse could then be used to estimate the actual B_1^+ magnitude and act as a correction for theoretical slab profile simulations.

2.3.3 T_1 Correction

The Look-Locker methods were tested as a flip angle correction technique for 3D variable flip angle T_1 (DESPOT1) images in the head. The high resolution T_1 images were acquired using 1mm isotropic voxels (imaging matrix 220x220x160), $TR = 9$ ms, and $\alpha_{nom} = 4^\circ$ and 18° for a total scan time of approximately 11 minutes.

The flip angle mapping techniques investigated included intDALL, niDALL, D τ LL and AFI. All were acquired with 5mm isotropic voxels, and a matrix size of 44x44x32. In this way, the same volume, and the same RF pulse could be used to map the flip angle as used in the T_1 mapping technique. The DALL based methods were acquired with $\alpha_{nom} = 8^\circ$, $\tau = 3$ ms with a total scan time of 1min 10 sec using 8 effective TI volumes. The D τ LL technique was based on $\alpha_{nom} = 16^\circ$ and $\tau = 3$ and 12 ms with a scan time of approximately 3 min for 8 effective TI volumes. The AFI flip angle map was acquired with $\alpha_{nom} = 40^\circ$ using $TR_1/TR_2 = 30/150$ ms, with a scan time

of approximately 4 min 30 sec.

2.4 Results

2.4.1 The Phantom

The images that went into the formation of flip angle maps are shown in Figure 2.1. Figure 2.1(a) is a T_1 map based on the 2D inversion recovery data. The nine samples with T_1 values decreasing from approximately 3000 ms in the upper left to 180 ms in the lower right can be seen in this image. The slice was selected to give approximately the same location as the slice selected out of the 3D data set for the Look-Locker and AFI based images.

Figures 2.1(b) and 2.1(c) are the T_1^* maps from fitting 3 parameter inversion recovery equations to the Look-Locker recovery curves for sampling using 6° and 12° nominal flip angle pulses. Sampling with 12° pulses clearly leads to a shorter T_1^* value. There is also a significant amount of noise in the T_1^* measurement in the saline surrounding the samples. This is due to non-optimal sampling of the long T_1 transient, in addition to difficulty effectively spoiling the transverse magnetization with the long relaxation times of saline.

By combining the two Figures 2.1(b) and 2.1(c) it is possible to form the flip angle map in Figure 2.1(d) using Equation 2.10. For comparison, the AFI based map is shown in Figure 3.12(a). At 3T, minimal B_1^+ artefact is expected in this small saline phantom, and this appears to be borne out by both the DALL and AFI flip angle maps. The flip angles, whether measured using AFI or DALL, are fairly uniform and match the prescribed flip angle. Both however show increased noise and inaccuracy in the surrounding saline.

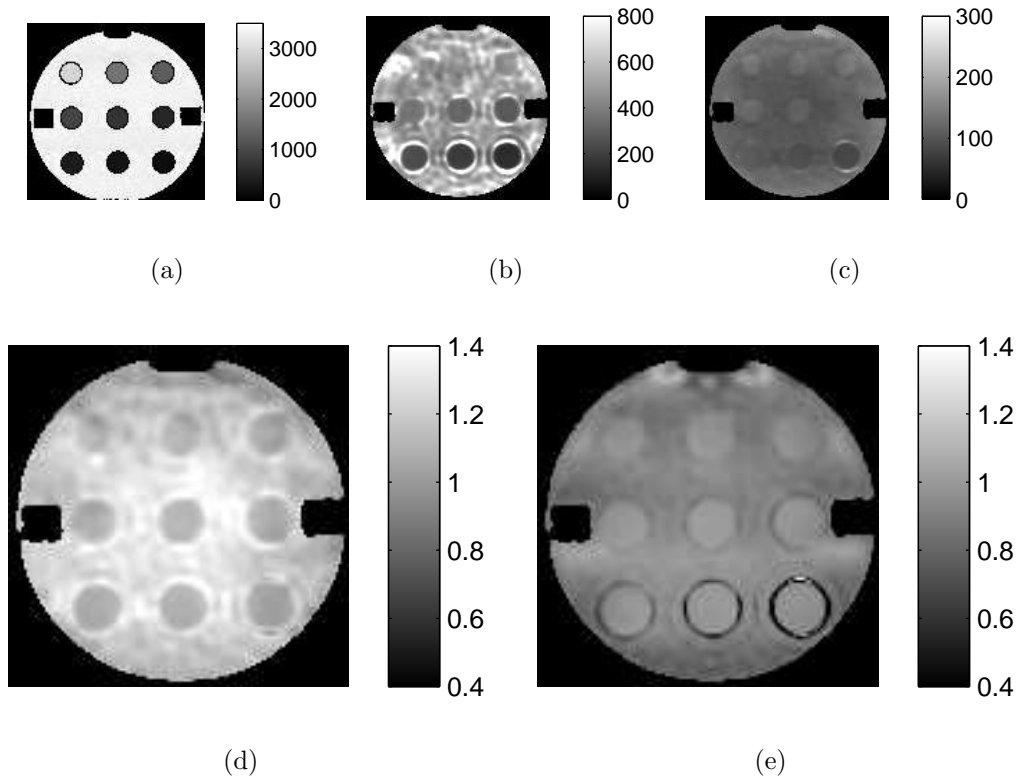


Figure 2.1: Cross section of the phantom containing multiple T_1 samples. (a) T_1 map in ms based on the 2D IR FSE images. (b) and (c) are the $T_{1,1\alpha}^*$ and $T_{1,2\alpha}^*$ maps in ms from fitting transients to the accelerated 3D Look-Locker acquisitions. (d) is the result of combining the $T_{1,1\alpha}^*$ and $T_{1,2\alpha}^*$ maps to form a flip angle map (α/α_{nom} with $\alpha_{nom} = 6^\circ$). (e) is a flip angle map using the AFI technique (α/α_{nom} with $\alpha_{nom} = 60^\circ$).

2.4.2 Transients

Representative transients for the different methods are shown in Figure 2.2 for a sample with a T_1 of 740 ms, and a nominal flip angle of 6° . The conventional DALL approach produces two transients as shown in Figure 2.2(a). The transient as sampled with the 1α pulses relaxes to a signal of approximately 10 arbitrary units (a.u.), and begins from approximately the inverse of this (-10 a.u.) due to the inversion applied at the end of the transient with minimal delays. The 2α transients show similar behaviour, but being sampled with larger pulses, have a shorter T_1^* and decay faster.

The effect of interleaving the 1α and 2α acquisitions is seen in Figure 2.2(b). The starting value of the 1α transient is based on the inversion of the M_z value at the end of the 2α transient, scaled by the ratio of the flip angles and vice versa. This leads to a slight reduction in the dynamic range of the 1α transient (recovers from -5 a.u. to 15 a.u.), but a significant increase in the dynamic range of the 2α transient.

The effect of omitting the preparation pulses entirely in an interleaved acquisition is shown in Figure 2.2(c). The transients still decay towards the same steady-state values as in the inversion prepared cases, but the starting values depend on the end state of the previous transient alone. For example, the starting value for the 1α transient is given by: $S_{1\alpha}(0) = (\sin 1\alpha / \sin 2\alpha) \cdot S_{2\alpha}(N_\alpha\tau)$. Collecting data in this way simplifies fitting somewhat as image phase need not be maintained, and it also removes any assumptions as to the accuracy of the inversion pulse.

In contrast to the double angle methods above, the dual repetition time approach leads to significantly different transients as shown in Figure 2.2(d). While only one flip angle is used, two values of the repetition time, τ , are used to sample the recovery and still lead to two different values for T_1^* . While τ is quadrupled in this implementation, the number of samples along the curve, N_α , remains the same leading to longer effective TI times.

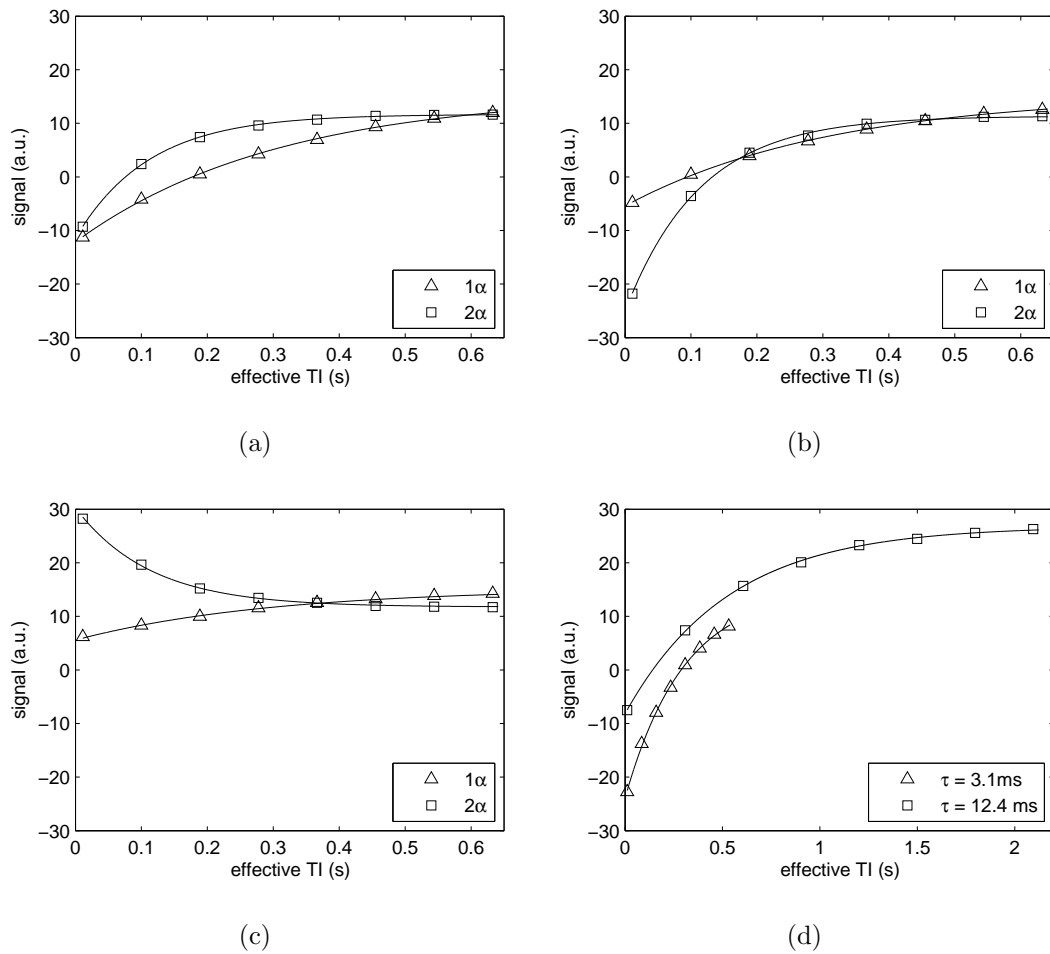


Figure 2.2: The transients measured in a sample with $T_1 = 740$ ms for the (a) DALL, (b) interleaved DALL, (c) non-inverted DALL and (d) $D\tau$ LL flip angle mapping techniques. The nominal 1α flip angle was 6° . Solid lines are the curves fit to the data points in the flip angle analysis.

2.4.3 Accuracy

The accuracy of the Look-Locker based methods are illustrated in Figure 2.3 where the measured flip angle is plotted against the nominal flip angle for a range of T_1 values. For a phantom of this size, at 3 Tesla, it is reasonable to assume that the nominal flip angle will match the actual flip angle fairly well.

All of the DALL methods lie along the $\alpha = \alpha_{nom}$ curve, with minimal deviations for tip angles in the range 2 to 8 degrees. The niDALL approach shows less deviation from the ideal response. Where the DALL and intDALL methods require fitting a total of 6 parameters, niDALL only requires 3, which is likely the cause of this better agreement. The $D\tau$ LL approach, however, appears to have significantly worse noise characteristics. All of the approaches, except the $D\tau$ LL approach, seem to become progressively less accurate at larger flip angles, showing a significant bias. This is a result of the breakdown of spoiling for the larger flip angles and short repetition times involved.

2.4.4 Slab Selection

An intensity filter was used to mask out regions with low signal prior to fitting for the flip angle. Full 3D maps of the flip angle were created of slabs excited using the three RF pulses described above. Theoretical slab profiles were calculated for the two shaped pulses using the prescribed slab thickness, the measured flip angle in the centre of the slab, and a smoothed version of the transmit coil profile as measured using the hard pulse as inputs to Bloch simulations. Figure 2.4(a) shows a flip angle image of the slab excited using the 10 kHz pulse. Despite the phantom extending outside the field of view in the horizontal direction, only the excited slab is visible in imaging, and here the contrast is set to highlight the ripple that is a result of the shaped pulse.

In Figure 2.4(b), slab profiles are plotted based on a central voxel. The non-

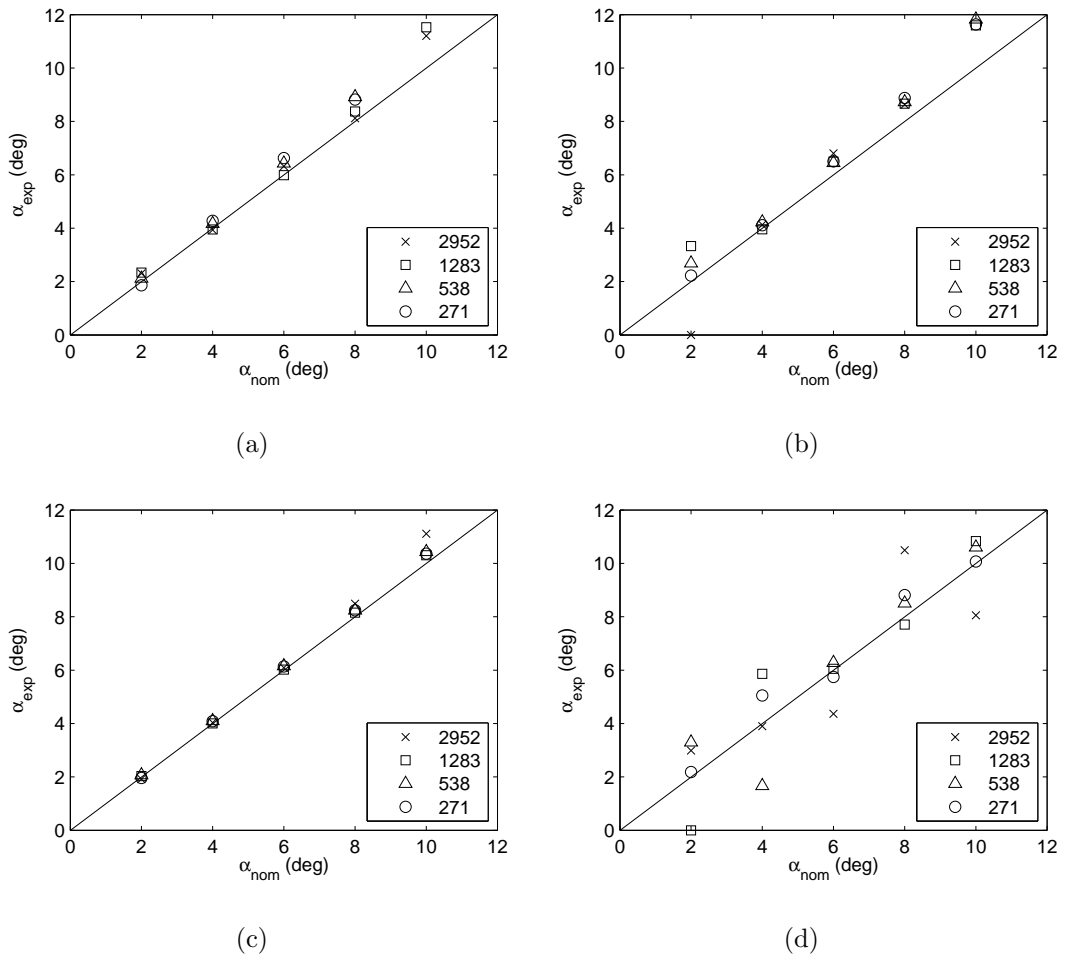


Figure 2.3: The accuracy of the Look-Locker based flip angle mapping techniques for T_1 values ranging from 271 to 2952 ms. (a) is the standard DALL implementation, (b) is the interleaved DALL, (c) is non inverted DALL using reduced parameter fitting, and (d) is an interleaved $D\tau$ LL approach.

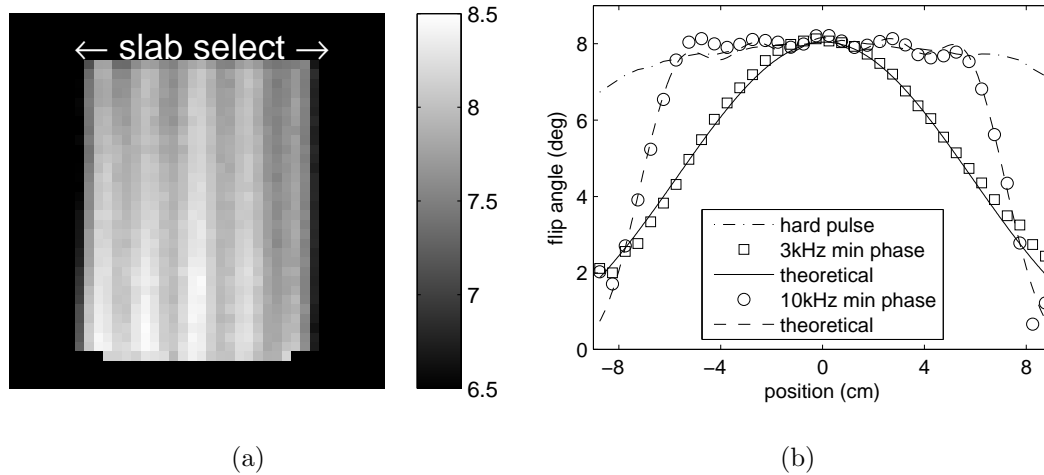


Figure 2.4: Sensitivity of DALL method to slab selective pulses. (a) shows an image of the flip angle in degrees across the slab excited with the 10kHz bandwidth pulse. Despite the phantom extending outside the imaged slab, only the excited slab is visible. (b) the experimentally measured slab profile matches the theoretical slab profile.

selective hard pulse profile remains relatively flat, only tailing off towards the ends of the coil. A second order polynomial was fit to the hard pulse profile for smoothing purposes. Bloch simulations were then used with the maximum observed flip angle, smoothed B_1^+ profile and prescribed slab thickness and overlaid with the experimentally measured slab profiles, showing very good agreement.

2.4.5 T_1 Correction

Axial and sagittal slices through the 3D flip angle maps in the brain are shown in Figure 2.5. The data were collected assuming sagittal images using a slab selective pulse. Thus in the sagittal plane, there is approximately a 20 % variation in flip angle due to wavelength effects. In the axial reformats, the profile of the slab selective pulse becomes apparent. This, combined with the wavelength effects, produces a nearly 50% variation in flip angle, primarily in the slab selective L/R direction.

In all these flip angle maps, the variation in flip angle is slow and smooth, as

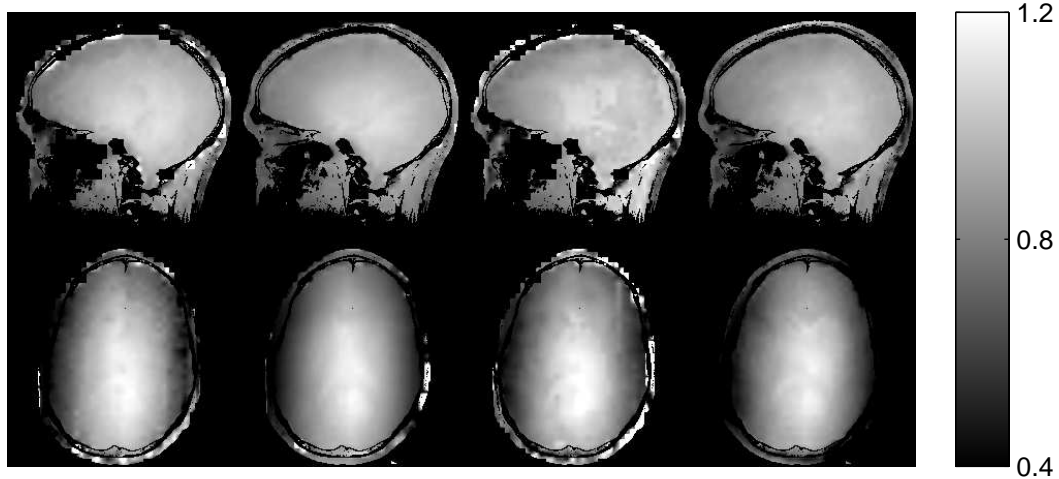


Figure 2.5: Flip angle maps for a sagittal (top row) and axial (bottom row) in the head at 3T. From left to right the methods of acquisition are intDALL, niDALL, D τ LL and AFI. Units are α/α_{nom} .

expected. In addition, there is only a slight indication of the cerebrospinal fluid in the ventricles, but otherwise there is no indication of the underlying anatomy, which is also expected. There is also good agreement between the different flip angle mapping techniques.

The T_1 maps produced by the variable flip angle technique are presented in Figure 2.6. The T_1 map produced by assuming the nominal 4° and 18° flip angles are achieved throughout is presented in the first column. This produces an underestimation of T_1 in the periphery of the brain due to the incorrect assumption of flip angle. This is most obvious in the axial image, but is also present in the sagittal image. If the flip angle is corrected using a map produced by the niDALL method in the middle column, the corrected T_1 images in the right column are produced. These have the slowly varying bias from the flip angle variation removed and correct T_1 values throughout.

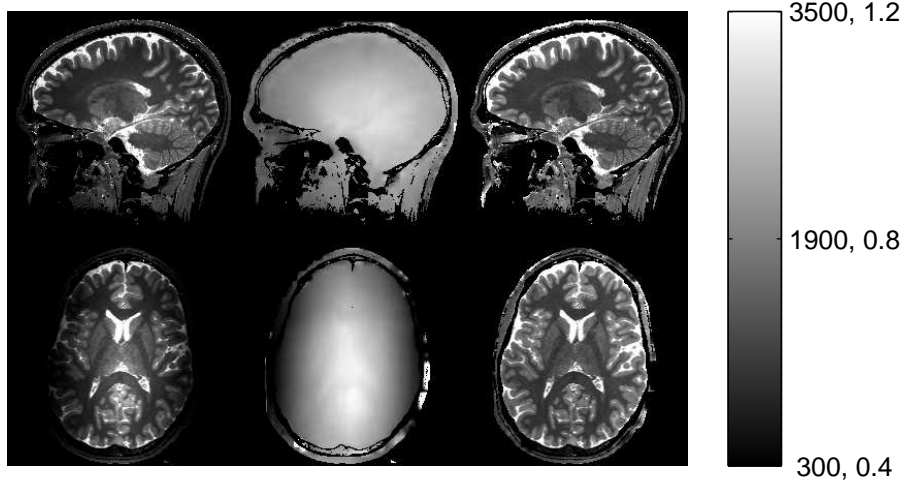


Figure 2.6: Sagittal (top row) and axial (bottom row) T_1 and flip angle maps in the head. The left column contains T_1 maps constructed assuming the nominal flip angles throughout the head. The middle column is the flip angle for the corresponding slices, and the right column is the flip angle corrected T_1 map. Units in ms for T_1 maps and α/α_{nom} for flip angle.

2.5 Discussion

Two of the primary limitations of the Look-Locker based approaches are illustrated in Figure 2.7. At low flip angles and/or long T_1 values, too little of the inversion recovery curve will get sampled to derive a useful T_1^* value. At the high flip angles and/or short T_1 values, the recovery may be largely done by the acquisition of the second effective TI volume. Inversion recovery curves are optimally sampled with TI samples that extend to approximately 3-4.5 times T_1^* [21]. In this case, the last sample is at 633 ms, but in Figure 2.7(a), $T_1^* \approx 660$ ms, and in Figure 2.7(b), $T_1^* \approx 58$ ms.

Figure 2.7(a) plots the transient for the non-interleaved Look-Locker acquisition with a nominal flip angle of 2° in a sample with a T_1 of 740 ms. This being a conventional Look-Locker acquisition, it would be expected that the transient should start at the inverse of where the previous one ends (i.e. it should start at approxi-

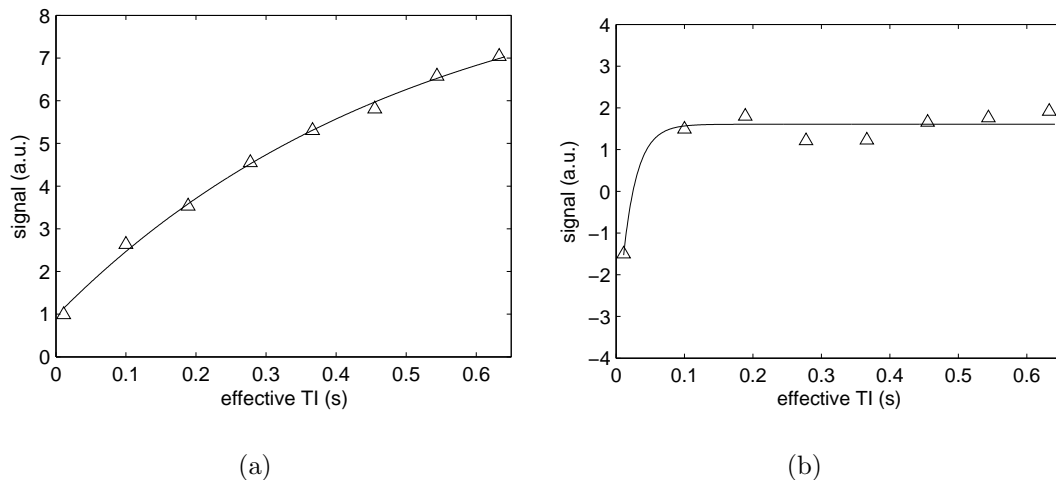


Figure 2.7: Sources of error in Look-Locker fitting. (a) Transient acquired with reduced B_1^+ ($\alpha = 2^\circ$) in a sample with $T_1 = 740$ ms. The reduced B_1^+ prevents complete inversion, and the TI points only sample a portion of recovery curve. (b) Transient acquired assuming large B_1^+ ($\alpha = 20^\circ$) in saline. The inversion pulse is effective, however, much of the exponential decay is complete by the second TI .

mately -7 arbitrary units (a.u)). This, however, is not the case. The inversion pulse amplitude was calibrated to a fixed value relative to the nominal 6° α pulse. Decreasing the B_1^+ amplitude either with destructive interference, or by increasing the transmit attenuation, as in this case, leads to a break-down of the adiabatic condition. Thus as the transmit field decreases, the inversion pulse may fail to effectively invert the magnetization. Unless high power inversion pulses are used, the inverted Look-Locker flip angle may reduce to the non-inverted case in the presence of large B_1^+ non-uniformities.

At the other extreme, especially in samples with long relaxation times, the transients cease to be well described by an exponential. Figure 2.7(b) is the transient for a nominal α of 20° acquired in a non-interleaved DALL acquisition in saline. Two things stand out in this transient. First, the T_1^* of this recovery is very short, and not well sampled by this sparsely sampled accelerated Look-Locker α -train. A smaller N_α and/or segmenting N_α into more TI volumes would be required to better sample the

transient. Second, the sampled points do not appear to lie along an exponential curve. The samples of the recovery curve are not well described by an exponential function, and these deviations cannot be accounted for by system noise alone. These deviations are the result of the breakdown of spoiling, which leads to a non-exponential transient, and thus an inaccurate T_1^* and α derived from it.

2.6 Conclusion

The accelerated 3D Look-Locker technique has been adapted to produce 3D flip angle maps using either a double angle or dual τ approach. The 3D nature of the method allows it to map the flip angle variations arising from wavelength effects and slab selective pulses, making it ideal for correcting quantitative 3D methods such as DESPOT. Given the typically slow variation in flip angle, low resolution flip angle maps can be acquired over the whole brain volume in approximately one minute, making this one of the faster B_1^+ mapping methods in existence.

References

- [1] de Moortele PFV, Akgun C, Adriany G, Moeller S, Ritter J, Collins CM, Smith MB, Vaughan JT, and Ugurbil K. B_1 destructive interferences and spatial phase patterns at 7 T with a head transceiver array coil. *Magn Reson Med* 2005; 54:1503–1518.
- [2] Deoni SC, Peters TM, and Rutt BK. High-resolution T_1 and T_2 mapping of the brain in a clinically acceptable time with DESPOT1 and DESPOT2. *Magn Reson Med* 2005;53:23—241.
- [3] Saekho S, Boada FE, Noll DC, and Stenger VA. Small tip angle three-dimensional tailored radiofrequency slab-select pulse for reduced B_1 inhomogeneity at 3 T. *Magn Reson Med* 2005;53:479–484.
- [4] Katscher U, Börnert P, Leussler C, and van den Brink JS. Transmit SENSE. *Magn Reson Med* 2003;49:144–150.
- [5] Ullmann P, Junge S, Wick M, Seifert F, Ruhm W, and Hennig J. Experimental analysis of parallel excitation using dedicated coil setups and simultaneous RF transmission on multiple channels. *Magn Reson Med* 2005;54:994–1001.
- [6] Insko E and Bolinger L. Mapping of the radiofrequency field. *J Magn Reson A* 1993;103:82–85.
- [7] Stollberger R and Wach P. Imaging of the active B_1 , field in vivo. *Magn Reson Med* 1996;35:246–251.
- [8] Cunningham CH, Pauly JM, and Nayak KS. Saturated double-angle method for rapid B_1+ mapping. *Magn Reson Med* 2006;55:1326–1333.
- [9] Dowell NG and Tofts PS. Fast, accurate, and precise mapping of the RF field in vivo using the 180° signal null. *Magn Reson Med* 2007;58:622–630.

- [10] Yarnykh VL. Actual flip-angle imaging in the pulsed steady state: A method for rapid three-dimensional mapping of the transmitted radiofrequency field. *Magn Reson Med* 2007;57:192–200.
- [11] Morrell GR. A phase-sensitive method of flip angle mapping. *Magn Reson Med* 2008;60:889–894.
- [12] Sacolick LI, Wiesinger F, Hancu I, and Vogel MW. B_1 mapping by Bloch-Siegert shift. *Magn Reson Med* 2010;63:1315–1322.
- [13] Oh C, Hilal S, Cho Z, and Mun I. Radio frequency field intensity mapping using a composite spin-echo sequence. *Magn Reson Imaging* 1990;8:21–25.
- [14] Lin W and Song HK. Improved signal spoiling in fast radial gradient-echo imaging: Applied to accurate T_1 mapping and flip angle correction. *Magn Reson Med* 2009;62:1185–1194.
- [15] Nehrke K. On the steady-state properties of actual flip angle imaging (AFI). *Magn Reson Med* 2009;61:84–92.
- [16] Yarnykh VL. Optimal radiofrequency and gradient spoiling for improved accuracy of T_1 and B_1 measurements using fast steady-state techniques. *Magn Reson Med* 2010;63:1610–1626.
- [17] Look D and Locker D. Time saving in measurement of NMR and EPR relaxation times. *Rev Sci Instrum* 1970;41:250–251.
- [18] Brix G, Schad LR, Deimling M, and Lorenz WJ. Fast and precise T_1 imaging using a TOMROP sequence. *Magn Reson Imaging* 1990;8:351–356.
- [19] Henderson E, Mckinnon G, Lee TY, and Rutt BK. A fast 3D Look-Locker method for volumetric T_1 mapping. *Magn Reson Imaging* 1999;17:1163–1171.

- [20] Nkongchu K and Santyr G. An improved 3-D Look-Locker imaging method for T_1 parameter estimation. *Magn Reson Imaging* 2005;23:801–807.
- [21] Crawley AP and Henkelman RM. A comparison of one-shot and recovery methods in T1 imaging. *Magn Reson Med* 1988;7:23–43.
- [22] Parker DL, Christian BA, Goodrich KC, Alexander A, Buswell H, and Yoon C. Improved accuracy in T1 measurements. *Proc 6th Annual Meeting ISMRM, Sydney, 1988 1998*;:2171.
- [23] Hsu JJ, Zaharchuk G, and Glover GH. Rapid methods for concurrent measurement of the RF-pulse flip angle and the longitudinal relaxation time. *Magn Reson Med* 2009;61:1319–1325.
- [24] Wade T and Rutt B. B1 correction using double angle Look-Locker (DALL). In: *Proceedings of the 16th Annual Meeting of the International Society of Magnetic Resonance in Medicine, Toronto, Canada 2008*;:1246.
- [25] Wade T and Rutt B. B1 correction using dual tau Look-Locker (D τ LL). In: *Proceedings of the 17th Annual Meeting of the International Society of Magnetic Resonance in Medicine, Honolulu, USA 2009*;:572.
- [26] Epstein FH, Mugler III JP, and Brookeman JR. Spoiling of transverse magnetization in gradient-echo (GRE) imaging during the approach to steady state. *Magn Reson Med* 1996;7:237–245.
- [27] Silver MS, Joseph RI, and Hoult DI. Highly selective $\pi/2$ and π pulse generation. *J Magn Reson* 1984;59:347–351.
- [28] Tofts P, Barker G, Dean T, Gallagher H, Gregory A, and Clarke R. A low dielectric constant customized phantom design to measure RF coil nonuniformity. *Magn Reson Imaging* 1997;15:69–75.

Chapter 3

Optimizing the Efficiency of Flip Angle Mapping Techniques

Abstract

Flip angle mapping is one approach to correcting B_1^+ transmit inhomogeneity problems, but it also has other applications. There currently exist many approaches to mapping the flip angle, and the actual flip angle imaging (AFI) and double angle methods (DAM) appear to be the most popular, while techniques based on the Look-Locker sequence are also showing promise. The noise in the resulting flip angle maps will depend on the noise in the raw images as well as the particular sequence parameters. The flip angle to flip angle noise ratio (ANR) is one useful metric for quantifying the quality of the techniques. A theoretical propagation of noise analysis is used to define an imaging efficiency based on the ANR achievable in a fixed scan time. The imaging parameters are optimized to produce the best ANR efficiency under a range of conditions for each of the techniques. The concept of imaging efficiency is then validated by comparing the predicted ANR to experimental values in vitro under a range of imaging conditions.

3.1 Introduction

There is currently a great deal of interest in mapping the excitation angle, α . This has been motivated by the trend towards higher main field magnets. These lead to improved SNR, but also require shorter wavelength radio frequency (RF) pulses, which lead to a non-uniform excitation field, B_1^+ , and consequently, α . Conventional quantitative and qualitative imaging approaches generally rely on the assumption that the excitation angle is uniform throughout the volume of interest. At field strengths up to and including 1.5 Tesla, volume coils have generally been able to achieve an excitation field, and thus an α profile, that is sufficiently uniform for most purposes. At 3 T and above, the wavelength in tissue becomes shorter, leading to destructive interference from coil elements in conventional coils [1], and thus a non-uniform B_1^+ and flip angle profile.

For imaging, a uniform excitation angle is desired over the field of view. Two factors prevent this. First, if the excitation field, B_1^+ , is non-uniform, either due to wavelength effects at high fields or simply a coil that produces a non-uniform B_1^+ field even in free space, even a non-selective hard pulse will not produce a uniform excitation. Secondly, any time slice or slab selective pulses are used, the selection profile of a finite duration pulse will not be a perfect rect function, also leading to a non-uniform excitation, even in the presence of a uniform B_1^+ field. In practice, the non-uniform excitation is due to a combination of both these influences, which are linked by $\alpha \propto B_1^+$, for hard pulses and selective pulses in the small tip angle regime [2]. The non-uniform excitation will lead to artefacts in 3D imaging and inaccuracies in quantitative imaging. Methods to correct the artefact, either through the use of custom pulses and coil combinations, or post processing, do exist, but mapping the excitation angle is a prerequisite.

Ideally, a flip angle mapping technique should be fast, accurate and precise, not be sensitive to variations in T_1 , T_2 or B_0 , and have a relatively large dynamic range.

Current methods for mapping the flip angle are typically based on image phase [3–5], or image amplitudes based on incremented radio frequency pulse amplitudes [6–10], or interleaved repetition times [11, 12].

The most commonly used techniques are the double angle methods (DAM) [7, 9] and the interleaved repetition, actual flip angle imaging (AFI) approach [12]. The double angle method itself is not easily adaptable to 3D imaging as it requires a long repetition time to avoid T_1 errors. This limitation can be overcome by the use of preparation pulses [8, 9]. The AFI approach is adaptable to 3D imaging, as the repetition times are by necessity short to avoid T_1 bias.

While these methods have become more widely adopted, there has been little effort made to compare or optimize their efficiencies. The AFI approach is based on an acquisition using interleaved repetition times, TR_1 and TR_2 , with a repetition time ratio in the range of 4–6, but little evidence has been provided to support this choice. Similarly, for the saturated double angle method (satDAM) [9], it is not clear what effect the saturation recovery time will have on the noise in the flip angle map.

In addition to the above cited approaches, it was recently suggested by us [13] and others [14] that the Look-Locker sequence [15, 16] could be adapted for flip angle imaging. This sequence has proven to be a highly time efficient technique for mapping T_1 , and was recently adapted to map α . The technique does however have a number of parameters that affect the noise in the α map.

The concept of imaging efficiency was previously used to compare and optimize quantitative T_1 imaging techniques [17]. By a propagation of noise analysis, it is possible to predict the noise that will be introduced into the derived quantitative measurement, under the assumption of a constant scan time. We sought to adapt this approach to flip angle mapping and to use it to optimize and compare existing techniques. We will limit our focus to the AFI and DAM approaches developed by others, and also include a comparison to the newly introduced Look-Locker methods developed in this Thesis. The above approach is general in nature, and requires no *a*

priori assumption of imaging scheme. As such it provides a fair technique to compare different approaches, assuming that they are acquired using the same voxel volume and total readout time.

3.2 Theory

This section follows the framework developed for the optimization of T_1 mapping sequences [17], which is adapted for flip angle mapping sequences here. The selection of an appropriate flip angle mapping technique depends on many factors. Image quality is typically assessed based on the signal to noise ratio (SNR). In the case of this Thesis, flip angle (α) maps are the goal, and a similar metric of image quality can be defined as the alpha to noise ratio (ANR):

$$ANR = \frac{\alpha}{\sigma_\alpha} \quad (3.1)$$

It is possible to define a dimensionless noise amplification factor, b , based on the propagation of noise from the signal to the derived flip angle:

$$b = \frac{\sigma_\alpha/\alpha}{\sigma_0/S_0} \quad (3.2)$$

Here S_0 represents the maximum theoretical signal, i.e. the signal obtained after a 90° pulse applied to fully relaxed magnetization, and σ_0 the noise in it. We use this hypothetical maximum signal for the intrinsic SNR, since it is otherwise impractical to define a signal value that has an equivalent meaning across the different flip angle mapping methods. α and σ_α represent the flip angle and noise in the flip angle that would be derived from the given flip angle mapping technique. b is thus determined by a theoretical analysis of noise propagation through the signal equation for any given imaging method.

The ANR in the image can then be expressed as:

$$ANR = \frac{S_0}{\sigma_0} \frac{1}{b} \quad (3.3)$$

$$= \frac{S'_0}{\sigma'_0} \frac{1}{b} \left(\frac{N_{rep}}{BW} \right)^{1/2} V \quad (3.4)$$

where S'_0/σ'_0 is the hypothetical signal acquired with a single repetition with unit bandwidth of a voxel with unit volume. BW and V represent the actual imaging acquisition bandwidth and voxel volume, and $N_{rep} = N_{ex}N_{pe}$ represents the signal averaging associated with imaging, with N_{ex} signal averages for N_{pe} phase encodes. The technique imaging time is thus given by $T_{exam} = N_{rep}T_{seq}$, and T_{seq} represents the time required to acquire all necessary repetitions of a single line in k-space for that particular technique.

Since we are interested in comparing the ANR of the derived flip angle maps of different techniques in a fixed imaging time and using equivalent spatial encoding schemes, setting T_{exam} , BW , V and S'_0/σ'_0 to unity will result in a measure of imaging efficiency, defined as ANR per unit total scan time, per unit intrinsic SNR, given by:

$$\Gamma = \frac{1}{b} \frac{1}{\sqrt{T_{seq}}} \quad (3.5)$$

Thus the efficiency will depend on the measure of effective sequence repetition time given by T_{seq} , and the dimensionless noise propagation value b , which is determined by the sequence timing and relaxation parameters.

The above is based on the assumption that one line of k-space is acquired with each sampling pulse, which can impose restrictive constraints on the sequence timing. If echo planar (EPI), or parallel imaging were used to accelerate the imaging with an acceleration factor R , and the bandwidth correspondingly increased to maintain the same readout window, the accelerated bandwidth would be $BW_{EPI} = R \times BW$. To keep T_{exam} constant, either N_{ex} would have to be increased by R , or the sequence timings (e.g. TR) would have to be increased and N_{ex} held constant. The first option dictates that sequence timings would have to be held constant, and thus b would not change, for no net gain in efficiency. The second option would have an efficiency reduced by $1/\sqrt{R}$, due to the increased bandwidth, with no corresponding increase in

N_{rep} , and this would compete with any improvement in b due to the eased restrictions (i.e. lengthening) of sequence timings in b .

3.2.1 DAM Efficiency

The double angle method (DAM) is based on the ratio of two signal intensities obtained using an RF pulse at a nominal flip angle of α or 2α [7,8]. Assuming that a long repetition time ($TR = 5T_1$) is used to ensure the magnetization preceding each pulse is the same, the signal intensities, S_1 and S_2 , will be given by:

$$S_1 = S_0 \cos \alpha \quad (3.6)$$

$$S_2 = S_0 \cos 2\alpha \quad (3.7)$$

these can then be combined to determine the actual flip angle achieved:

$$\alpha = \arccos\left(\frac{S_2}{2S_1}\right) \quad (3.8)$$

Propagation of noise (see Appendix 3.7.1) would then result in a noise propagation factor of:

$$b_{DAM} = \left(\frac{1}{\alpha^2} \frac{1}{4 \sin^2 \alpha - \sin^2 2\alpha} \left(\frac{\sin^2 \alpha + \sin^2 2\alpha}{\sin^2 \alpha} \right) \right)^{1/2} \quad (3.9)$$

An alternative technique is to use a saturation pulse followed by a fixed recovery time T_{SR} , thus providing the same magnetization to precede each pulse without the need for full recovery [9].

$$\{[SatPrep - T_{SR} - \alpha] - [SatPrep - T_{SR} - \alpha] -\}_{repeat}$$

The signals would then be given by:

$$S_1 = S_0 (1 - \exp(-T_{SR}/T_1)) \sin \alpha \quad (3.10)$$

$$S_2 = S_0 (1 - \exp(-T_{SR}/T_1)) \sin 2\alpha \quad (3.11)$$

The flip angle would still be calculated using Eq 3.8, but would result in a noise propagation factor of:

$$b_{satDAM} = \frac{1}{(1 - \exp(-T_{SR}/T_1))} b_{DAM} \quad (3.12)$$

If the long TR method is used, two repetitions of $TR = 5T_1$ would be required, and thus, the effective sequence time, T_{seq} , would be $2 \cdot 5 \cdot T_1$. If the saturation preparation is used instead, the input signal, and thus efficiency, would be scaled by $1/(1 - \exp(-T_{SR}/T_1))$, where T_{SR} is the time allowed after the saturation for recovery. Assuming that the time required to excite and collect signal outside of the saturation time, is short compared to the T_{SR} , (i.e. the next saturation pulse follows closely after the α pulse), T_{seq} would then be given by $2 \cdot T_{SR}$.

Combining the above, the efficiencies of the double angle methods would be given by:

$$\Gamma_{DAM} = \frac{\alpha}{\sqrt{10T_1}} \left((4 \sin^2 \alpha - \sin^2 2\alpha) \left(\frac{\sin^2 \alpha}{\sin^2 \alpha + \sin^2 2\alpha} \right) \right)^{1/2} \quad (3.13)$$

$$\Gamma_{satDAM} = (1 - \exp(-T_{SR}/T_1)) \left(\frac{5T_1}{T_{SR}} \right)^{1/2} \Gamma_{DAM} \quad (3.14)$$

Thus, the efficiency of the satDAM method is affected by two competing factors. Short saturation recovery times lead to a reduced signal, thereby reducing the efficiency by the factor $(1 - \exp(-T_{SR}/T_1))$, which competes with the decreased imaging time that increases efficiency by the factor $1/\sqrt{T_{SR}}$. In fact, it holds that the efficiency of the satDAM method is only greater than the DAM method when $(1 - \exp(-T_{SR}/T_1))\sqrt{5T_1/T_{SR}} > 1$ which is approximately the case when $T_{SR} < T_1/5$.

3.2.2 AFI Efficiency

The actual flip angle imaging (AFI) [12] technique employs an interleaved TR acquisition. Two images are acquired using two repetition times, TR_1 and TR_2 , with $TR_2 > TR_1$, that are interleaved.

$$\{[\alpha - TR_1 - \alpha - TR_2] -\}_{repeat}$$

These produce two images, S_1 , from the short TR_1 window and S_2 from the longer TR_2 window, with different contrast:

$$S_1 = S_0 \sin \alpha \frac{1 - E_{1,2} + (1 - E_{1,1}) E_{1,2} \cos \alpha}{1 - E_{1,1} E_{1,2} \cos^2 \alpha} \quad (3.15)$$

$$S_2 = S_0 \sin \alpha \frac{1 - E_{1,1} + (1 - E_{1,2}) E_{1,1} \cos \alpha}{1 - E_{1,1} E_{1,2} \cos^2 \alpha} \quad (3.16)$$

where $E_{1,1} = \exp(-TR_1/T_1)$, and $E_{1,2} = \exp(-TR_2/T_1)$. If the repetition times are assumed to be short relative to the longitudinal relaxation, the ratio of these, $r = S_2/S_1$, can be used to determine the flip angle:

$$\alpha = \arccos \left(\frac{rn - 1}{n - r} \right) \quad (3.17)$$

where $n = TR_2/TR_1$.

The propagation of noise factor (see Appendix 3.7.2) is then given by:

$$b = \frac{1}{\alpha \sin \alpha} \left(\left(\frac{1 - E_{1,1} E_{1,2} \cos^2 \alpha}{1 - E_{1,2} + (1 - E_{1,1}) E_{1,2} \cos \alpha} \right)^2 \frac{(n^2 - 1)(r^2 + 1)}{(1 - r^2)(n - r)^2} \right)^{1/2} \quad (3.18)$$

and the sequence will have an effective sequence time given by $T_{seq} = TR_1 + TR_2$.

This results in a flip angle mapping efficiency given by:

$$\Gamma_{AFI} = \frac{\alpha \sin \alpha}{\sqrt{TR_1 + TR_2}} \times \dots \left(\left(\frac{1 - E_{1,2} + (1 - E_{1,1}) E_{1,2} \cos \alpha}{1 - E_{1,1} E_{1,2} \cos^2 \alpha} \right)^2 \frac{(1 - r^2)(n - r)^2}{(n^2 - 1)(r^2 + 1)} \right)^{1/2} \quad (3.19)$$

3.2.3 Double Angle Look-Locker

Compared to the above methods, Look-Locker based flip angle mapping techniques have many more parameters that influence the flip angle imaging efficiency. This, combined with the error propagation through the non-linear least squares fitting process, makes the derivation of imaging efficiency a tedious endeavour. The procedure is outlined here, but for a full discussion, the reader is directed to the Thesis Appendix. The efficiency is determined by T_1 , the separation of sampling pulses τ ,

flip angle α , and the segmentation of the transient, based on N_α samples along the recovery curve, into N_{TI} effective inversion time images. This gives an acceleration factor of N_α/N_{TI} .

The Look-Locker technique has been shown to be a very efficient technique for measuring T_1 [17], with a peak efficiency nearly equal to that of inversion recovery techniques, but applicable in a very short scan time.

The flip angle as given by the double angle Look-Locker (DALL) method is given by [13,14]:

$$\alpha = \arccos\left(\frac{1}{4}\left(E_\Delta + \sqrt{E_\Delta + 8}\right)\right) \quad (3.20)$$

with

$$E_\Delta = \exp\left(-\tau\left(\frac{1}{T_{1,2\alpha}^*} - \frac{1}{T_{1,1\alpha}^*}\right)\right) \quad (3.21)$$

where $T_{1,1\alpha}^*$ and $T_{1,2\alpha}^*$ are the driven inversion recovery time constants measured by least squares fitting to the Look-Locker recovery curves, based on sampling with a train of 1α or 2α pulses, and are related to T_1 and α by:

$$T_{1,1\alpha}^* = \frac{1}{T_1} - \frac{\ln(\cos 1\alpha)}{\tau} \quad (3.22)$$

$$T_{1,2\alpha}^* = \frac{1}{T_1} - \frac{\ln(\cos 2\alpha)}{\tau} \quad (3.23)$$

The noise amplification factor (see Appendix 3.7.3) is then give by:

$$b = \frac{E_\Delta \tau}{\alpha} \frac{\partial \alpha}{\partial E_\Delta} \left(\left(\frac{b_{1\alpha}^*}{T_{1,1\alpha}^* DR_1} \right)^2 + \left(\frac{b_{2\alpha}^*}{T_{1,2\alpha}^* DR_2} \right)^2 \right)^{1/2} \quad (3.24)$$

where

$$\frac{\partial \alpha}{\partial E_\Delta} = \left(16 - \left(E_\Delta + \sqrt{E_\Delta^2 + 8} \right)^2 \right)^{-1/2} \left(1 + \frac{E_\Delta}{\sqrt{E_\Delta^2 + 8}} \right) \quad (3.25)$$

where $DR_{1,2}$ is the dynamic range of the exponential recovery curves (defined for these purposes as $(S(\infty) - S(0))/S_0$), and b^* is the noise amplification factor for the

T_1^* values assuming 3 parameter fitting to an inversion recovery equation, defined as:

$$b^* = \frac{\sigma_{T_1^*}/T_1^*}{\sigma_0/DR} \quad (3.26)$$

The full expansion of b^* is presented in [17], and is also included in Thesis Appendix A.

Here we have to distinguish between the standard implementation of Look-Locker imaging and the accelerated technique. In conventional Look-Locker imaging, the recovery is sampled N_α times with the low flip angle pulses, and these samples are used to form $N_{TI} = N_\alpha$ images along the recovery curve. In accelerated Look-Locker imaging, the samples can be grouped so that $N_{TI} < N_\alpha$, thus giving an acceleration factor of N_α/N_{TI} .

The double angle accelerated 3D Look-Locker imaging techniques require N_{TI} reconstructed images along the recovery curve, acquired twice (once using 1α tip angles and once using 2α tip angles). This gives an effective sequence time, $T_{seq} = 2 \cdot \tau \cdot N_{TI}$. The effective sequence time may be slightly longer than this due to the time required for the inversion prep pulses, but for purposes of simplicity it is assumed these are short compared to the time taken for the sampling pulses.

Thus the double angle Look-Locker methods have an efficiency given by:

$$\Gamma_{DALL} = \frac{1}{\sqrt{2\tau N_{TI}}} \frac{\alpha}{E_\Delta (\partial\alpha/\partial E_\Delta)} \left(\left(\frac{b_{1\alpha}^*}{T_{1,1\alpha}^* DR_1} \right)^2 + \left(\frac{b_{2\alpha}^*}{T_{1,2\alpha}^* DR_2} \right)^2 \right)^{-1/2} \quad (3.27)$$

where the efficiency depends on the sampling of the two recovery curves via the b^* values and DR values. The b^* values will be determined by the sampling of the recovery curves and do depend on the starting or ending values of the transients, and the DR values will be determined by the order in which the two curves are sampled as well as the nature of the preparation pulses. In the following sections three different ordering and preparation pulse schemes are introduced and efficiency formulae derived.

3.2.3.1 Non-Interleaved Inverted DALL

Typically, for the accelerated 3D Look-Locker method, each α -pulse-train is followed immediately by the next inversion α -pulse-train, and this conventional approach will just be referred to as DALL.

$$\left\{ \pi - [\alpha - \tau -]_{N_\alpha} \right\}_{\text{repeat}}$$

After a complete image (or k-space) data set is fully collected using α pulses, a second would be acquired using 2α pulses.

$$\left\{ \pi - [2\alpha - \tau -]_{N_\alpha} \right\}_{\text{repeat}}$$

The familiar inversion recovery equation that is fit independently to the two transients is:

$$S(t) = A + (B - A) \exp\left(-\frac{t}{T_1^*}\right) \quad (3.28)$$

where A is the steady-state that the signal is decaying towards given by the equation:

$$A = S_0 \frac{1 - E_\tau}{1 - E_\tau \cos \alpha} \sin \alpha \quad (3.29)$$

$$E_\tau = \exp(-\tau/T_1) \quad (3.30)$$

The starting value, B will depend on the delays introduced by the inversion pulse, as well all of the samples along the recovery curve [16]. If the inversion pulse is assumed to be short relative to T_1 relaxation, it can be approximated by setting

$$S(0) \approx -S(N_\alpha \tau) \quad (3.31)$$

giving the result

$$B \approx -A \frac{1 - \exp(-N_\alpha \tau/T_1^*)}{1 + \exp(-N_\alpha \tau/T_1^*)} \quad (3.32)$$

and thus a dynamic range

$$\begin{aligned} DR &= A - B \\ &= A \left(\frac{2}{1 + \exp(-N_\alpha \tau/T_1^*)} \right) \end{aligned} \quad (3.33)$$

In this implementation of the dual angle LL method, a total of six parameters will be fit: A_1 , B_1 and $T_{1,1\alpha}^*$ for the transient acquired with 1α pulses, and A_2 , B_2 and $T_{1,2\alpha}^*$ for the transient acquired with 2α pulses.

3.2.3.2 Interleaved Inverted DALL

The interleaved DALL (intDALL) method interleaves the 1α and 2α recovery trains:

$$\left\{ \pi - [\alpha - \tau -]_{N_\alpha} - \pi - ([2\alpha - \tau -]_{N_\alpha} -) \right\}_{\text{repeat}}$$

so that both 1α and 2α data set acquisitions are interleaved into one sequence. This has the effect that it makes the dynamic range of the transients in the two acquisitions more similar, and may make the DALL technique less sensitive to changes in T_1 or flip angle.

Thus, if the 1α acquisition is governed by the equation $S_{1\alpha}(t) = A_1 + (B_1 - A_1) \exp(-t/T_{1,1\alpha}^*)$ and the 2α acquisition by $S_{2\alpha}(t) = A_2 + (B_2 - A_1) \exp(-t/T_{1,2\alpha}^*)$, the signal for the 1α acquisition will recover from B_1 , towards, but not necessarily reach A_1 , while the 2α acquisition will recover from B_2 which will be determined by the end of the 1α train.

$$\begin{aligned} B_1 &= -\sin \alpha M_{z,2\alpha}(N_\alpha \tau) \\ B_2 &= -\sin 2\alpha M_{z,1\alpha}(N_\alpha \tau) \end{aligned} \quad (3.34)$$

Solving these gives:

$$A_1 = S_0 \frac{1 - E_\tau}{1 - E_\tau \cos \alpha} \sin \alpha \quad (3.35)$$

$$A_2 = S_0 \frac{1 - E_\tau}{1 - E_\tau \cos 2\alpha} \sin 2\alpha \quad (3.36)$$

$$B_1 = \frac{-(\sin \alpha / \sin 2\alpha) A_2 (1 - E_{2\alpha}) + A_1 E_{2\alpha} (1 - E_{1\alpha})}{(1 - E_{1\alpha} E_{2\alpha})} \quad (3.37)$$

$$B_2 = \frac{-(\sin 2\alpha / \sin \alpha) A_1 (1 - E_{1\alpha}) + A_2 E_{1\alpha} (1 - E_{2\alpha})}{(1 - E_{1\alpha} E_{2\alpha})} \quad (3.38)$$

$$E_{1\alpha} = \exp\left(-\frac{N_\alpha \tau}{T_{1,1\alpha}^*}\right) \quad (3.39)$$

$$E_{2\alpha} = \exp\left(-\frac{N_\alpha \tau}{T_{1,2\alpha}^*}\right) \quad (3.40)$$

where the dynamic range is still given by $A_1 - B_1$ for the 1α acquisition, and $A_2 - B_2$ for the 2α acquisition, but now B_1 and B_2 depend on the dynamics of both transients.

3.2.3.3 Interleaved Non-Inverted DALL

There is a third option. The transients may be acquired in an interleaved sense, but with the inversion pulses omitted (niDALL):

$$\left\{ [\alpha - \tau -]_{N_\alpha} - [2\alpha - \tau -]_{N_\alpha} - \right\}_{\text{repeat}}$$

As in the interleaved DALL acquisition scheme above, the end of the 1α -pulse-train acts as the preparation for the 2α -pulse-train and vice versa. The equations for interleaved non-inverted DALL still apply, but B_1 and B_2 are replaced with:

$$\begin{aligned} B_1 &= \frac{(\sin \alpha / \sin 2\alpha) A_2 (1 - E_{2\alpha}) + A_1 E_{2\alpha} (1 - E_{1\alpha})}{(1 - E_{1\alpha} E_{2\alpha})} \\ B_2 &= \frac{(\sin 2\alpha / \sin \alpha) A_1 (1 - E_{1\alpha}) + A_2 E_{1\alpha} (1 - E_{2\alpha})}{(1 - E_{1\alpha} E_{2\alpha})} \end{aligned} \quad (3.41)$$

Flip angle maps may still be produced as above by fitting for A_1 , A_2 , B_1 , B_2 , $T_{1,1\alpha}^*$ and $T_{1,2\alpha}^*$, but removing the inversion pulse decreases the dynamic range of the transients and may lead to poorer efficiency. However, now that the assumption of an infinitely short, perfect inversion is no longer required, the equations become exact and it is possible to fit directly for 3 parameters: T_1 , α and S_0 .

The propagation of noise into T_1 , α and S_0 by directly fitting for these parameters is not as straight forward as fitting for $T_{1,1\alpha}^*$ and $T_{1,2\alpha}^*$ independently. There is no closed form solution to work from. Instead, the propagation of noise into the flip angle was solved using the symbolic math toolbox of Matlab, and the expressions are included in Appendix A of the Thesis.

3.2.4 Dual τ Look-Locker

So far we have only considered running the accelerated Look-Locker sequence using two different values for the flip angle, α and 2α . It is possible to extract the same information using a dual τ approach (D τ LL). The transients can be acquired using the same flip angle, but with a different spacing between the α pulses [14, 18]. An interleaved acquisition would look like this:

$$\left\{ \pi - [\alpha - \tau_1 -]_{N_\alpha} - \pi - [\alpha - \tau_2 -]_{N_\alpha} - \right\}_{\text{repeat}}$$

The flip angle will then be given by:

$$\alpha = \arccos(E_\Lambda) \quad (3.42)$$

with:

$$E_\Lambda = \exp\left(-\frac{n\tau_1}{n-1}\left(\frac{1}{T_{1,\tau}^*} - \frac{1}{T_{1,n\tau}^*}\right)\right) \quad (3.43)$$

where $\tau = \tau_1 = \tau_2/n$ with $n > 1$. The two repetition times lead to the two recovery constants, $T_{1,\tau}^*$ and $T_{1,n\tau}^*$, in an effective sequence time of $T_{seq} = (n+1)N_{TI}\tau$. This expression leads to a noise amplification factor given by:

$$b = \frac{1}{\alpha} \frac{n\tau}{n-1} \frac{E_\Lambda}{\sqrt{1-E_\Lambda^2}} \left(\left(\frac{b_\tau^*}{T_{1,\tau}^* DR_\tau} \right)^2 + \left(\frac{b_{n\tau}^*}{T_{1,n\tau}^* DR_{n\tau}} \right)^2 \right)^{1/2} \quad (3.44)$$

where the b^* values are the dimensionless noise propagation factors for the T_1^* values as given in the Appendix.

In principle the same options available for DALL are available for D τ LL; in other words, the two different T_1^* values may be acquired using sequential, interleaved or non-inverted acquisitions as with the double angle methods above. However, for the sake of brevity, only the interleaved, inverted acquisition scheme will be considered.

3.3 Methods

The relevant imaging parameters for each technique were varied to investigate what affect they would have on the theoretical efficiency of each flip angle mapping technique. The goal was to find the set of parameters that would optimize the efficiency, Γ , and thus ANR for a given scan time. With each technique thus optimized, they could then be compared in terms of efficiency over a desired range of excited flip angles.

A 12 cm diameter cylinder containing NiCl samples, with T_1 values ranging from 185 ms to 2950 ms, was used to validate the calculated efficiencies over a range of parameters. The 3D imaging matrix for the AFI and Look-Locker techniques was 42x42, with 24 slices, with an FOV of 12 cm in plane and 1 cm thick slices to cover the entire volume of the phantom. Imaging parameters were then optimized to achieve the maximum ANR in a one minute scan. Multiple repeats were then used to estimate the noise in the estimated flip angle, and therefore ANR in the resulting flip angle maps.

A one minute scan with $42 \times 24 = 1008$ phase encode lines and no averaging leads to a T_{seq} of 60 ms. For the AFI technique, the one minute scan time limitation implies $TR_1 + TR_2 = 60$ ms, thus to maximize n , subject to a minimum TR constraint of 5ms, TR_1/TR_2 was set to 5/55 ms. The flip angle was set to a nominal value of $\alpha = 60^\circ$, and varied by changing the transmit attenuation.

For the Look-Locker experiments, imaging timing parameters were chosen to optimize efficiency for a one minute scan based on 8 effective TI points and a T_1 of 1500 ms. To achieve a one minute scan, τ was set to 3.7 ms, and N_α to 608 and 328 for intDALL and niDALL respectively. Image SNR (S_0/σ_0) and the resulting ANR (based on Eq. 3.3) were estimated using multiple repeats for each of the techniques. S_0 was estimated using the value determined from the niDALL technique. A hard pulse with a nominal flip angle of 4° ($2\alpha = 8^\circ$) was used as the nominal α pulse, and the flip

angle was then varied between 2° and 12° by changing the transmit attenuation.

3.4 Results

3.4.1 Double Angle Method Optimization

The basic double angle method itself requires a repetition time of $5T_1$ to avoid bias. For a 3D data set this would lead to an excessively long scan, unless accelerated read-out techniques such as EPI or spiral acquisitions are used. The saturated double angle (satDAM) method employs a saturation reset pulse with a customizable delay before the imaging pulses, to allow faster sequence acquisition. The delay determines the available longitudinal magnetization and scan time.

This extra delay allows the sequence to be run more quickly without incurring a bias, but also leads to an efficiency that varies with the recovery delay time as can be seen in Figure 3.1(a). The optimum value for T_{seq} is approximately $2.5T_1$, which corresponds to $T_{SR} = 1.25T_1$. This would still lead to a long scan, and speeding up the acquisition by choosing a shorter repetition time will lead to a reduction in efficiency.

The optimum efficiency achievable at different α values is shown in Figure 3.1(b). The conventional double angle method with a TR of $5T_1$ is shown, and indicates that the saturated DAM has a higher efficiency. Both approaches, though, appear to achieve their optimum efficiency when $\alpha = 96^\circ$. This contrasts slightly with how the sequence is normally run. Normally only the signal amplitude is considered, and the flip angle must be kept below 90° to avoid an undetermined solution. If the signal phase is maintained, then $S_{2\alpha}/S_{1\alpha}$ can become negative and produce valid results for flip angles above 90° .

A critical drawback of these double angle methods is that optimum efficiency is only achieved with relatively long repetition times, leading to long scan times.

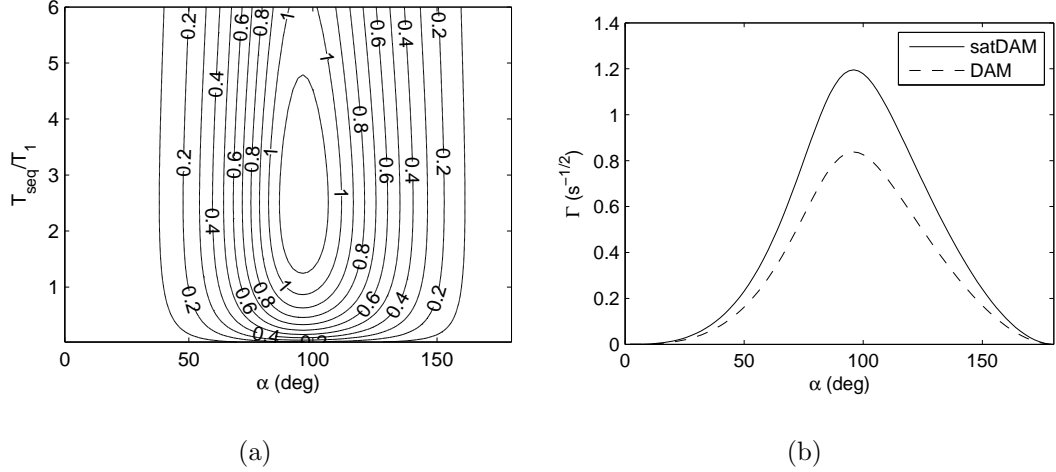


Figure 3.1: Optimum efficiency (in $\text{s}^{-1/2}$) available using the double angle methods. (a) Efficiency at different recovery times for the saturated DAM and (b) the optimized efficiency of the saturated DAM compared to conventional DAM.

Reducing the scan time by shortening the recovery delay time leads to a significant decrease in scanning efficiency. Alternatively, an accelerated readout could be used to acquire images more rapidly. This could make the DAM feasible in a reasonable scan time, and allow the satDAM technique to be run with longer T_{SR} times. Doing this would lead to a more optimal T_{SR} but would also decrease the SNR due to the higher bandwidth of the EPI train. These two influences will be examined further when exploring efficiency in a restricted scan time.

3.4.2 AFI Optimization

Optimization of the AFI technique is more complex than the DAM methods. Rather than optimizing just one recovery time parameter (T_{SR} for satDAM), there are now two recovery times that need to be considered, TR_1 and TR_2 , also expressed as TR_1 and $n = TR_2/TR_1$. The original implementation [12] recommended $TR_1 < TR_2 < T_1$ with n between 4 and 6, and flip angles in the range 20° to 80° .

From Figure 3.2(a) it appears that these values may not be optimal. The optimum

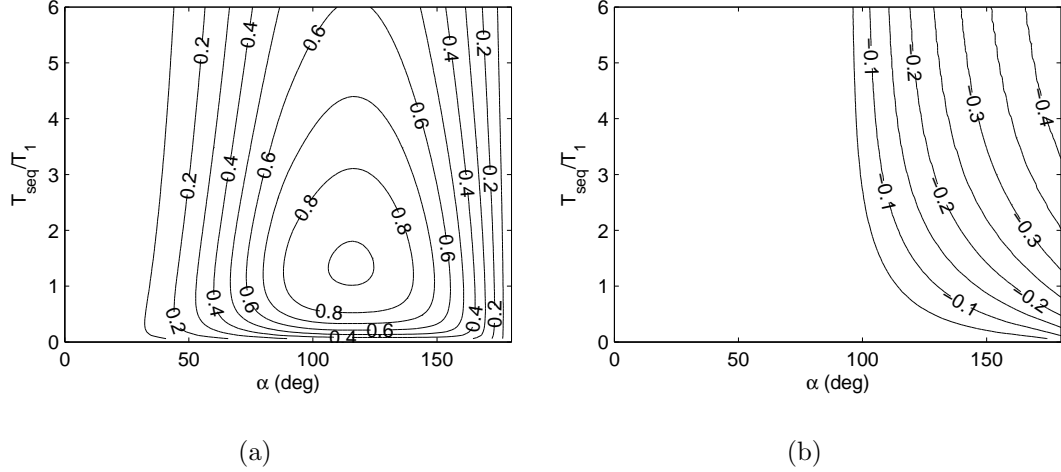


Figure 3.2: Efficiency of AFI with n optimized. (a) Efficiency (Γ in $s^{-1/2}$) at different values of T_{seq} and α with n optimized for each combination, and (b) the error $((\alpha_{AFI} - \alpha)/\alpha)$ associated with the optimum efficiency).

efficiency occurs at $\alpha = 116^\circ$, for a T_{seq} value of $1.3T_1$ with $n = 7.4$ (i.e. $TR_1/TR_2 = 232/1718$ ms for $T_1 = 1500$ ms). This however will lead to a significant inaccuracy, as indicated in Figure 3.2(b), in the measurement of α , as the assumption that $TR_1 < TR_2 < T_1$ will no longer be valid. Moving to shorter repetition times will reduce this problem, but at the expense of efficiency. Alternatively, n may be increased to reduce bias with minimal effect on efficiency.

The n value required to produce the optimum efficiency shown in Figure 3.2(a) depends on the particular T_{seq} and α combination. This is shown in Figure 3.3 for a $T_{seq} = 1.3T_1$. At low flip angles (below approximately 90°), the efficiency is relatively insensitive to n but the optimum choice for n is as large as possible (i.e. TR_1 a minimum). At larger flip angles, a value closer to $n = 5$ may be better in terms of efficiency, but comes at the expense of a larger error as shown in Figure 3.3(b). Maximizing n will maximize the efficiency at low flip angles, ensure the least bias regardless of the flip angle, and will only lead to a minor decrease in efficiency at the largest flip angles.

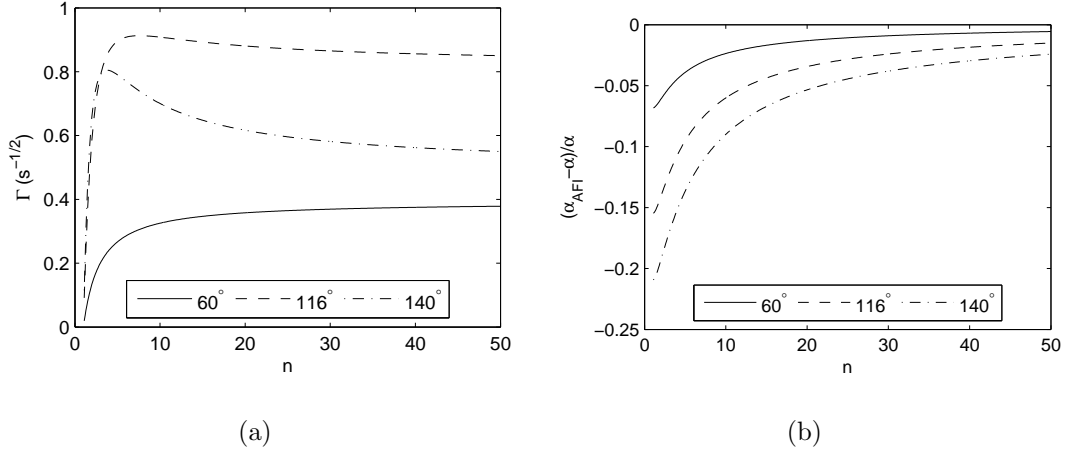


Figure 3.3: (a) Efficiency and (b) error of the AFI technique as a function of n , with $T_{seq} = 1.3T_1$. Low flip angles ($< 90^\circ$) are optimized when n is maximized. At higher flip angles this behavior changes.

In addition, it should be noted that with n maximized (i.e. TR_1 a minimum), the sequence begins to behave like another method based on two approximately 90° pulses in rapid succession [11]. The first pulse tips the magnetization into the transverse plane, and the second follows very shortly after the first to sample the residual longitudinal magnetization. It can be shown that for $TR_1 \ll T_1$ the AFI equation reduces to:

$$\alpha = \arccos\left(\frac{S_2}{S_1}\right) \quad (3.45)$$

which matches the solution in [11].

As in the double angle methods, the AFI method achieves its optimum scan time with a T_{seq} value that would lead to a very long scan for a 3D data set if no accelerated imaging were used. Reducing the scan time is possible either by reducing the repetition times and thus T_{seq} , with a resulting loss in efficiency, or by using accelerated imaging which permits a more optimum T_{seq} , but with reduced SNR.

3.4.3 Double Angle Look-Locker Optimization

The parameter space of the DALL techniques was explored by varying the repetition time (τ), length of the α -pulse-train, (N_α) and the flip angle (α) to find the optimum efficiency for each T_{seq} and α combination. The T_1 was set to 1500 ms, and N_{TI} to 8.

Figure 3.4 shows the dependence of the relative efficiency, Γ , of the DALL and $D\tau$ LL techniques on τ and flip angle. For each point, N_α is optimized to give the best efficiency, and in the case of $D\tau$ LL, n is optimized as well. Based on these, it would appear that the best efficiency is achieved with fairly long τ values at large flip angles. At this point N_α is restricted to N_{TI} , and the technique ceases to be accelerated and reduces to a conventional Look-Locker approach. This is also at the limit of the validity of the DALL approach. For $\alpha = 45^\circ$, $2\alpha = 90^\circ$ and $T_{1,2\alpha}^* = 0$ to which no valid exponential can be fit. At this limit, the optimum choice of τ is around $0.2T_1$, which for 32 view and 32 slice encodes, and $N_{TI} = 8$ effective TI images, would lead to a 3 hour scan, unless some sort of accelerated imaging is used.

The best achievable efficiency (τ , N_α and n optimized) at any given flip angle is shown in Figure 3.5. The benefit of moving to an interleaved acquisition is shown by the increase in efficiency across the entire range. It is also apparent that reducing the number of parameters fit in the niDALL approach, by removing the inversion pulse, more than compensates for reduced dynamic range in the transients, and leads to an efficiency that is even better still.

However, as can be seen in Figure 3.5, the optimum achievable efficiency does not depend strongly on the flip angle. Thus choosing a shorter repetition time, and a correspondingly smaller nominal flip angle can lead to a much shorter scan, with minimal reduction in efficiency.

The τ and N_α values required to achieve optimum performance are presented in Figure 3.6 for the niDALL method. From Figure 3.6(a), it is clear that lower flip angles allow a shorter repetition time, and hence total scan time, with minimal

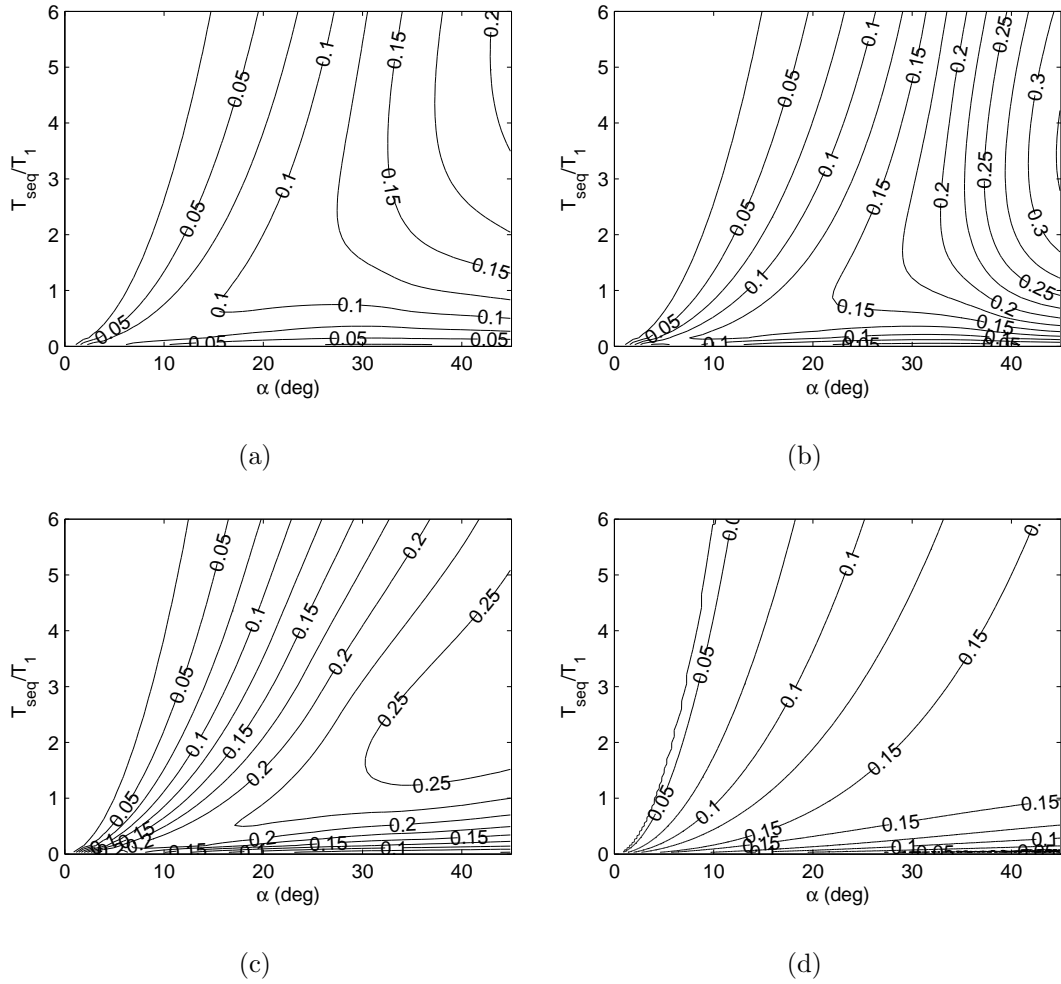


Figure 3.4: Optimal flip angle mapping efficiency (in $s^{-1/2}$) achievable using the accelerated 3D Look-Locker sequence for different repetition time, and flip angle combinations. (a) efficiency based on a sequential acquisition of α and 2α , (b) interleaved DALL, (c) non-inverted DALL, fitting reduced parameter set, and (d) interleaved D τ LL acquisition.

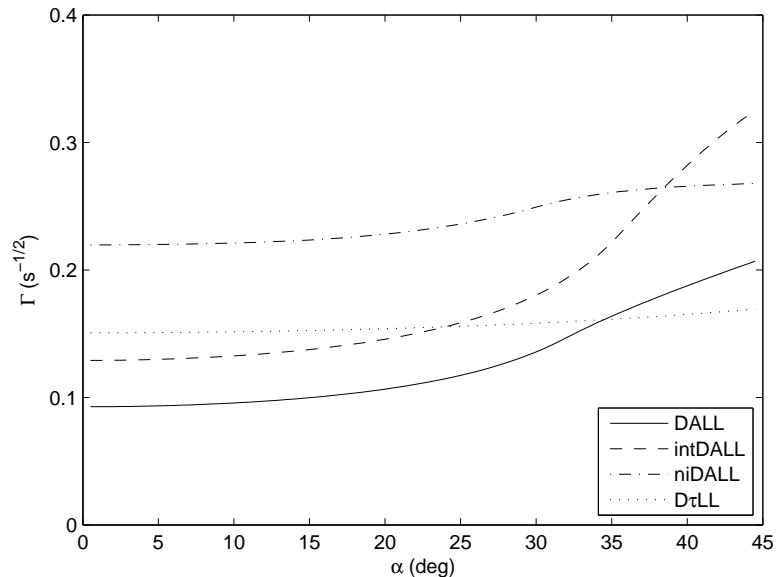


Figure 3.5: The best efficiency of the Look-Locker based methods achievable at each flip angle, assuming all other parameters are optimized for that flip angle.

reduction in efficiency. These shorter repetition times and flip angles, lead to a slower transient recovery curve, which is best sampled by many α pulses as indicated by Figure 3.6(b).

The best choice of flip angle, if the τ value is set based on scan time, can be found by observing that the ratio of the flip angle to the Ernst angle based on the desired τ value is nearly constant in Figure 3.6(c). Similarly, the number of α pulses to optimally sample the recovery train is based on observing that the ratio of the time taken to sample the recovery (τN_α) to the modified recovery constant ($T_{1,1\alpha}^*$) is also relatively constant in Figure 3.6(d). While only the results for the niDALL method are presented in Figure 3.6, the other DALL based methods display similar behaviour, and the optimum imaging parameters can be found based on the values in Table 3.1. In Figure 3.6 there is a discontinuity in the optimum parameter values at approximately 30° . This is due to the fact that above this angle, the sequence ceases to operate as an accelerated acquisition and the parameters are limited by the

restriction $N \geq N_{TI}$, with N_{TI} fixed at eight as outlined below.

	α/α_{Ernst}	$N_{\alpha}\tau/T_{1,1\alpha}^*$
DALL	0.94	3.35
intDALL	1.21	3.73
niDALL	1.19	1.93

Table 3.1: Optimum imaging parameters for the various DALL flip angle mapping techniques.

3.4.4 Optimizing the Number of Effective TI Images

For the Look-Locker based techniques we have so far been assuming $N_{TI} = 8$. This is partially based on [19], but it is also possible to demonstrate how efficiency depends on N_{TI} with N_{α} and all other parameters fixed.

As can be seen in Figure 3.7(a), the efficiency increases up to approximately $N_{TI} = 8$ and then begins to fall off very slightly. With insufficient points along the transient, the exponential fitting is a poorly determined system, and very sensitive to noise. Above a certain threshold, (approximately $N_{TI} = 8$) additional points along the transient begin to act just like additional averages, and so, while they may reduce the noise in the fit parameters, it will come at the expense of scan time, for minimal net effect on efficiency.

For the DALL and intDALL techniques that require fitting a total of 6 parameters, the optimum N_{TI} value is closer to 8, whereas for the niDALL technique that relies on fitting only 3 parameters, fewer points are necessary (an optimum closer to 4).

While increasing the number of effective TI images beyond a certain point may not lead to an increase in efficiency, it will lead to an increase in the dynamic range of the techniques. This is illustrated in Figure 3.7(b) for the DALL and niDALL techniques. With the technique optimized for peak efficiency, points are spaced along each transient to minimize the noise propagated into the flip angle for that set of parameters. Moving away from this optimum, the efficiency begins to drop off, due

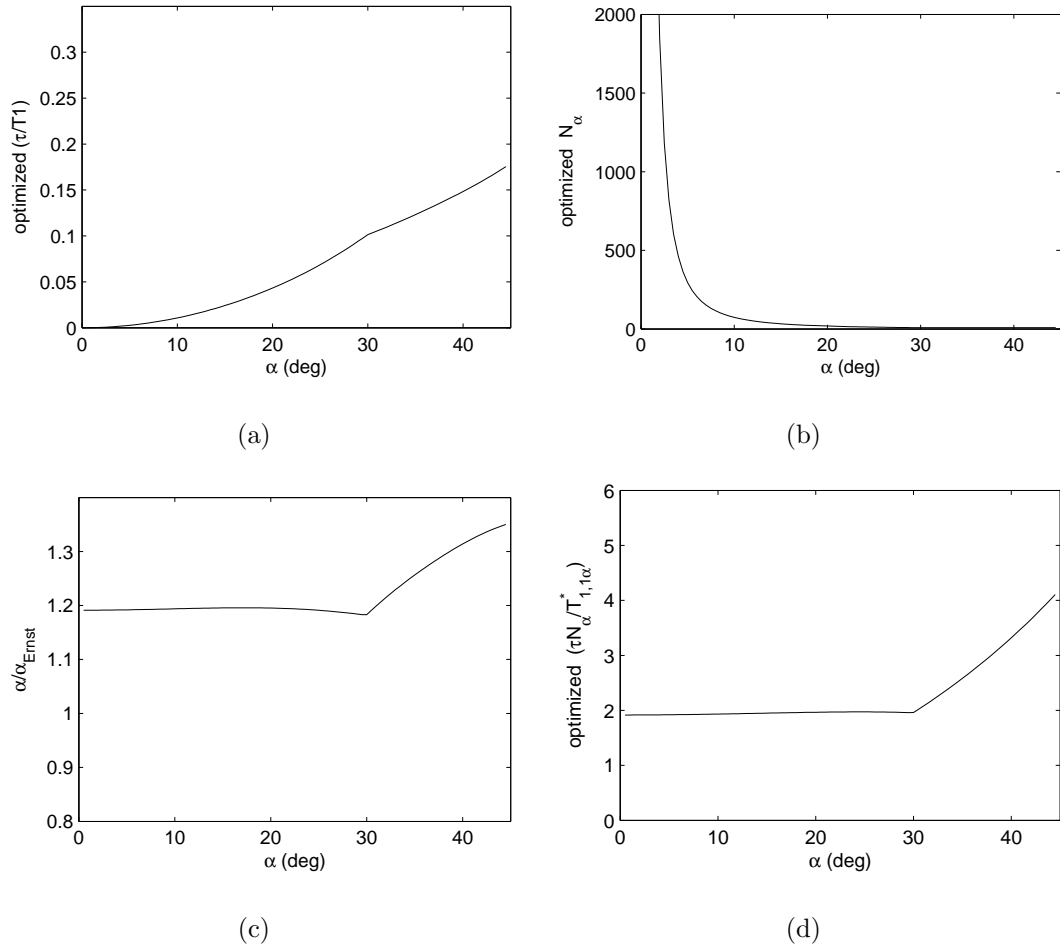


Figure 3.6: Parameters required to optimize the niDALL method. (a) The optimum repetition time is lower with decreasing flip angle. (b) Lower flip angles with correspondingly shorter repetition times require longer read-out trains. (c) The ratio of the flip angle to the Ernst angle based on optimum efficiency at that angle is relatively constant, as is (d) the time taken for the read-out train relative to the T_1^* for that angle.

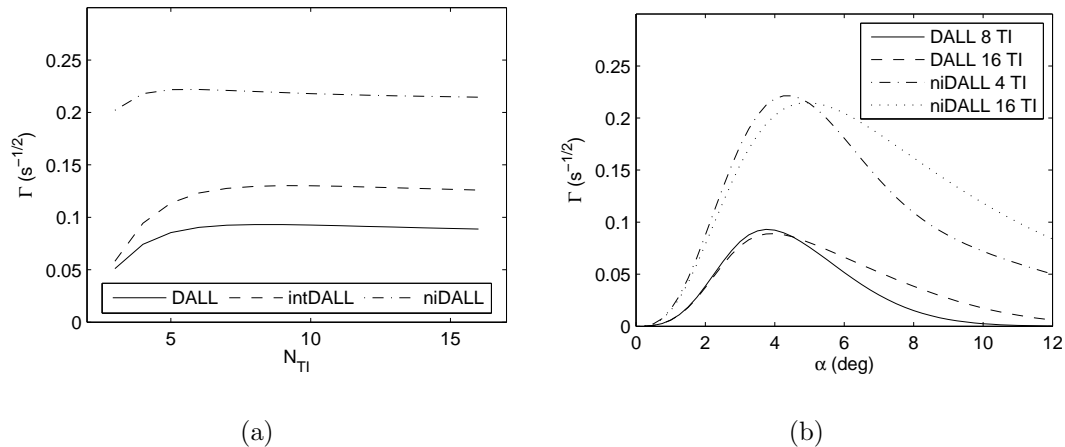


Figure 3.7: Effect of the number of effective T_I images on the flip angle mapping efficiency of Look-Locker methods with τ set to 3.7 ms. (a) Efficiency is independent of N_{T_I} above a certain threshold as the additional T_I volumes behave like averages N_α and α are fixed. (b) The additional T_I volumes lead to a broader flip angle sensitivity with N_α fixed.

to the points no longer optimally sampling the curves. Increasing N_{T_I} ensures that, even away from the optimal sampling condition, the curves are sampled adequately.

3.4.5 T_1 Sensitivity

Up to this point we have been assuming a fixed T_1 . Typically, tissues with long T_1 values are the most challenging with regard to flip angle mapping. If the sequence is optimized to acquire an acceptable flip angle map at the largest T_1 predicted to exist within the volume, it will likely also produce acceptable results for shorter T_1 values, even if not optimized for those.

Figure 3.8 shows the efficiency of a niDALL technique optimized for a 1 minute scan and a T_1 of 1500 ms. Even though the technique is optimized for a long T_1 value, it will produce an even better ANR at shorter T_1 values. The ANR will be as good or better than the value at 1500 ms for T_1 's ranging from approximately 300 ms to 1500 ms. The dynamic range will also be better at shorter T_1 values over most of this

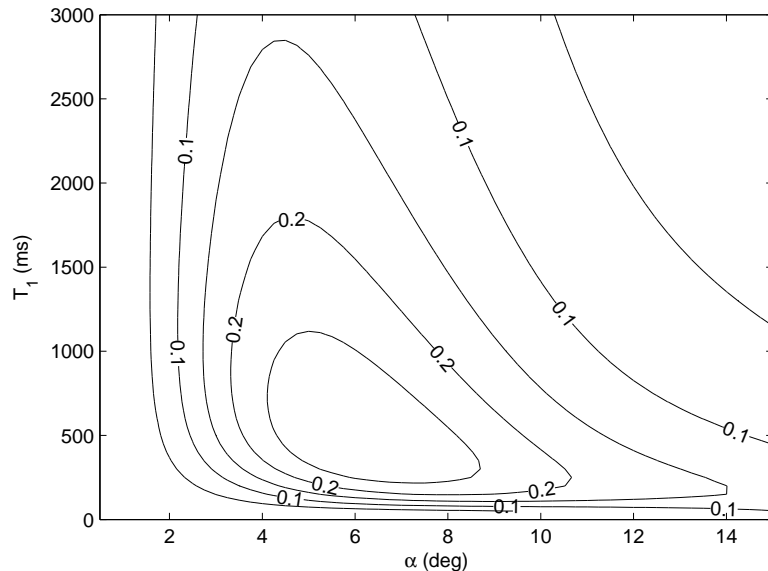


Figure 3.8: Efficiency (in $s^{-1/2}$) of the niDALL technique optimized for a T_1 of 1500 ms over a range of T_1 and flip angle values ($\tau = 3.7$ ms, $N_{TI} = 8$, $N_\alpha = 328$).

range.

3.4.6 Practical Scan Time

So far we have investigated the optimum achievable efficiency of the above methods without any concern as to how long they will actually take to scan. Neglecting the actual scan time would seem to suggest that either the double angle or AFI techniques have the advantage with peak efficiencies of approximately 1.2 and 0.9 $s^{1/2}$ respectively, compared to the Look-Locker methods with efficiencies on the order of 0.25 $s^{1/2}$. However all of the above techniques appear to have an optimum efficiency with parameters that would require a scan on the order of hours to acquire a 3D data set.

Based on Figure 3.4 it appears that it may be possible to run the DALL methods with shorter repetition times with minimal loss in efficiency. On the other hand, shortening the overall scan time would appear to lead to a significant loss in efficiency

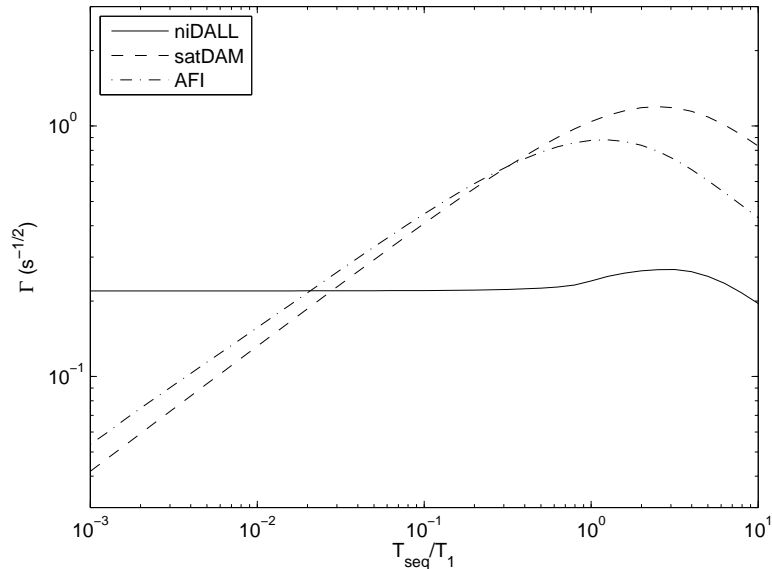


Figure 3.9: Optimized efficiency as a function of restricted effective sequence time for the niDALL, AFI and satDAM flip angle mapping techniques.

of the DAM or AFI methods. This effect is highlighted in Figure 3.9 which shows the optimized efficiency as a function of the effective sequence time, T_{seq} , of each sequence. The efficiency of the DALL methods is relatively insensitive to T_{seq} . The AFI and satDAM methods have an efficiency that improves with T_{seq} , and only exceeds the efficiency of the niDALL method above a certain threshold (approximately $T_{seq} = 0.025T_1$). This implies that for fast imaging especially in the presence of long T_1 values, niDALL may be the best choice. For example, for a 3D scan with approximately 1000 total phase encode lines (32×32 or 42×24), and a sample T_1 of 2000 ms, this implies niDALL would be the optimal choice for scan times below 50 s.

Flip angle or B_1^+ mapping is required to set optimal amplitudes and phases of multiple transmit ports for B_1^+ shimming, or to design rf pulses for fully parallel transmit methods [20–22]. For these applications, flip angle maps in times on the order of a minute or less are needed. For this comparison, we will assume a maximum scan time of one minute for a scan with 42 views and 24 slice encodes (1008 total

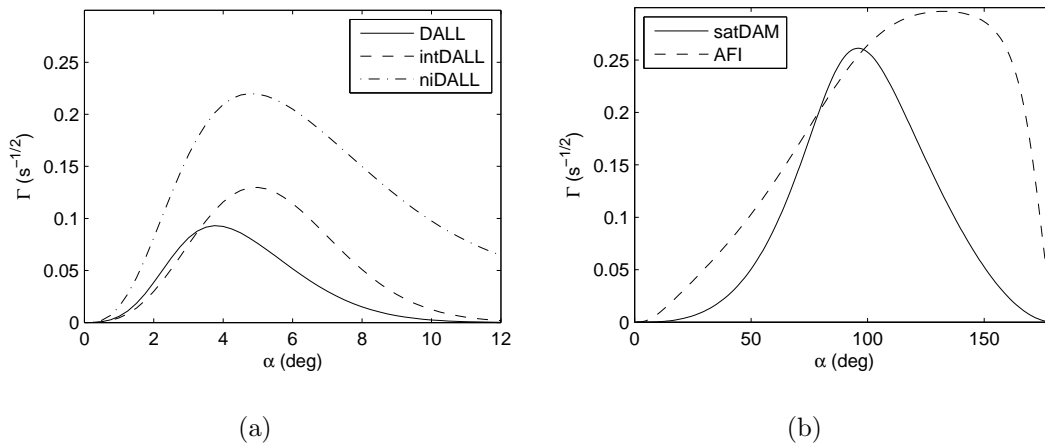


Figure 3.10: Efficiency of flip angle mapping techniques with a scan time limited to one minute for (a) the DALL techniques, and (b) the AFI and DAM techniques.

phase encodes).

Imaging parameters were chosen to maximize the ANR for a T_1 of 1500 ms and a scan time restricted to one minute (i.e. $T_{seq} \approx 0.04T_1$). The optimum sequence parameters were set based on this value, and only the flip angle varied. This provides an estimation of the dynamic range of the different techniques, as well as their relative ANR performance.

The results of restricting the scan time to one minute are shown in Figure 3.10. From these, it is clear that, while AFI or the DAM may have a higher peak efficiency, with a limited scan time the accelerated 3D Look-Locker based methods, and in particular the niDALL technique offer an almost equally efficient map of the flip angle.

Rather than reducing the repetition times to achieve a one minute scantime, it is also possible to use accelerated imaging such as EPI. The acceleration due to EPI allows an increase in repetition times so that $T_{seq} \propto ETL$. This leads to two competing effects. The longer T_{seq} values lead to higher efficiency for the satDAM and AFI methods, and could make conventional DAM feasible, but SNR is reduced

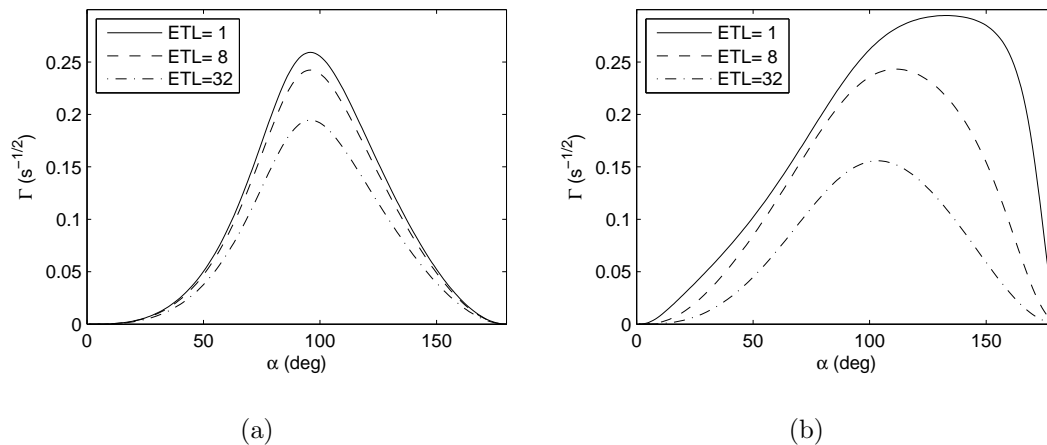


Figure 3.11: Effect of EPI acceleration on the efficiency of the (a) satDAM and (b) AFI methods.

due to the need to increase bandwidth to maintain the same read-out window, which leads to a decrease in efficiency. This decrease in efficiency is proportional to $R^{-1/2}$, and in Figure 3.9, the slope of the satDAM and AFI methods is never greater than 0.5, or in other words slower than a square root law. This implies that using EPI to permit longer T_{seq} values will not lead to a net gain in efficiency. This is further illustrated in Figure 3.11 for the proposed one minute scan. An ETL of 32 would allow a $T_{seq} = 1.27T_1$, which is near optimum for the AFI and satDAM methods, but does not yield a net increase in efficiency.

3.4.7 Experimental Validation

The flip angle maps based on optimum imaging parameters for the AFI and niDALL techniques are shown in Figure 3.12. The nominal flip angle to produce the AFI map in Figure 3.12(a) was 120° , and the locations of the different T_1 doped phantoms are evident by a slightly different flip angle from the surrounding saline. The noise in this image is indicated by the ANR map shown in Figure 3.12(b). Here it is clear that the noise in the flip angle map is dependent on the T_1 , producing a low

ANR for the longest T_1 samples (upper left, 2950 ms), and improving with decreasing T_1 to the lower right (185 ms).

The flip angle map based on the niDALL technique in Figure 3.12(c) is based on $\alpha_{nom} = 6^\circ$. This leads to the ANR map in Figure 3.12(d), which indicates an ANR approximately equal to the ANR of the AFI technique, where T_1 is long, but does not improve much with shorter T_1 values. In both flip angle maps, there appears to be minimal B_1^+ inhomogeneity, which is expected for a small phantom at 3 Tesla.

The model of noise propagation was validated by comparing the ANR predicted by noise propagation based on the measured signal to noise and the scan time to the experimentally measured values over a range of imaging parameters, using multiple repeats to acquire the above images. These are presented in Figure 3.13 for the AFI and niDALL techniques. The AFI approach has an efficiency advantage in short T_1 samples, but where T_1 becomes large, the niDALL approach matches the AFI technique, but at significantly lower flip angles. There is also reasonable agreement between the theoretically predicted and experimentally measured ANR for both techniques, indicating that the noise propagation theory is an acceptable method of optimizing and comparing the techniques.

There does appear to be additional error present in the AFI technique (Figure 3.13(b)). This is most likely due to imperfect spoiling. The improved AFI spoiling scheme [23] was implemented, but may not have been sufficient, particularly at the higher flip angles.

3.5 Discussion

The AFI and DAM methods are often run ensuring $\alpha < 90^\circ$ to avoid the need to maintain image phase. As the results in this chapter show, there are potential benefits to be had by running the techniques at higher flip angles. The DAM methods appear to give a peak efficiency at flip angles around 96° , while the AFI method is optimized

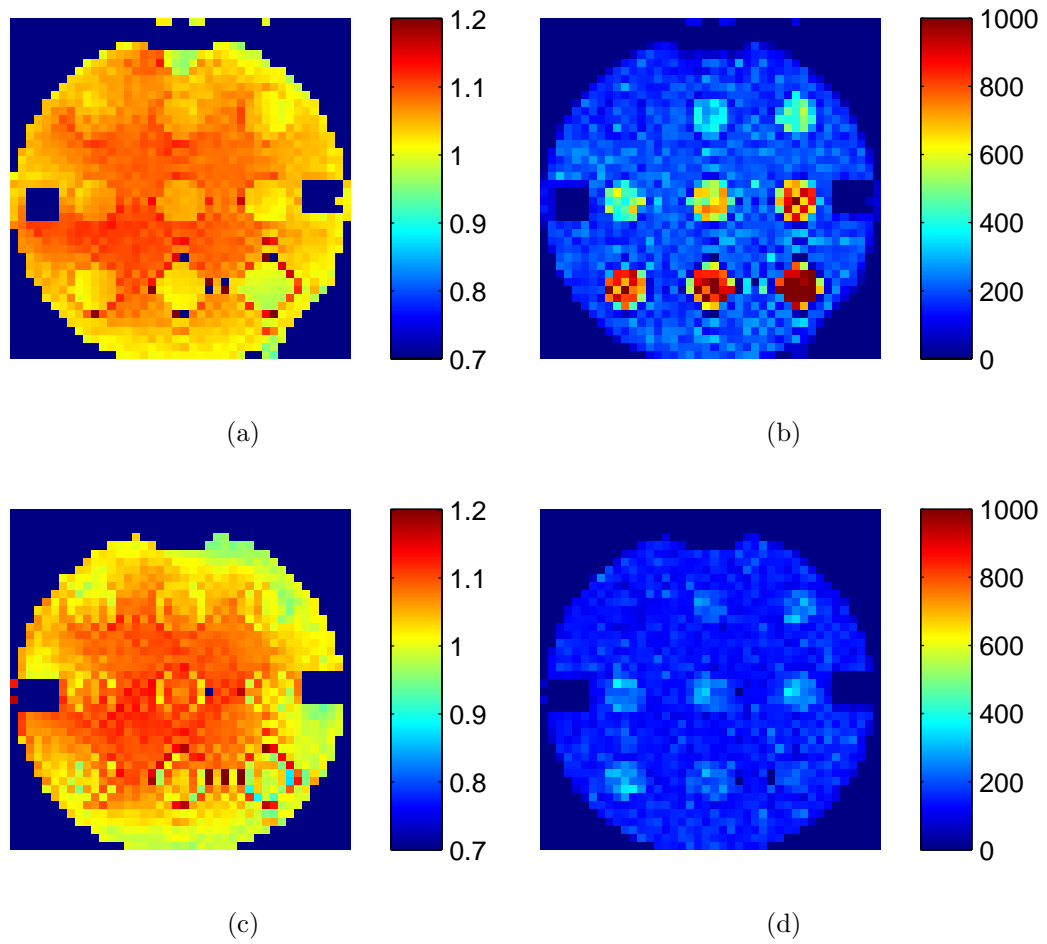


Figure 3.12: Noise properties of the AFI and niDALL techniques. (a) AFI flip angle map (α/α_{nom}) with $\alpha_{nom} = 120^\circ$, and $TR_1/TR_2 = 5/55$ ms (b) ANR map of (a). (c) niDALL flip angle with $\alpha_{nom} = 6^\circ$ and $\tau = 3.7ms$ and (d) the ANR map of the niDALL image.

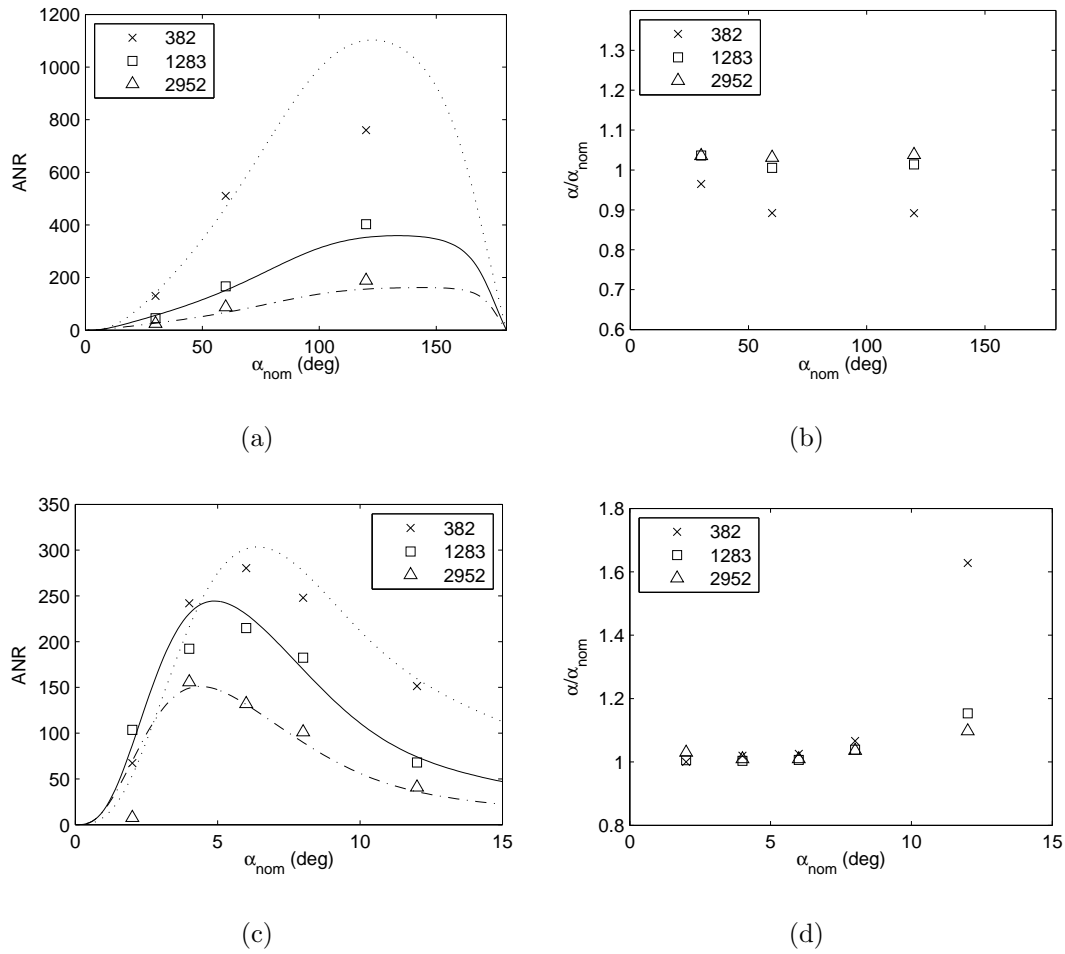


Figure 3.13: Performance of the AFI and non-inverted DALL techniques. (a) shows the ANR for a range of T_1 values in ms, and (b) shows the bias in the measurement. (c) is the ANR for the niDALL technique, and (d) is the bias in the niDALL flip angle measurement. Lines are the ANR predicted by propagation of noise.

around 116° . There are additional challenges at these higher flip angles, as the small tip angle assumption will no longer apply, and flip angle maps produced using slab selective pulses may not translate well to lower flip angles. In addition, spoiling becomes challenging, particularly when repetition times become shorter.

The results also indicate that the techniques are at their most efficient with relatively long repetition times ($T_{SR} = 1.25T_1$ for the satDAM method and $TR_1 + TR_2 = 1.3T_1$ for AFI). This indicates that better results are obtained by lengthening sequence parameters up to these limits rather than signal averaging. In addition, it appears that it may be advantageous to run the AFI technique with TR_1 minimized. Previous studies typically used the TR_2/TR_1 ratio in the range 4-6 which appears not to be ideal. At flip angles below 90° minimizing TR_1 leads to the best efficiency. At higher flip angles a TR_2/TR_1 closer to the previously suggested range may be optimum in terms of efficiency, but will lead to significant bias. For these reasons it is best to keep TR_1 to a minimum.

Using EPI imaging to permit a longer and more optimal T_{seq} for AFI and satDAM was shown to produce no net benefit in terms of imaging efficiency. EPI may have other benefits however. It could potentially make conventional DAM feasible. Using EPI also allows an increase in the sequence repetition times, which may have the additional benefit of reducing the difficulty in spoiling the transverse magnetization and reducing T_1 bias.

The Look-Locker based flip angle mapping techniques appear to have an efficiency that is relatively independent of T_{seq} . Overall, the niDALL was found to be the most efficient owing to the ability to fit a reduced parameter set. Thus, while it may not have the peak efficiency of the DAM or AFI methods, when scan times are limited, the ANR performance of the niDALL method may meet or exceed that of the other methods, especially for long T_1 values.

The propagation of noise analysis allows a conceptual approach to optimizing flip angle mapping techniques. It does, however, have some significant limitations.

The techniques presented assume perfect spoiling of the transverse magnetization at the end of each repetition period. At low flip angles and long repetition times, this may be a good assumption, and the primary source of error in the flip angle maps is likely to be noise propagated from the raw images. At the shorter repetition times and larger flip angles required by some of these techniques, the perfect spoiling assumption begins to break down.

3.6 Conclusion

The concept of flip angle imaging efficiency based on a theoretical propagation of noise analysis was successfully used to investigate the parameters that would give the best noise properties in flip angle maps. Imaging parameters for AFI, DAM and Look-Locker based imaging techniques were presented that optimized the flip angle techniques over a range of physical parameters, and experimental ANR ratios agreed with those predicted by the theoretical model. Overall the AFI approach appears to be an excellent choice when time constraints are not a factor, though it does suffer from spoiling difficulties and requires long imaging times for optimum performance. The Look-Locker based methods appear to be an excellent option, especially when short imaging times are required, or when small tip angles are desired.

3.7 Appendix

From least square propagation of noise statistics, we have [24]:

$$\sigma_{\alpha}^2 = \sum_i \left(\frac{\partial \alpha}{\partial S_i} \right)^2 \sigma_i^2 \quad (3.46)$$

Where S_i are the signal intensity values that enter into the calculation of the flip angle, and σ_i are the noise levels in each of those values. Since we expect the noise to be the same for each image, $\sigma_i = \sigma_0$. In addition, the signal values will in general

be given by $S_i = S_0 S'_i$. Thus Eq. 3.46 can be rewritten as:

$$\sigma_\alpha^2 = \left(\frac{\sigma_0}{S_0}\right)^2 \sum_i \left(\frac{\partial \alpha}{\partial S'_i}\right)^2 \quad (3.47)$$

and thus the dimensionless noise propagation factor is given by:

$$b^2 = \frac{1}{\alpha^2} \sum_i \left(\frac{\partial \alpha}{\partial S'_i}\right)^2 \quad (3.48)$$

3.7.1 DAM

For the double angle method, two signals, S'_1 and S'_2 , are required in Eq. 3.8, and thus Eq. 3.48 becomes:

$$b^2 = \frac{1}{\alpha^2} \left(\left(\frac{\partial \alpha}{\partial S'_1}\right)^2 + \left(\frac{\partial \alpha}{\partial S'_2}\right)^2 \right) \quad (3.49)$$

$$= \frac{1}{\alpha^2} \frac{1}{4S_1'^2 - S_2'^2} \left(\frac{S_1'^2 + S_2'^2}{S_1'^2} \right) \quad (3.50)$$

For the conventional DAM method, $S'_1 = \sin \alpha$ and $S'_2 = \sin 2\alpha$, while for the saturated DAM method $S'_1 = (1 - \exp(-T_{SR}/T_1)) \sin \alpha$ and $S'_2 = (1 - \exp(-T_{SR}/T_1)) \sin 2\alpha$.

Thus the error propagation term becomes:

$$b_{DAM}^2 = \frac{1}{\alpha^2} \frac{1}{4 \sin^2(\alpha) - \sin^2(2\alpha)} \left(\frac{\sin^2(\alpha) + \sin^2(2\alpha)}{\sin^2(\alpha)} \right) \quad (3.51)$$

$$b_{satDAM}^2 = b_{DAM}^2 \frac{1}{(1 - \exp(-T_{SR}/T_1))^2} \quad (3.52)$$

3.7.2 AFI

In the AFI method, the flip angle is determined by Eq. 3.17, and thus the noise propagation factor is given by:

$$b^2 = \frac{1}{\alpha^2} \left(\left(\frac{\partial \alpha}{\partial S'_1}\right)^2 + \left(\frac{\partial \alpha}{\partial S'_2}\right)^2 \right) \quad (3.53)$$

$$= \frac{1}{\alpha^2} \left(\frac{\partial \alpha}{\partial r}\right)^2 \left(\left(\frac{\partial r}{\partial S'_1}\right)^2 + \left(\frac{\partial r}{\partial S'_2}\right)^2 \right) \quad (3.54)$$

where $r = S_2/S_1 = S'_2/S'_1$ and with:

$$\frac{\partial \alpha}{\partial r} = -\frac{1}{n-r} \left(\frac{n^2-1}{1-r^2} \right)^{1/2} \quad (3.55)$$

b becomes:

$$b^2 = \frac{1}{S_1'^2 \alpha^2} \frac{(n^2-1)(r^2+1)}{(1-r^2)(n-r)^2} \quad (3.56)$$

$$= \frac{1}{\alpha^2 \sin^2 \alpha} \left(\frac{1 - E_1 E_2 \cos^2 \alpha}{1 - E_2 + (1 - E_1) E_2 \cos \alpha} \right)^2 \frac{(n^2-1)(r^2+1)}{(1-r^2)(n-r)^2} \quad (3.57)$$

by substituting $S'_1 = S_1/S_0$ as given by Eq. 3.15

3.7.3 DALL

For the double angle method, the flip angle is given by 3.20, and thus Eq. 3.46 can be reduced to:

$$\sigma_\alpha^2 = \left(\frac{\partial \alpha}{\partial E_\Delta} \right)^2 \left(\left(\frac{\partial E_\Delta}{\partial T_{1,1\alpha}^*} \right)^2 \sigma_{T_{1,1\alpha}^*}^2 + \left(\frac{\partial E_\Delta}{\partial T_{1,2\alpha}^*} \right)^2 \sigma_{T_{1,2\alpha}^*}^2 \right) \quad (3.58)$$

where:

$$\frac{\partial E_\Delta}{\partial T_{1,1\alpha}^*} = -\frac{E_\Delta \tau}{T_{1,1\alpha}^{*2}} \quad (3.59)$$

$$\frac{\partial E_\Delta}{\partial T_{1,2\alpha}^*} = \frac{E_\Delta \tau}{T_{1,2\alpha}^{*2}} \quad (3.60)$$

and $\sigma_{T_{1,1\alpha}^*}$ and $\sigma_{T_{1,2\alpha}^*}$ can be found by analyzing the propagation of noise in least squares fitting.

Statistical analysis of least squares fitting [24] yields the error matrix, $\epsilon = \beta^{-1}$, where the elements of β are given by:

$$\beta_{jk} = \sum_i \left[\frac{1}{\sigma_i^2} \frac{\partial y(x_i)}{\partial a_j} \frac{\partial y(x_i)}{\partial a_k} \right] \quad (3.61)$$

where y is the function that is fit, x_i are the locations of the data points used in the fitting, σ_i is the noise in the data point at x_i and a are the parameters in the function.

For Look-Locker imaging $y(x_i) = S(t_i) = A + (B - A) \exp(-t_i/T_1^*)$, and if we set $a_1 = T_1^*$, $a_2 = A$ and $a_3 = B$, then $\sigma_{T_1^*}^2 = \epsilon_{1,1}$. An exact solution can be found in [17], and is summarized by the T_1^* error propagation term:

$$b^* = \left(\frac{c_{02}c_{00} - c_{01}^2}{c_{22}c_{02}c_{00} + 2c_{12}c_{01}c_{11} - c_{12}^2c_{00} - c_{01}^2c_{22} - c_{11}^2c_{02}} \right)^{1/2} \quad (3.62)$$

$$c_{m,n} = \sum_{i=1}^N (t_i/T_1^*)^m \exp(-nt_i/T_1^*) \quad m, n = 0, 1, \text{ or } 2$$

and thus the α noise amplification factor becomes:

$$b^2 = \frac{1}{\alpha^2} \left(\frac{\partial \alpha}{\partial E_\Delta} \right)^2 \left(\left(\frac{E_\Delta \tau b_{1\alpha}^*}{T_{1,1\alpha}^* DR_1} \right)^2 + \left(\frac{E_\Delta \tau b_{2\alpha}^*}{T_{1,2\alpha}^* DR_2} \right)^2 \right) \quad (3.63)$$

For the non-inverted DALL method, it is possible to fit S_1 and S_2 simultaneously for α , T_1 and M_0 . Thus Equation A.83 becomes:

$$\beta_{jk} = \frac{1}{\sigma_0^2} \sum_i \left[\frac{\partial S_{1\alpha}(t_i)}{\partial a_j} \frac{\partial S_{1\alpha}(t_i)}{\partial a_k} + \frac{\partial S_{2\alpha}(t_i)}{\partial a_j} \frac{\partial S_{2\alpha}(t_i)}{\partial a_k} \right] \quad (3.64)$$

Where $a_1 = \alpha$, $a_2 = T_1$ and $a_3 = M_0$. $S_{1\alpha}$ and $S_{2\alpha}$ can be reduced to functions of α , T_1 , and M_0 by substituting the full terms for A , B and T_1^* into equation 3.28. The solution is complex and was solved using the symbolic math toolbox in Matlab.

References

- [1] de Moortele PFV, Akgun C, Adriany G, Moeller S, Ritter J, Collins CM, Smith MB, Vaughan JT, and Ugurbil K. B_1 destructive interferences and spatial phase patterns at 7 T with a head transceiver array coil. *Magn Reson Med* 2005; 54:1503–1518.
- [2] Pauly J, Nishimura D, and Macovski A. A k-space analysis of small-tip-angle excitation. *J Magn Reson* 1989;81:43–56.
- [3] Oh C, Hilal S, Cho Z, and Mun I. Radio frequency field intensity mapping using a composite spin-echo sequence. *Magn Reson Imaging* 1990;8:21–25.
- [4] Morrell GR. A phase-sensitive method of flip angle mapping. *Magn Reson Med* 2008;60:889–894.
- [5] Sacolick LI, Wiesinger F, Hancu I, and Vogel MW. B_1 mapping by Bloch-Siegert shift. *Magn Reson Med* 2010;63:1315–1322.
- [6] Hornak JP, Szumowski J, and Bryant RG. Magnetic field mapping. *Magn Reson Med* 1988;6:158–163.
- [7] Insko E and Bolinger L. Mapping of the radiofrequency field. *J Magn Reson A* 1993;103:82–85.
- [8] Stollberger R and Wach P. Imaging of the active B_1 , field in vivo. *Magn Reson Med* 1996;35:246–251.
- [9] Cunningham CH, Pauly JM, and Nayak KS. Saturated double-angle method for rapid B_1+ mapping. *Magn Reson Med* 2006;55:1326–1333.
- [10] Dowell NG and Tofts PS. Fast, accurate, and precise mapping of the RF field in vivo using the 180° signal null. *Magn Reson Med* 2007;58:622–630.

- [11] Pan JW, Twieg DB, and Hetherington HP. Quantitative spectroscopic imaging of the human brain. *Magn Reson Med* 1998;40:363–369.
- [12] Yarnykh VL. Actual flip-angle imaging in the pulsed steady state: A method for rapid three-dimensional mapping of the transmitted radiofrequency field. *Magn Reson Med* 2007;57:192–200.
- [13] Wade T and Rutt B. B1 correction using double angle Look-Locker (DALL). In: *Proceedings of the 16th Annual Meeting of the International Society of Magnetic Resonance in Medicine, Toronto, Canada 2008*;:1246.
- [14] Hsu JJ, Zaharchuk G, and Glover GH. Rapid methods for concurrent measurement of the RF-pulse flip angle and the longitudinal relaxation time. *Magn Reson Med* 2009;61:1319–1325.
- [15] Look D and Locker D. Time saving in measurement of NMR and EPR relaxation times. *Rev Sci Instrum* 1970;41:250–251.
- [16] Henderson E, Mckinnon G, Lee TY, and Rutt BK. A fast 3D Look-Locker method for volumetric T_1 mapping. *Magn Reson Imaging* 1999;17:1163–1171.
- [17] Crawley AP and Henkelman RM. A comparison of one-shot and recovery methods in T_1 imaging. *Magn Reson Med* 1988;7:23–43.
- [18] Wade T and Rutt B. B1 correction using dual tau Look-Locker (D τ LL). In: *Proceedings of the 17th Annual Meeting of the International Society of Magnetic Resonance in Medicine, Honolulu, USA 2009*;:572.
- [19] Crawley AP, Wood ML, and Henkelman RM. Elimination of transverse coherences in FLASH MRI. *Magn Reson Med* 1988;8:248–260.
- [20] Saekho S, Boada FE, Noll DC, and Stenger VA. Small tip angle three-dimensional tailored radiofrequency slab-select pulse for reduced B_1 inhomogeneity at 3 T. *Magn Reson Med* 2005;53:479–484.

- [21] Katscher U, Börnert P, Leussler C, and van den Brink JS. Transmit SENSE. *Magn Reson Med* 2003;49:144–150.
- [22] Ullmann P, Junge S, Wick M, Seifert F, Ruhm W, and Hennig J. Experimental analysis of parallel excitation using dedicated coil setups and simultaneous RF transmission on multiple channels. *Magn Reson Med* 2005;54:994–1001.
- [23] Nehrke K. On the steady-state properties of actual flip angle imaging (AFI). *Magn Reson Med* 2009;61:84–92.
- [24] Bevington PR and Robinson DK. *Data Reduction and Error Analysis for the Physical Sciences*. McGraw-Hill, New York, 2003.

Chapter 4

Spoiling for Accelerated 3D

Look-Locker Acquisitions

Abstract

The Look-Locker technique is a fast and efficient method of measuring the longitudinal recovery constant, T_1 . This makes it adaptable to imaging, and in particular it can be used in an accelerated 3D Look-Locker acquisition to rapidly acquire T_1 , or flip angles. When flip angles become large, or repetition times become short relative to T_1 and T_2 , conventional techniques fail to effectively spoil the transverse magnetization, leading to significant deviations from an ideal transient and inaccuracies in the measurement of the modified recovery constant, T_1^* . A novel approach using a randomized spoiling scheme was recently suggested for steady-state imaging applications where signal accuracy is more important than artefacts induced by not being in a true steady-state. Here this approach is applied to transients measured using the accelerated 3D Look-Locker technique. This improved random spoiling is particularly well suited to this application as conventional spoiling causes erratic deviations from the ideal transient, and these can be significantly reduced using random spoiling. This approach is shown to improve the accuracy of measurements of T_1^* without degrading image quality.

4.1 Introduction

Fast imaging in the steady-state using short repetition times and spoiling of the transverse magnetization is an efficient method of image acquisition. The short repetition times make fast imaging possible, and by acquiring data using the Ernst angle, the acquisition can be very efficient. By spoiling the transverse magnetization before each radio-frequency (RF) pulse, the image contrast can be defined by a relatively simple equation, simplifying image interpretation and making quantitative imaging feasible.

Conventionally, spoiling is achieved by using a quadratically increasing RF phase combined with a constant amplitude gradient crusher [1]. So long as the crusher dephases spins in a voxel by a multiple of 2π , this will lead to the formation of a steady-state. An appropriate choice of the quadratic increase in phase will lead to a steady-state signal that approaches the ideally spoiled case for a range of relaxation times and imaging parameters. The precise choice of quadratic increase will, however, depend on the particular application [1–6].

The motivation behind this deterministic spoiling scheme is that it will lead to a steady-state. The signal will thus be modulated only by the phase and frequency encoding gradients leading to a nearly ideal point spread function (PSF). If a random spoiling gradient [1] or random RF phase spoiling [7] scheme were used, there would be underlying variation of the magnetization from α pulse to α pulse. This would lead to a non-ideal PSF, and artefacts similar to motion or ghosting artefacts.

As repetition times become short, excitation angles become large, and relaxation times lengthen, the cancellation of coherence pathways induced by the quadratically increasing RF phase, begins to break down and the steady-state magnetization achieved by the quadratic scheme begins to deviate significantly from the ideal value. This particularly becomes a concern where the steady-state signal is used for quantitative T_1 analysis as in DESPOT1 [8], or flip angle mapping using AFI [9]. While

a steady-state will be reached, it can no longer be described by a simple expression, leading to inaccuracies in the analysis.

In cases where the accuracy of the signal amplitude is essential, it may be advantageous to resort to a random spoiling scheme [10]. By using random spoiling phase and random amplitude crusher gradients, the signal will oscillate about the ideally spoiled value. If conventional Cartesian imaging were employed, this would lead to the ghosting artefacts suggested above. This can be overcome by using radial sampling, which effectively averages the centre of k-space, reducing the artefacts to an acceptable level.

When not in steady-state, the prime reason for using quadratic spoiling disappears. In Look-Locker imaging [11, 12] or accelerated 3D Look-Locker acquisitions [13], we are interested primarily in the transient before steady-state is reached. Even in a perfectly spoiled situation, sampling along the transient in the accelerated 3D Look-Locker case would lead to modulation of k-space. In addition, quadratic spoiling does not lead to a situation in which signal follows an exponential. Instead, the signal deviates erratically from the ideally spoiled curve, and leads to additional degradation of image quality and inaccuracy when fitting a time constant to the measured transient.

The Look-Locker sequence was conceived as a method to quickly measure T_1 and consists of an inversion pulse followed by a low flip angle excitation pulse train to sample the recovery curve. This was incorporated into a 2D imaging sequence [12] which formed one image for each low angle RF pulse in the readout train, and required multiple repetitions to fully sample k-space. The accelerated 3D Look-Locker sequence [13] is a modification of the original which uses slice and phase encode gradients to partition the recovery curve into a 3D data set with multiple effective inversion time (TI) volumes. In this case, the deviations from the ideally spoiled transient, due to imperfect spoiling, lead to effective TI images with signal that deviates significantly from the ideal. This leads to inaccuracy in T_1 images

obtained from this technique.

While originally designed for T_1 imaging, the Look-Locker imaging sequence can also be used to rapidly quantify the flip angle [14,15]. This, however, requires shorter repetition times and larger flip angles, which both contribute to poorer spoiling effectiveness.

Quadratic spoiling does not produce a signal that varies smoothly from sample to sample in the transient case, or even a curve that follows the ideally spoiled case. We hypothesize that a random spoiling scheme, like that proposed by Lin [10], may lead to images that better approximate the decay curve with reduced artefact. In this chapter, the effects of random and quadratic spoiling on the transients used in accelerated 3D Look-Locker imaging, and the resulting accuracy of T_1^* and flip angle maps is investigated. The influence of spoiling on the resulting point spread functions is also investigated.

4.2 Theory

The Look-Locker technique uses an inversion pulse followed by a long train of low flip angle pulses to sample the relaxing longitudinal magnetization (IR-SPGR) as indicated in Figure 1.8. This provides a very fast and efficient technique for measuring T_1 [16]. SPGR pulses not only sample the recovering magnetization, but also perturb it, leading to a modified longitudinal recovery constant:

$$\frac{1}{T_1^*} = \frac{1}{T_1} - \frac{\ln(\cos \alpha)}{\tau} \quad (4.1)$$

where α is the angle of the rapid sampling pulses, and τ is the spacing between those pulses. If the flip angle is known, then the true T_1 can be deduced from the measured T_1^* .

The analysis of the above is further complicated by the sampling scheme employed in the accelerated 3D Look-Locker acquisition. Each effective TI image is formed

using a small subset of samples along the transient, and multiple inversion- α -train repetitions are required to fully sample k-space. For example, if 128 samples are acquired and segmented into 8 effective TI images, 16 phase encode lines for each effective TI image can be acquired for each repetition of the inversion- α -train. The inversion- α -train would then have to be repeated until all phase encodes are acquired, and the effective inversion time for each image would then be determined by the time after inversion at which the centre of k-space is acquired.

Filling k-space by sampling along the transient in this way, introduces an additional modulation of k-space that depends on the order in which phase encode lines are acquired and is best quantified by observing the distortion of the point spread function [17]. In addition to the distortion introduced by the transient, the deviation from ideal transient induces an additional distortion. In simulation, it is possible to separate these two effects.

Quadratic RF spoiling uses an ever increasing phase angle of each subsequent RF pulse to spoil the transverse magnetization.

$$\phi_n = \phi_{n-1} + n\phi_{seed} \quad (4.2)$$

The optimum ϕ_{seed} value has been found by numerical simulation to be 117° for steady-state [1], and for transient signals to be 84° [4] to best match the ideally spoiled case for a range of relaxation times and sequence parameters. For other applications, other values may be better suited. For example, for T_1 mapping using the variable flip angle technique a value is 50° is proposed [5] based on stability concerns and T_1 measurement accuracy. For the actual flip angle technique [9], which involves an interleaved TR steady-state, a different value again (129°) is required [3]. In addition to the phase spoiling, another approach is to include very large spoiling gradient moments to induce additional spoiling due to diffusion losses [18].

While quadratic spoiling produces good qualitative images with minimal artefact, when repetition times become short in comparison to relaxation times and/or flip

angles become large, it becomes progressively more difficult to achieve the cancellation of coherence pathways. At this point, the signal begins to deviate significantly from the ideally spoiled value, and it becomes impossible to choose a ϕ_{seed} value that is applicable to a reasonable range of imaging parameters. This causes problems in applications where signal accuracy is essential. This has led to a renewed interest in randomized spoiling techniques [10].

The spoiling scheme proposed randomizes the phase of each RF pulse. Specifically, each RF pulse has a phase randomly chosen from the interval $[-\pi, \pi]$. In addition, each repetition will also include a crusher gradient of random amplitude that dephases spins over a given voxel, by value C measured in cycles/voxel, where C is randomly chosen from the interval $[C_{min}, C_{max}]$.

4.3 Materials and Methods

4.3.1 Simulation

The approach to steady-state was modelled using Bloch simulations implemented in Matlab. For simplicity all of the pulses were assumed to be perfect hard pulses. The signal after each pulse was simulated by summing 10000 isochromats uniformly distributed along the gradient spoiling direction.

For spoiling in the steady-state, a gradient randomized over the interval [10,20] cycles/voxel was previously found to be optimum [10]. For a transient, the same may not be the case. To investigate this, two gradient randomization schemes were simulated and compared to the ideally spoiled transient based on the root mean square error (RMSE) between the simulated transient and an ideally spoiled transient. The random spoiling schemes investigated included random crusher ranges $[-C_{max}, C_{max}]$, and $[0.5C_{max}, C_{max}]$. The transient investigated was modeled assuming a sample with $T_1 = 2000$ ms, $T_2 = 200$ ms, and $64, 30^\circ \alpha$ pulses separated by $\tau = 3.5$ ms. This

would imply a T_1^* value of 24 ms, and sampling fairly far out on the exponential curve (out to approximately $9 T_1^*$).

4.3.2 Experimental

The accelerated 3D Look-Locker sequence was implemented on a 3T GE Discovery MR750 scanner. A pseudo random number generator [19] was used to perform the randomization of RF phase and spoiling gradients, and the slab select (Z) gradient was used for the spoiling gradient. Each effective TI image was formed from a group of α pulses along the α -train, and within each group, ky-kz space was sampled using a 2D centric encoding scheme. In other words, within each TI interval, the first RF pulse was used to encode the lines closest to the centre of k-space, thus giving an effective TI given by the time of the first α pulse within each TI interval.

A small CuSO_4 phantom ($T_1 = 143$ ms, $T_2 = 117$ ms) was used to minimize any B_1^+ inhomogeneity artefact and to simplify validation of the the simulations. The inversion recovery curve was sampled with 512, 30° RF pulses with $\tau = 3.6$ ms, spoiled using either the quadratic or random methods. This long train of RF pulses allowed investigation of both the transient phase of the signal, as well as the steady-state. Imaging gradients were turned off to give a direct measurement of signal after each pulse, that could be compared to a simulated transient. A delay of two seconds was used between the end of one transient and the next inversion to allow for full relaxation, and to facilitate comparison with simulation and imaging.

The imaging gradients were turned back on, and the number of RF pulses reduced to 64 to acquire eight effective inversion time images of the phantom during the transient phase. Within each effective TI image, the ky-kz lines were encoded using a 2D centric approach [20]. The first pulse within each group was used to encode the line closest to the centre of k-space, and the last the line furthest out in k-space. The sequence was then repeated to fully sample k-space with a 2 s delay between the end of each sampling train and the next inversion for full recovery. Other imaging

parameters were the same as for the acquisition of the transient above. The signal intensities of a central region of interest were measured for each effective TI image and were compared to the raw transient acquired with imaging gradients turned off.

4.3.3 Theoretical PSF

The accelerated 3D Look-Locker acquisition is complicated by the fact that signal is modulated by sampling along the transient. This in itself leads to modulation of k-space [17], and a non-ideal PSF. This much is inevitable in the accelerated 3D Look-Locker acquisition. In addition to this effect, however, is any deviation from the ideal transient.

The cumulative effect of these deviations is shown in Figure 4.1. The Fourier transform of a delta function leads to a constant in k-space. In an ideal situation, the signal acquired from this point source for each effective TI image would be a constant in k-space ($S(k_y, k_z) = S(k = 0)$). This ideal k-space is then modulated by the sampling scheme along the transient, $S_{trans}(k_y, k_z)/S(k = 0)$. The Fourier transform of this function gives the PSF due to the transient itself (PSF_{trans}). Next, the k-space is further distorted by the deviations from the ideal curve due to imperfect spoiling, contributing to the distorted k-space image. The Fourier transform of this second distortion produces the PSF due to imperfections in spoiling (PSF_{spoil}). The convolution of these two point spread functions combine to produce the distortion in the final image and potential inaccuracies in the signal intensity as measured using an accelerated 3D Look-Locker acquisition.

The blurring due to sampling along the transient (PSF_{trans}) is inevitable due to the definition of the accelerated 3D Look-Locker sequence. PSF_{spoil} on the other hand is something we can try to control by our choice of spoiling scheme. First, we want to control any additional blurring, or ghosting. Secondly, the area under PSF_{spoil} , which is also given by the deviation of $M_{spoil}(k = 0)$ from the ideal, will lead to an inaccurate intensity of the effective TI image, and thus a potential bias in

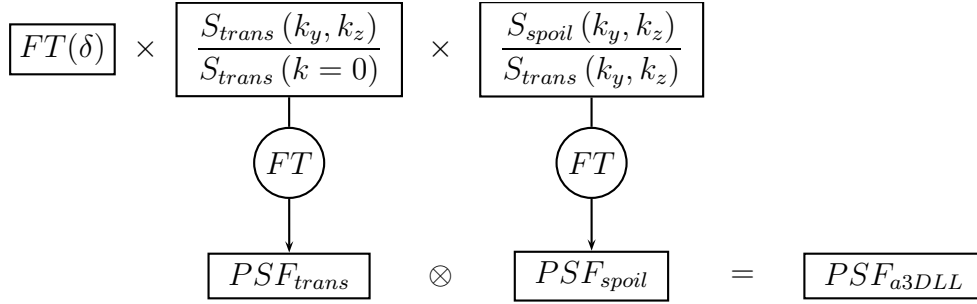


Figure 4.1: The steps used to determine sources of artefact in simulated accelerated 3D Look-Locker acquisitions. A point is represented by a constant in k-space. This is modulated by sampling along the transient, and any fluctuations from the transient caused by imperfect spoiling, resulting in the distorted image of the point.

the T_1^* measurement.

The 2D centric sampling scheme will lead to a circularly symmetric modulation of k-space. Thus a 1D profile through the 2D PSF should be sufficient to characterize it.

4.3.4 Quantitative Imaging

A 12 cm diameter saline filled cylinder with 9 samples doped with NiCl to T_1 's ranging from 185 ms to 2953 ms was imaged using the accelerated 3D Look-Locker sequence. Transients were sampled with 48 α pulses with a repetition time of 3.6 ms. These pulses were segmented into 8 effective TI volumes. The transients were sampled with either 15° or 30° RF pulses in an interleaved sense:

$$[\pi - \{48, 15^\circ \text{ RF pulses}\} - \pi - \{48, 30^\circ \text{ RF pulses}\}]_{repeat}$$

This permitted imaging of the T_1^* values at two different flip angles and also allowed the technique to be used to derive a flip angle map using the double angle Look-Locker approach. Imaging was based on a 3D matrix, 42x42 in plane (FOV = 12 cm) with 24, 10 mm thick slices to cover the entire phantom. Spoiling was either conventional

quadratic spoiling, using $\phi_{seed} = 84^\circ$ and a crusher producing 14 cycles/voxel, or randomized phase and gradients over the interval [10 20] cycles/voxel.

The T_1^* values derived from the accelerated 3D Look-Locker technique were then compared to values derived from a 2D inversion prepared fast spin echo measurement of T_1 and a flip angle measured using the AFI technique [9]. Accelerated 3D Look-Locker acquisitions were repeated 20 times to assess the accuracy and precision of the T_1^* and α measurements, as well as to investigate the benefits of averaging.

4.4 Results

4.4.1 Optimal Spoiler Gradient

The result of choosing different gradient crushers is shown in Figure 4.2. The quadratic spoiling scheme is shown as a baseline, and its performance does not change with increasing crusher strength, over the minimum required of one cycle/voxel. Similarly, if a randomized phase is used in conjunction with a non-randomized gradient crusher, there is no improvement with moving to increasing gradient crusher amplitude. This can be summarized as follows [10]. The isochromat signal across the crusher direction of the voxel is periodic with position. Thus, if the gradient crusher produces a phase dispersion of 2π , or 10π , the voxel signal will be the same as there will be 1 period or 10 periods of magnetization and thus yield the same signal. Randomizing the crusher amplitude breaks this periodicity.

With random crusher moments, isochromat signal will no longer be a periodic function of position along the gradient crusher direction. Instead, the random gradients add a spatially dependent nature to the random isochromat signal. If the crusher moments are small ($C_{max} < 5\text{cycles/pixel}$), then there will be less spatial variation in the isochromat signal and coherence pathways can still be conserved. As the crusher moments become larger, there will be greater variation within a voxel,

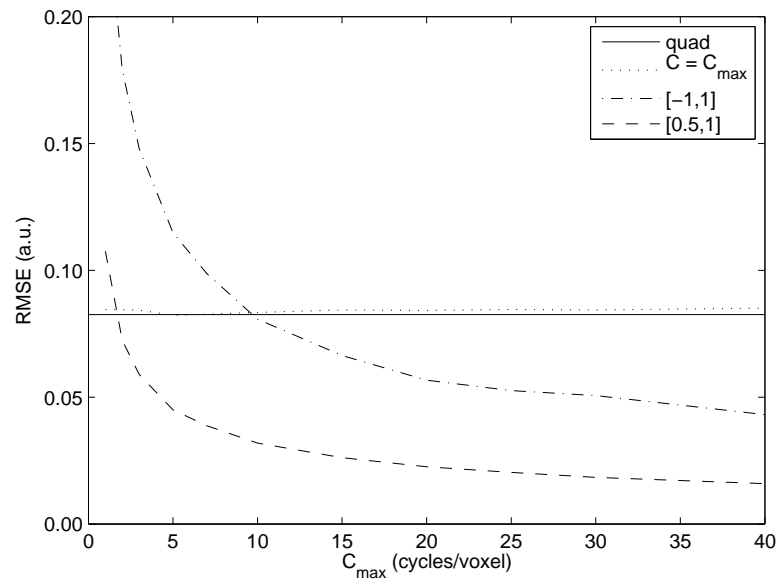


Figure 4.2: Root mean square error between ideally spoiled and simulated transient. Shown are the conventional quadratic spoiling, random phase with fixed crusher, and random phase with crushers randomized over different intervals. 64 samples post inversion, $\tau = 3.5$ ms, $T_1/T_2 = 2000/200$ ms. Ranges shown are a fraction of C_{max} .

and the coherence pathways will generally cancel. This is evident in Figure 4.2, where larger maximum random gradient moments lead to better agreement with the ideally spoiled curve. For steady-state, uniformly distributed random crushers over the range $[0.5, 1]C_{max}$ were reported to be optimum [10] by avoiding low gradient moments or balanced gradients that could lead to rephasing while still allowing a significantly large random range. The same appears to be true for spoiling of transient curves. A value of $C_{max} = 20$ cycles/voxel was previously reported to be optimum. While there appears to be little benefit of randomized crushers greater than this value, results significantly better than quadratic spoiling should be possible with C_{max} as low as 5 cycles/voxel.

4.4.2 Validation

The approach to steady-state is not smooth even when a quadratic spoiling scheme is used, as shown Figure 4.3(a). Despite the deterministic spoiling scheme, the signal varies erratically about the ideally spoiled curve. There are segments where the signal deviates consistently from the exponential for several samples. A random spoiling scheme removes these systemic deviations in favour of more random oscillations. In addition, the amplitude of the deviations is smaller leading to an overall better approximation of the ideally spoiled exponential.

The motivation for quadratic spoiling is evident from the right end of the plot of Figure 4.3(a). After a sufficient number of pulses, the magnetization enters a true steady-state but with a significant deviation from the fully spoiled value. The approach to steady-state, however, is erratic, with significant deviations from the ideally spoiled transient. It is this erratic transient that makes fitting an exponential to acquire an estimate of T_1^* unreliable. The deviations are not due to noise. Rather they are repeatable, and due to the erratic combination of coherence pathways. This is demonstrated by the experimentally measured points that track the simulated spoiling.

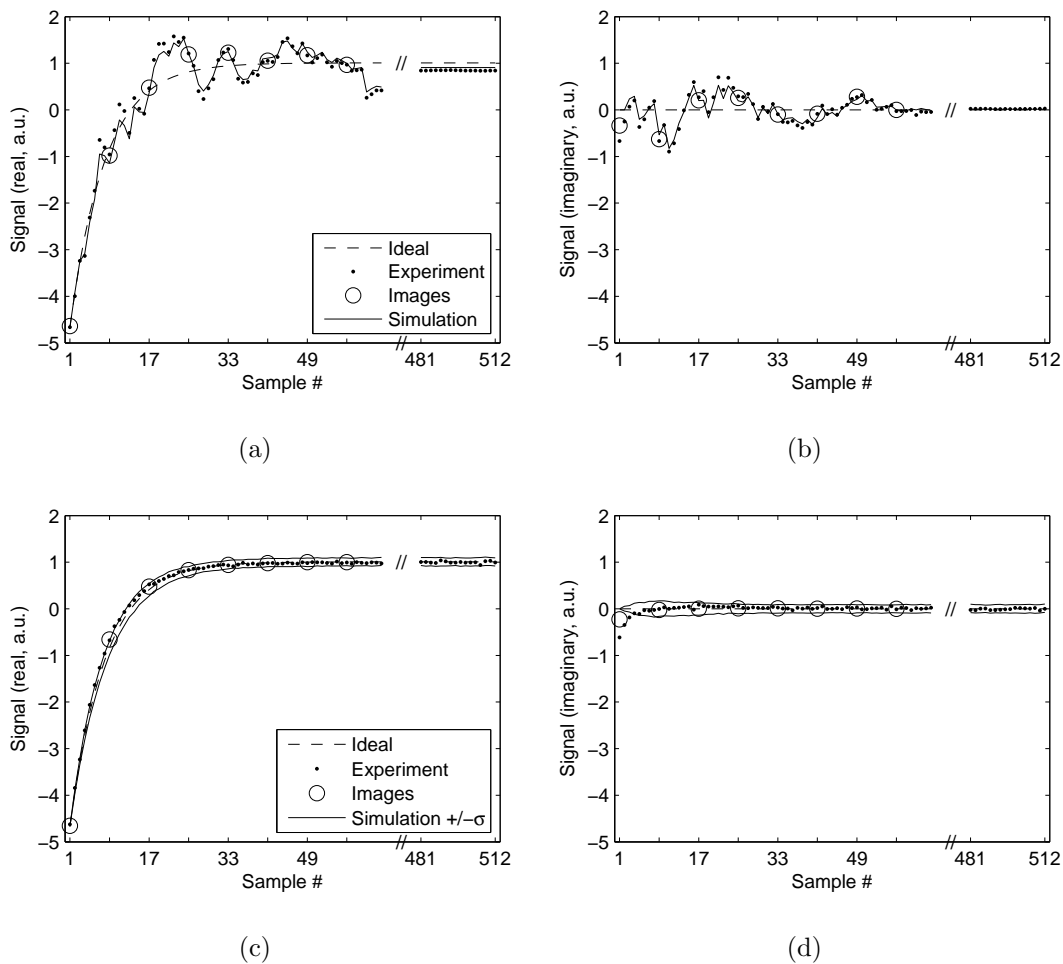


Figure 4.3: Bloch simulations and experimental data for approach to steady-state employing quadratic or random spoiling schemes. (a and b) Real and imaginary components respectively of the signal for a transient acquired using quadratic spoiling and a small amplitude crusher (2 cycles/voxel) and a $\phi_{seed} = 84^\circ$. (c and d) Real and imaginary signal for a transient acquired using random phase and crusher gradients randomized over interval [10,20] cycles/voxel. The standard deviation in the transient points is 0.0042 for quadratic spoiling and 0.021 for the random spoiling.

The points that encode the center of k-space determine the signal intensity values of the effective TI images. With the imaging gradients turned on, images were acquired of the uniform phantom, and a central ROI used to measure the signal of the effective TI images. These values are indicated by the circles, which indicate that the image intensity is effectively determined by the points encoding the centre of k-space. It is these image values that determine the T_1^* map of accelerated 3D Look-Locker acquisitions, and the deviations from ideal transient cause inaccuracies in the T_1^* measurement.

When using random spoiling, as in Figure 4.3(c), even well after the transient phase has ended, the signal still varies slightly from sample to sample, but it does so about the fully spoiled value. In the approach to steady-state, however, the random fluctuations are beneficial, as they remove the large, erratic deviations from the ideally spoiled transient. Instead the points are randomly distributed about the transient, well within the deviations predicted by simulation. Since the deviations are smaller and random, exponential fitting to the transient is likely to produce a more reliable estimate of T_1^* . This results in a lower RMSE for the first 64 samples along the recovery as indicated in Table 4.1.

The noise and error differences between the spoiling approaches are shown in Figure 4.4(a). For a single point along the transient (sample 23 in Figure 4.3), a histogram of the error, as given by the difference between the experimental data and theoretically ideal transient, was found using multiple repeats of each transient. Each repetition of the quadratically spoiled transient will consistently give a point that deviates from the ideal, as can be seen by the narrow spread in error values, at a significant bias. Random spoiling leads to a point that on average will be the correct value, but introduces additional noise into the measurement. This is demonstrated by the broader histogram, that is centred about the ideal value.

Diffusion also has an effect on the spoiling, and can even be used as the primary source of transverse magnetization damping [2, 3]. To investigate this property, the

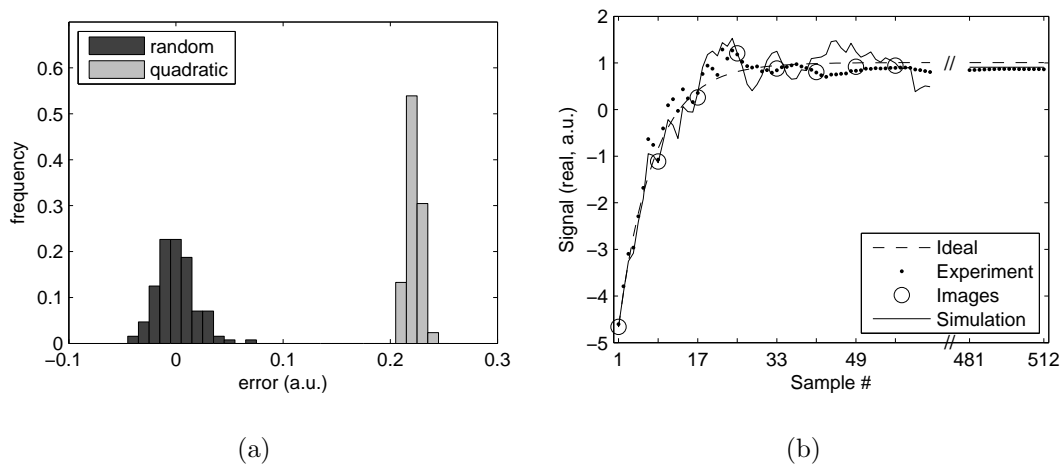


Figure 4.4: Noise and diffusion effects on spoiling. (a) error properties of random and quadratic spoiling for sample 23. (b) Effect of increasing the crusher amplitude to 15 cycles/voxel in the quadratic spoiling case.

amplitude of the crusher gradient for the quadratic spoiling was increased to 15 cycles per voxel to match the average value of the random spoiler gradient. As can be seen in Figure 4.4(b), this leads to additional damping of the erratic fluctuations in the quadratically spoiled transient, leading to a reduction in the error between experimental and theoretical perfect spoiling as indicated in Table 4.1. This indicates that diffusion does have an effect on, and can improve spoiling. The improvement, however, is not sufficient to match the spoiling when both random phase and random gradients are used.

RF phase	Gradient cycles/voxel	RMSE
quadratic	2 (constant)	0.40
quadratic	15 (constant)	0.23
random	[10,20] (range)	0.07

Table 4.1: Error between experimental samples and theoretically ideally spoiled samples for quadratically spoiled and randomly spoiled transients. Only the first 64 samples were used to highlight the errors during the transient phase.

4.4.3 PSF

The effect of imperfect spoiling can be seen in the effective TI images of the CuSO_4 phantom shown in Figure 4.5. In these, the first effective TI volume images are dominated by the transient phase producing some minimal blurring. Due to the fully relaxed state prior to the inversion, no spoiling related artefacts are apparent. By the third effective TI image, differences in the techniques begin to appear. Both quadratic and random spoiling schemes produce a minimal amount of ghosting in the phase encoding directions (read direction is vertical) due to the imperfect PSF. Also apparent is the overestimation of the signal intensity in the quadratically spoiled image. This image is significantly brighter than the randomly spoiled image, and even contains regions that are brighter than the last effective TI image. Since this effective TI volume is acquired during the transient phase, this should not be so.

In the last effective TI image, the ghosting is still barely evident in the randomly spoiled image, and less so when quadratically spoiled. The image intensity of the quadratically spoiled image, however, slightly underestimates the signal when compared to the randomly spoiled image. In both the quadratically and randomly spoiled imaging, some Gibbs ringing is evident, but any differences between the top row and bottom row are due entirely to the choice of spoiling.

The process described in Figure 4.1 is shown using simulated data in Figure 4.6. Using the given acquisition scheme (64 α pulses segmented into 8 effective TI times), the ky-kz lines are acquired using a centric approach. The perfect image of a point in k-space would be uniform, with an intensity given by the effective TI time as in Figure 4.6(a). Using the accelerated 3D Look-Locker sequence, this is not feasible. For the first effective TI image, the first 8 RF samples are used to populate ky-kz lines, and even with perfect spoiling, the transient would lead to signal variations from sample to sample. This leads to the 8 concentric regions in Figure 4.6(b), one for each of the RF pulses in the first effective TI image. The centre of k-space is populated by the first RF pulse, the next ring by the second RF pulse, and so on. Subsequent effective

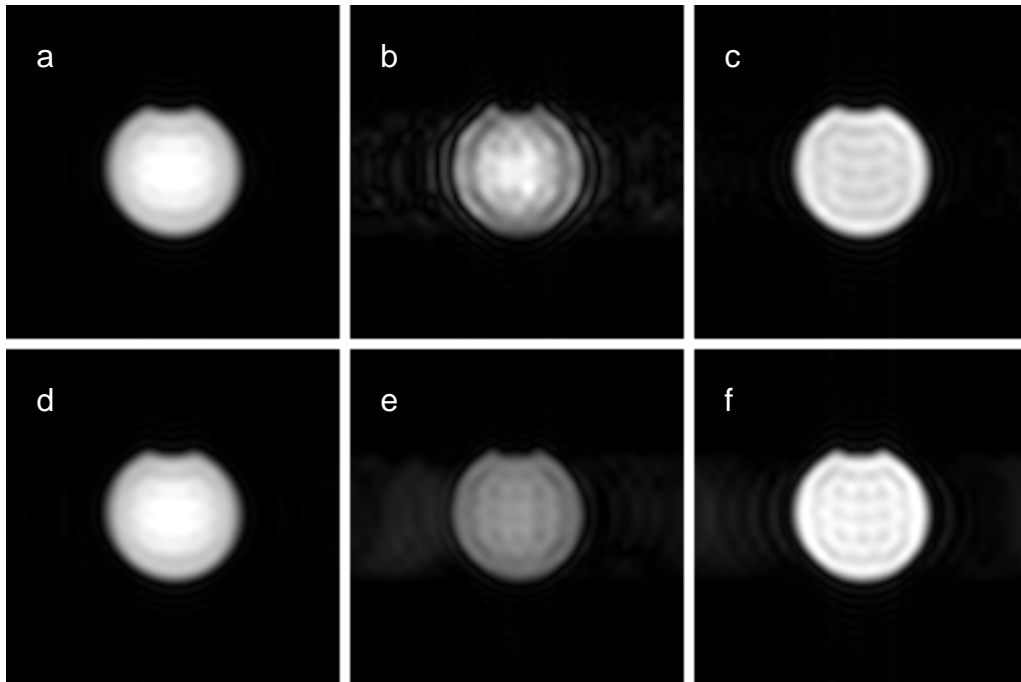


Figure 4.5: Effective TI magnitude images of the CuSO_4 phantom. Top row (a,b,c) are images using quadratic sampling for the first, third and eighth effective TI image respectively. Bottom row (d,e,f) are images based on random spoiling for the same effective TI values as the above quadratically spoiled images. The first TI images are scaled by 1/6th but the third and eighth have same window and level.

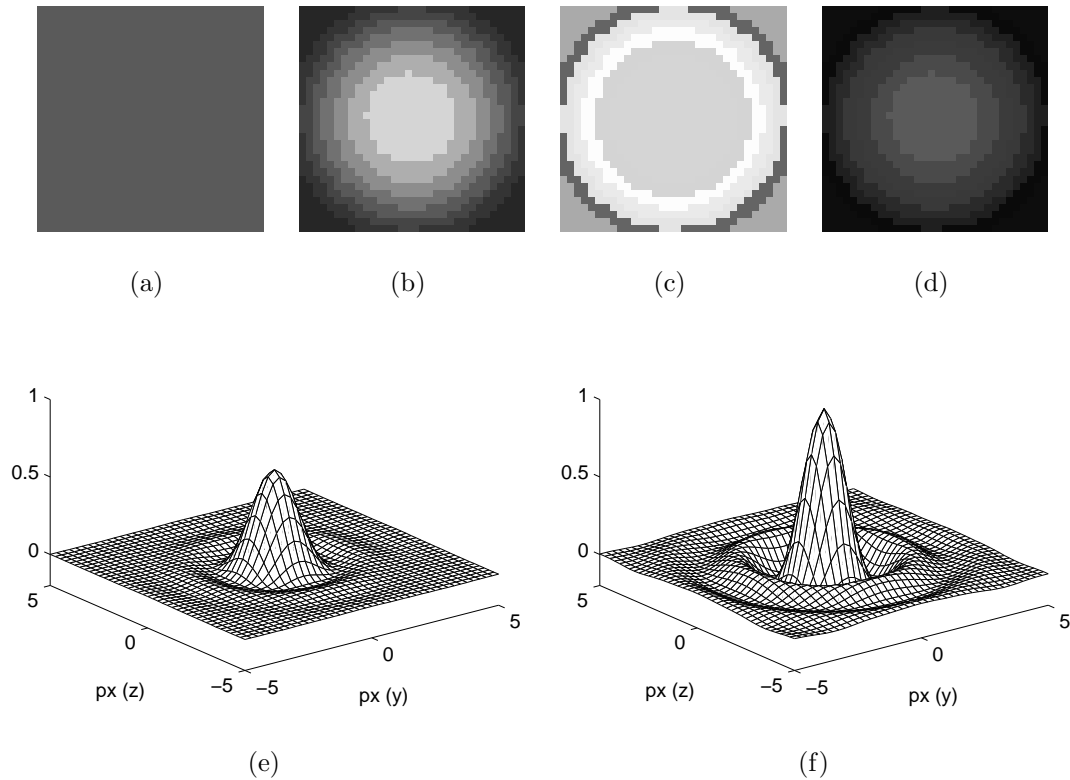


Figure 4.6: k_y - k_z space modulation (magnitude) due to a centric accelerated 3D Look-Locker acquisition for the first TI volume. (a) K-space filled with signal equal to the first post-inversion sample. (b) Modulation due to transient, $(M_{trans}(k_y, k_z)/M_{trans}(0, 0))$. (c) Modulation due to spoiling, $(M_{spoil}(k_y, k_z)/M_{trans}(k_y, k_z))$. (d) Combined effect of (b) and (c) on (a). The modulation of k -space due the transient and spoiling lead to the 2D PSFs shown in (e) and (f) respectively.

TI images would be filled in a similar fashion. This type of distortion is unavoidable by the definition of the accelerated 3D Look-Locker sequence.

Imperfect spoiling leads to coherence pathways being set up from sample to sample, and these lead to deviations from the ideally spoiled modulation, as shown in Figure 4.6(c). The combined effect of sampling along the transient and non-ideal spoiling on k -space of a point is shown in Figure 4.6(d).

The centric acquisition scheme leads to a circularly symmetric modulation of k -space due to both the transient and non-ideal spoiling. These in turn lead to circularly

symmetric PSFs as shown in Figures 4.6(e) and 4.6(f). As a consequence, the PSFs can be characterized fairly well by a one-dimensional profile. In addition to the width of the PSF leading to blurring, the area under the PSF is not necessarily unity due to the error associated with sampling the $k = 0$ line. Any deviation from unity will lead to an effective TI image with an inaccurate intensity, and will bias the T_1^* estimate.

The sources of artefact and error in the experimental data can be visualized by examining the 1D PSFs based on simulating the filling of k-space indicated by Figure 4.7. The first effective TI image is dominated by the effects of the transient. These can cause significant blurring as indicated by Figure 4.7(a), but by the last effective TI image, a perfectly spoiled transient would be nearly in steady-state, and thus the PSF due to the transient narrows.

Due to the time given for full relaxation before each inversion pulse, the first few points in the transient are only minimally affected by imperfect spoiling, leading to minimal distortion from this effect in the first effective TI image (Figure 4.7(b)). By the third effective TI image, the errors induced by quadratic spoiling are apparent. Here, the error associated with the acquisition of the centre of k-space, leads to a PSF with an area significantly greater than one for the quadratically spoiled transient, but has little affect on the random case. Both techniques also indicate some signal outside the central peak responsible for the ghosting artefacts. The eighth effective TI PSF shows the same effects due to spoiling as the third, except now the quadratically spoiled case shows a decreased area, and both show approximately the same artefact in the tails of the PSF.

4.4.4 T_1^* Error

Some of the effective TI images that were used to calculate T_1^* maps, based on sampling using 15° pulses, are shown in Figure 4.8. The locations of the samples with different T_1 values are evident from these images, as well as the surrounding saline. Since the 15° and 30° transients were acquired in an interleaved sense, the first

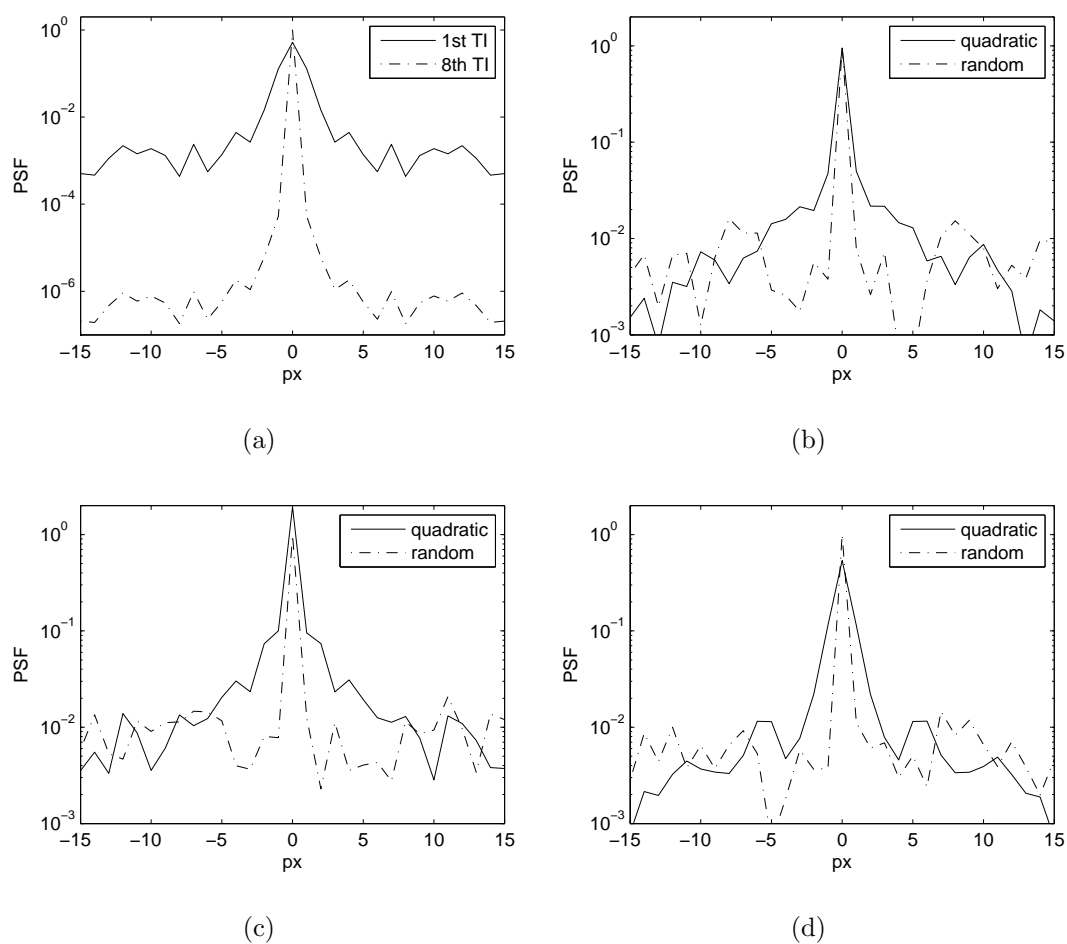


Figure 4.7: Point spread function indicating sources of error and artefact in accelerated 3D Look-Locker acquisitions. (a) The PSF due to transient effects alone for the first and last effective TI image. (b) The PSF due to spoiling effects for the first effective TI image, (c) for the third effective TI image, and (d) for the last effective TI image.

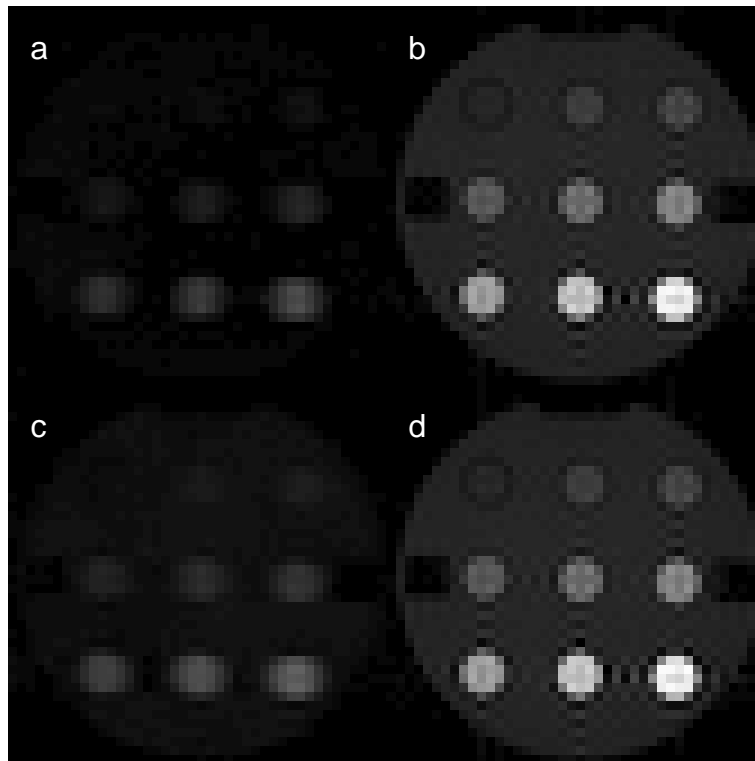


Figure 4.8: Effective TI images from a transient sampled with $N_\alpha = 48$, 15° segmented into 8 effective TI volumes. (a) and (b) are the first and last effective TI images using quadratic spoiling respectively, while (c) and (d) are the same, but randomly spoiled.

effective TI image is mostly saturated, especially the long T_1 of the saline. Sampling along the transient does lead to blurring that is evident in the first effective TI image (frequency encoding direction was vertical), but is less evident in the last effective TI image. In addition, from these images there does not appear to be a significant difference between quadratic and random spoiling.

T_1^* maps were extracted by non-linear least squares fitting of the inversion recovery equation to the eight effective TI images. These are shown Figure 4.9. In the single repetition images, the noise in the surrounding saline dominates, but the shorter T_1 samples are distinguishable. At these short repetition times and flip angles T_1^* does not depend strongly on T_1 . After 20 averages, much of the noise is removed, but there

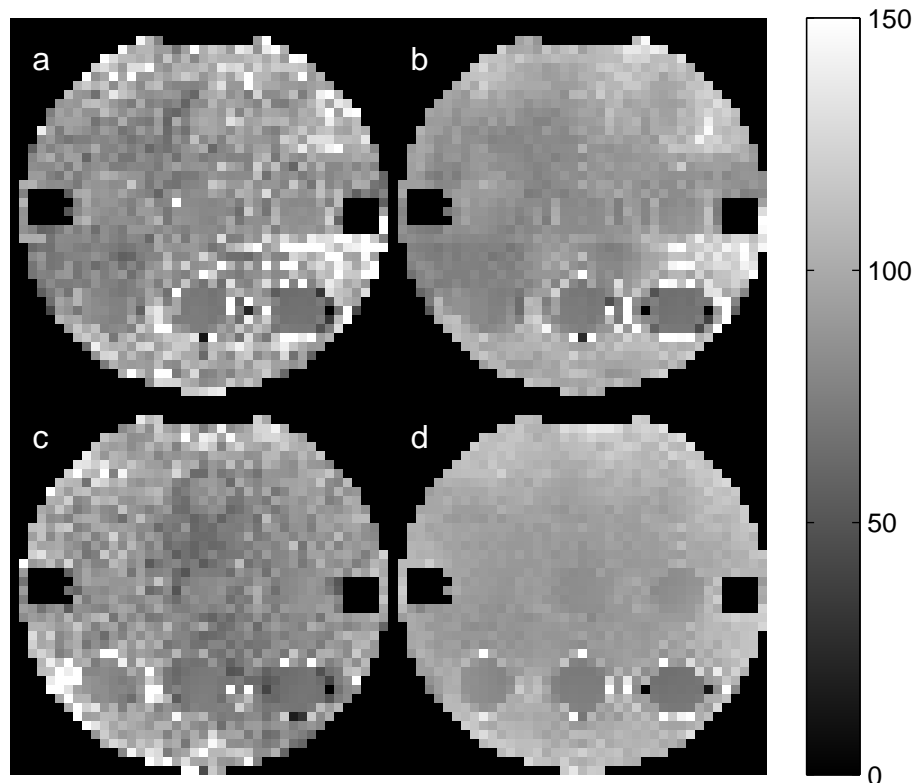


Figure 4.9: T_1^* maps (in ms) of the multi- T_1 phantom. (a) and (b) are derived from images spoiled using quadratic spoiling after (a) 1 Nex and (b) 20 Nex. (c) and (d) are based on images spoiled using random spoiling.

is still some residual artefact in the quadratically spoiled map that is less apparent in the randomly spoiled images.

The error and bias, measured using repeated measurements, introduced by the different spoiling schemes sampled using 15° pulses are quantified in Table 4.2. The random fluctuations induced by the random spoiling introduce additional noise into the T_1^* maps, as indicated by standard deviation of the T_1^* value, as compared to the measurement made with quadratic spoiling. The mean absolute error, however is only slightly worse for the randomly spoiled. This indicates that, at this lower sampling angle, the quadratic spoiling is effective, and any inaccuracies induced in the image intensities are either small or are effectively averaged out by the fitting process.

T_1 / T_1^*	T_1^*		$\sigma_{T_1^*}$		mean abs err	
	quad	rand	quad	rand	quad	rand
2952 / 105.3	91.2	105.8	11.5	29.4	16.0	21.9
1571 / 96.5	99.6	98.2	7.1	12.6	8.0	9.7
739 / 85.4	84.9	87.0	2.7	3.8	3.4	3.9
272 / 72.4	73.7	74.3	0.9	2.6	2.6	2.8

Table 4.2: Relaxation times (in ms) and errors (also in ms) measured using the accelerated 3D Look-Locker technique with $\alpha = 15^\circ$, spoiled either quadratically or randomly.

At larger flip angles, as quantified in Table 4.3, the benefit of random spoiling becomes apparent. While the noise in the T_1^* maps is still larger for the randomly spoiled transients, the mean absolute error is significantly reduced. The quadratically spoiled acquisition will consistently give an incorrect T_1^* value. Random spoiling introduces additional noise, but will still lead to a more accurate estimate of T_1^* .

T_1 / T_1^*	T_1^*		$\sigma_{T_1^*}$		mean abs err	
	quad	rand	quad	rand	quad	rand
2952 / 26.2	21.2	25.0	0.7	2.2	4.9	2.2
1571 / 24.4	20.4	24.4	0.4	1.1	4.0	1.0
739 / 22.6	19.0	22.9	0.4	0.5	3.6	0.7
272 / 21.9	18.7	22.6	0.4	0.4	3.2	0.9

Table 4.3: Relaxation times (in ms) and errors (also in ms) measured using the accelerated 3D Look-Locker technique with $\alpha = 30^\circ$, spoiled either quadratically or randomly.

If the above T_1^* maps are combined, it is possible to extract an estimate of the flip angle based on the nominal angle of $\alpha = 15^\circ$ as shown in Figure 4.10. The inaccuracy in T_1^* measurements leads to a significant overestimation of the flip angle when quadratic spoiling is employed. Random spoiling, on the other hand, indicates a fairly flat flip angle profile, which is expected in a small phantom at 3T, and has significantly reduced errors.

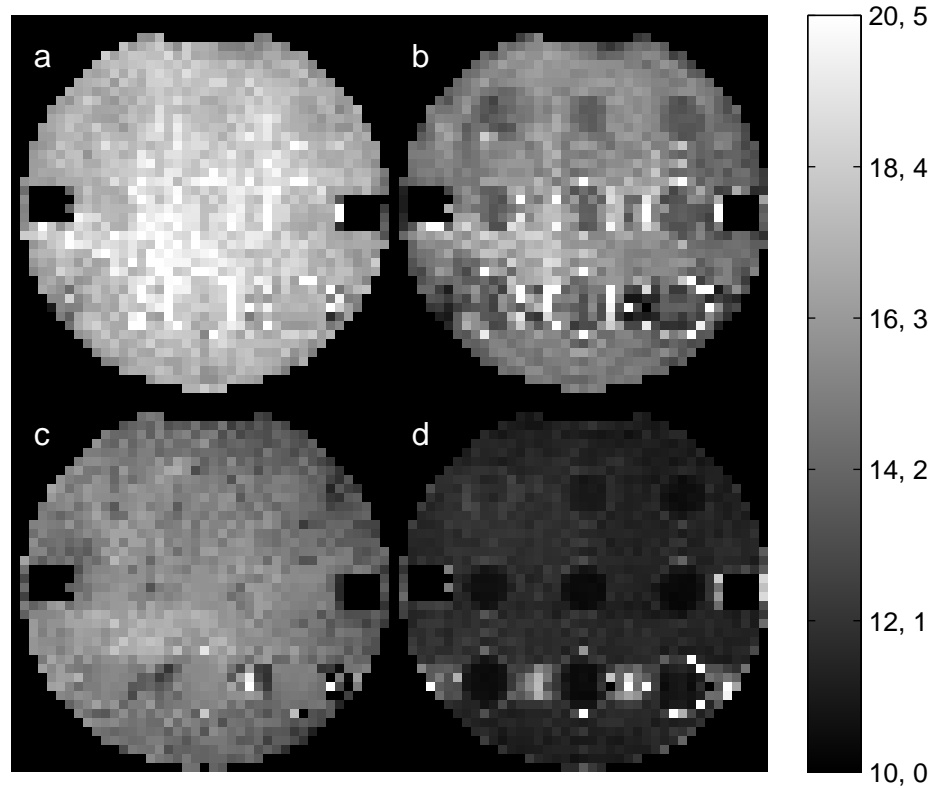


Figure 4.10: Flip angle measurement based on the DALL approach. (a) is the flip angle measured using quadratic spoiling and (b) is the mean absolute error. (c) and (d) respectively are the flip angle map and error respectively based on random spoiling. Units are degrees in the range $[10^\circ - 20^\circ]$ for flip angle maps and $[0^\circ - 5^\circ]$ for errors.

4.5 Discussion

For the validation experiments only, an additional delay was inserted between the end of one transient and the inversion to start the next. This allowed the magnetization to fully recover, and simplified the comparison between theory and experiment. In Look-Locker acquisitions it is not necessary to provide this additional delay, and the inversion to start the next transient phase can be applied immediately following the end of the former. Without the delay, coherence pathways from one train of RF pulses will contribute to the start of the next transient and introduce additional fluctuations to the first few samples, but otherwise the results remain unchanged.

It has also been suggested that large gradient moments can also be used to disrupt coherence pathways and improve spoiling through diffusion effects. These effects were not included in simulation, but were investigated experimentally by increasing the crusher moments of quadratically spoiled transients. This did lead to a decrease in the fluctuations in the transient, but still did not match the performance of the randomly spoiled transients.

For T_1 measurements, the accelerated 3D Look-Locker sequence would not normally be run with the large flip angles and short repetition times presented here. These were chosen to make the exponential curves sensitive to the flip angle for the double angle Look-Locker approach. The problem is worst at large flip angles and short repetition times, but the quadratically spoiled transients take on an erratic shape and it may be difficult to predict what effect this will have on any particular measurement of T_1^* .

4.6 Conclusion

Conventional spoiling using a quadratically increasing phase and uniform crusher gradients will lead to an inaccurate measurement of the modified relaxation coefficient T_1^* , especially with short repetition times and large flip angles. The deterministic

nature of the spoiling will lead to the same inaccurate transient with each repetition. This can lead to an inaccurate determination of T_1^* and anything derived from it. In addition, the deviations from ideal transient will lead to point spread artefacts in accelerated 3D Look-Locker imaging in addition to those induced by the transient.

A random phase and gradient spoiling scheme can overcome many of these problems. It will induce additional random fluctuations to the transient. Since these are randomly distributed about the true transient, the derived T_1^* value will be noisier but more accurate. In addition, averaging can be used to further reduce these errors and PSF artefacts, while the same is not true of quadratically spoiled transients.

References

- [1] Zur Y, Wood M, and Neuringer L. Spoiling of transverse magnetization in steady-state sequences. *Magn Reson Med* 1991;21:251–263.
- [2] Yarnykh VL. Optimal radiofrequency and gradient spoiling for improved accuracy of T_1 and B_1 measurements using fast steady-state techniques. *Magn Reson Med* 2010;63:1610–1626.
- [3] Nehrke K. On the steady-state properties of actual flip angle imaging (AFI). *Magn Reson Med* 2009;61:84–92.
- [4] Epstein FH, Mugler III JP, and Brookeman JR. Spoiling of transverse magnetization in gradient-echo (GRE) imaging during the approach to steady state. *Magn Reson Med* 1996;7:237–245.
- [5] Preibisch C and Deichmann R. Influence of RF spoiling on the stability and accuracy of T_1 mapping based on spoiled FLASH with varying flip angles. *Magn Reson Med* 2009;61:125–135.
- [6] Busse RF and Riederer SJ. Steady-state preparation for spoiled gradient echo imaging. *Magn Reson Med* 2001;45:653–661.
- [7] Freeman R and Hill H. Phase and intensity anomalies in Fourier transform NMR. *J Magn Reson* 1971;4:366–383.
- [8] Deoni SC, Rutt BK, and Peters TM. Rapid combined T_1 and T_2 mapping using gradient recalled acquisition in the steady state. *Magn Reson Med* 2003;49:515–526.
- [9] Yarnykh VL. Actual flip-angle imaging in the pulsed steady state: A method for rapid three-dimensional mapping of the transmitted radiofrequency field. *Magn Reson Med* 2007;57:192–200.

- [10] Lin W and Song HK. Improved signal spoiling in fast radial gradient-echo imaging: Applied to accurate T_1 mapping and flip angle correction. *Magn Reson Med* 2009;62:1185–1194.
- [11] Look D and Locker D. Time saving in measurement of NMR and EPR relaxation times. *Rev Sci Instrum* 1970;41:250–251.
- [12] Brix G, Schad LR, Deimling M, and Lorenz WJ. Fast and precise T_1 imaging using a TOMROP sequence. *Magn Reson Imaging* 1990;8:351–356.
- [13] Henderson E, Mckinnon G, Lee TY, and Rutt BK. A fast 3D Look-Locker method for volumetric T_1 mapping. *Magn Reson Imaging* 1999;17:1163–1171.
- [14] Hsu JJ, Zaharchuk G, and Glover GH. Rapid methods for concurrent measurement of the RF-pulse flip angle and the longitudinal relaxation time. *Magn Reson Med* 2009;61:1319–1325.
- [15] Wade T and Rutt B. B1 correction using double angle Look-Locker (DALL). In: *Proceedings of the 16th Annual Meeting of the International Society of Magnetic Resonance in Medicine, Toronto, Canada 2008*;:1246.
- [16] Crawley AP and Henkelman RM. A comparison of one-shot and recovery methods in T_1 imaging. *Magn Reson Med* 1988;7:23–43.
- [17] Nkongchu K and Santyr G. Phase-encoding strategies for optimal spatial resolution and T_1 accuracy in 3D Look-Locker imaging. *Magn Reson Imaging* 2007;25:1203–1214.
- [18] Yarnykh V. Improved accuracy of variable ip angle T_1 measurements using optimal radiofrequency and gradient spoiling. *Proceedings of the 16th Annual Meeting of ISMRM, Toronto, Ontario, Canada, 2008* ;:(Abstract 234).
- [19] Press WH, Teukolsky SA, Vetterling WT, and Flannery BP. *Numerical Recipes in C*. Cambridge University Press, New York, 2 edition, 2002.

- [20] Wilman AH and Riederer SJ. Performance of an elliptical centric view order for signal enhancement and motion artifact suppression in breath-hold three-dimensional gradient echo imaging. *Magn Reson Med* 1997;38:793–802.

Chapter 5

Discussion and Future Work

5.1 Thesis Summary

Over the course of this Thesis, a novel approach to flip angle mapping has been developed and optimized. In high field applications, especially 3 Tesla and above, knowledge of the flip angle is essential in many applications, and conventional imaging is not possible without accounting for flip angle deviations in some way. As a flip angle map would be required in addition to other protocols, a short scan is desired, especially if it is to be used to calibrate transmit B_1^+ shimming, when a flip angle image is required for each coil in a transmit array [1–5].

The Look-Locker technique presented an excellent opportunity for a fast and efficient flip angle mapping technique. It was previously shown to be an efficient technique for mapping the longitudinal recovery constant, T_1 , and had been adapted into an accelerated 3D technique. In Chapter 2, it was adapted for flip angle imaging. By acquiring the T_1^* recovery constant using either a double angle or dual repetition time approach, it became possible to derive the flip angle from the measured recovery constants. The possibility of interleaving these acquisitions to improve the dynamic range of the technique was also introduced.

The interleaved approach to data acquisition raised the novel idea that it would

be possible to sample the Look-Locker recovery curves without the need for inversion pulses. The different, interleaved α -pulse-trains act as the preparation for each other. While this would lead to a decrease in the dynamic range of the transients (and thus the accuracy of the measured flip angle if the transients are fit independently), any errors resulting from the inversion pulses would be removed, and the equations describing the decay curves would become exact, making it possible to fit directly for α .

The interleaved, non-inverted double angle Look-Locker approach is shown in Chapter 3 to be the most efficient of the Look-Locker based imaging methods. In this chapter the parameter space of the Look-Locker flip angle mapping techniques was investigated based on a theoretical propagation of noise analysis to optimize the measured α to noise in α ratio (ANR), normalized by scan time. This provided an ideal metric of efficiency by which to optimize, not only the Look-Locker based imaging methods, but also the more conventional double angle and interleaved TR (AFI) flip angle mapping techniques.

This analysis of imaging efficiency indicated that the AFI and double angle methods would suffer a significant decrease in ANR efficiency by any decrease in repetition times to achieve a short scan time. The Look-Locker based imaging methods in contrast had an efficiency that was relatively independent of restricted scan time, so that for low resolution 3D flip angle maps with scan times on the order of one minute or less, the interleaved, non-inverted DALL approach appears to be the most efficient flip angle imaging technique.

The optimization of the AFI technique also led to some unexpected results for the optimum parameters for this technique. Typically the AFI dataset is acquired with n between 4 and 6, and with flip angles between 20° and 70° . This optimization suggested that n should in fact be maximized for the given scan time (i.e. TR_1 as short as possible), and with flip angles above 110° .

The noise predicted by the propagation of noise and efficiency optimization was

validated by comparing it with the noise measured in multiple repeats of the flip angle measurement with a variety of relaxation times and imaging parameters. These results showed good agreement with the theoretical approach, but a significant bias in the flip angle measurement was noticed for the larger flip angles. This required a closer examination of the transients that were fit to find the exponential recovery constant.

These transients, particularly when large flip angles are combined with short repetition times, begin to display erratic deviations from exponential. These deviations are not due to noise, as they exist in each repetition, and do not go away with averaging. Instead, they were found to be the result of imperfect spoiling of the transverse magnetization. This phenomenon was investigated further in Chapter 4.

The conventional approach to spoiling is to use a quadratically increasing phase with a uniform amplitude crusher gradient. Provided the quadratic increase is chosen well, this will lead to a steady-state with a signal that closely matches the perfectly spoiled case for a range of parameters. While this approach makes for good qualitative steady-state images, and may be sufficient when sampling the transient with low flip angle and long repetition times, it is less than ideal for imaging during the transient phase using the larger flip angles and shorter repetition times that are optimal for the Look-Locker flip angle mapping approaches. The quadratic spoiling produces a transient that can be very non-exponential, and also varies erratically from sample to sample. This makes for inaccurate signal in the effective TI images, with degraded image quality due to the erratic deviations.

To address these issues, a random RF phase and gradient spoiling scheme was implemented for the accelerated 3D Look-Locker imaging technique. Random spoiling would lead to a signal that would never truly reach steady-state. Instead, the signal would vary from sample to sample, but with a mean value that would match the ideally spoiled value [6]. In Chapter 4, it was shown that this is an ideal property for the transient. The random spoiling produces a transient that on average will be the

ideally spoiled transient. While the variation in signal from transient to transient will be increased by the random spoiling, the root mean squared error will still be lower than if quadratic spoiling were used. This results in a T_1^* measurement that may, be more noisy, but will be more accurate.

In summary, this Thesis has introduced a unique modification to the Look-Locker approach in the form the non-inverted double angle Look-Locker imaging sequence. This technique was then optimized using both theoretical and experimental approaches, and demonstrated to be a highly efficient method of mapping the flip angle. The sampling along the Look-Locker transient required shorter repetition times and higher flip angles than conventionally used. Conventional approaches were shown to be non-ideal for spoiling in this regime, and the problem was solved by the application of a new random spoiling technique to this application, which demonstrated significant improvement. This significantly improved the dynamic range of the niDALL approach and could improve the accuracy of Look-Locker measurements in general. The developments in this Thesis have led to a technique capable of mapping the flip angle in vivo and in 3D, in scan times on the order of a minute.

5.2 Limitations of Developed Methods

5.2.1 Diffusion and Spoiling

As discussed in Chapter 4, proper spoiling of the transverse magnetization during the acquisition of the transients used in the Look-Locker flip angle mapping techniques is essential. In addition to the use of radio frequency spoiling, large gradients can be used to induce additional losses due to diffusion. The large unbalanced gradients can lead to significant disruption of the coherence pathways, and can be used as a primary source of spoiling [7,8]. The simulations used to investigate different spoiling techniques in Chapter 4 did not include this effect.

The diffusion losses could be included through a number of different analytical approaches [9, 10], or Monte Carlo simulations. This was not necessary for this work. While the experimental results indicated that diffusion would lead to some additional disruption of the coherence pathways, the random spoiling approach had a much larger influence and was more effective than any diffusion effects on the spoiling of the transients. To increase the effect of diffusion would have required much larger gradient areas which would have led to a significant increase in scan time.

5.2.2 RF Amplifier Drift

A potential source of error in the flip angle measurement, and indeed in any imaging application in which flip angle stability is required, is a drift in the flip angle over time. If the RF amplifier output were to drift over time or be non-linear, the assumption that $\alpha_2 = 2\alpha_1$ would potentially no longer be valid in double angle based flip angle measurements. It would also lead to errors in quantitative imaging techniques such as DESPOT1 and DESPOT2 that rely on flip angle accuracy [11]. The measurement of flip angle noise by the use of repeated measurements would also be corrupted by the drift in flip angle. One potential source of error would be an amplifier whose output is affected by its temperature. This could induce duty cycle and transient effects. If this were the case, it would be particularly important to map the flip angle with a technique that had a similar duty cycle to the one being corrected.

The interleaved DALL methods would be the least susceptible to RF amplifier drift, since there is minimal time for the amplifier output to change between the acquisition of the 1α and 2α transient acquisitions. However, during the acquisition of the DALL noise maps in Chapter 3, which involved the repeated measurement of the flip angle over a period of approximately 30 minutes, no trend in the flip angle was observed, indicating that the RF amplifier was indeed stable.

5.3 Future Research and Applications

5.3.1 Hyperpolarized Media T_1 Quantification

Hyperpolarized media are a special challenge in nuclear magnetic resonance experiments, and in particular imaging. Hyperpolarization allows an increase in the base magnetization that is several orders of magnitude greater than the equilibrium magnetization. This makes imaging of naturally low signal species possible. After hyperpolarization, the magnetization will decay towards its thermal equilibrium value on time scales typically on the order of tens of seconds to a few minutes. In other words, after longitudinal magnetization is tipped into the transverse plane for detection, the longitudinal magnetization will not recover to its hyperpolarized value, but only to its (much smaller) thermal polarization. This poses a particular challenge for imaging, as conventional imaging techniques using many large pulses are not applicable. Optimal use must be made of the available magnetization before it decays away. Part of this optimization process is to measure the applicable T_1 constant.

Quantification of T_1 in hyperpolarized media is a particular challenge. The conventional approach, using inversion recovery with multiple inversion time points, does not work, as the magnetization will not recover after the 90° read pulse. This is an ideal application for a Look-Locker measurement of T_1 . The low tip angle pulses will sample longitudinal magnetization as it decays towards its equilibrium value, and provided they are small and not spaced too closely, they will lead to minimal perturbation of the decay curve. This approach assumes that the transverse magnetization is effectively spoiled between the small tip angle samples. If this does not happen, it can lead to significant error in the measured T_1 .

This approach also closely mimics the typical approach to imaging hyperpolarized samples. A train of low tip angle pulses are used to acquire all the data required in the imaging, with the choice of tip angle depending very strongly on the T_1 of the particular hyperpolarized nuclei.

Currently our lab is investigating the use of contrast agents to increase the hyperpolarization of carbon-13 [12]. While these agents may improve the hyperpolarized fraction, they also typically will lead to a shortening of T_1 . This leads to a trade off between the initial magnetization and the reduced imaging time due to the shorter T_1 . It is very important to be able to measure this T_1 and the starting magnetization as it will determine the optimal imaging parameters.

Currently T_1 is measured using a 0.55 Tesla, bench-top spectrometer (Oxford Instruments). This measures the decay using a Look-Locker approach with no spoiling. The T_1 decay curve is sampled using a train of 100 nominally 5° pulses, spaced 4.9 seconds apart.

This sampling leads to decay curves such as those in Figure 5.1(a). Fitting a 3 parameter exponential ($A + (B - A) \exp(-t/T_1^*)$) to this curve using non-linear least squares fitting results in the solid line, and shows significant deviation of the experimental points from an ideal exponential, as indicated by the residuals in Figure 5.1(b). Theoretically, the curve would decay towards zero ($A = 0$), but a DC offset is frequently seen on the spectrometer. Multi-component T_1 also does not account for the significant deviation from ideal.

Using the spoiling simulation techniques developed in Chapter 4, it is possible to simulate a transient assuming no spoiling, with the free parameters T_1 , T_2 , α , M_p , and a DC offset. Here M_p is the initial hyperpolarized magnetization value, and M_0 , the equilibrium magnetization, is assumed to be zero. Fitting this simulated transient, assuming no spoiling, to the experimental data for the five free parameters results in a better fit to the transient, resulting in the reduced residuals relative to the mono-exponential fitting as indicated in Figure 5.1(b).

The results of the two fitting techniques are summarized in Table 5.1. Modelling the data using a Bloch simulation, indicates that the sample has a significant T_2 , thus some form of spoiling is required. Using the Bloch simulation also predicts a significantly greater T_1 value than predicted by fitting a mono-exponential. The root

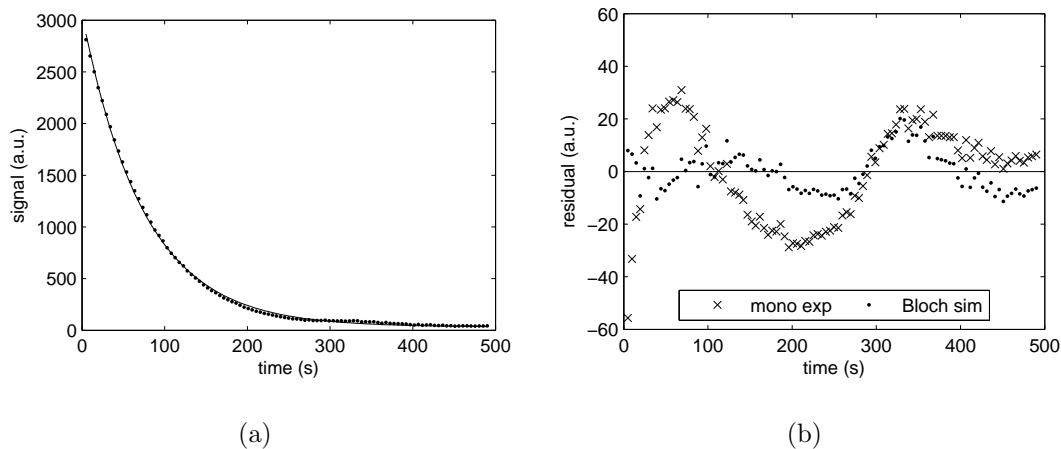


Figure 5.1: Carbon-13 Look-Locker transient and the results from two fitting approaches. (a) With a mono-exponential fit to the experimental data points, significant deviations from the model still remain. (b) The residuals after fitting either with a mono-exponential fit or based on Bloch simulations and assuming no spoiling of the transverse magnetization.

mean squared deviation (RMSD) of the experimental points from the experimental curve is also significantly lower for the simulated transient.

Fitting Technique	T_1 (s)	T_2 (s)	RMSD (a.u.)
mono-exponential	82.6 ± 1.1	N/A	18.0
Bloch simulation	86.6 ± 2.0	64.4 ± 7.2	7.6

Table 5.1: Results of fitting hyperpolarized carbon-13 Look-Locker decay curve either with a mono-exponential curve, or using Bloch simulations.

While these five parameters can be fit to a single decay curve, it is important to note that this is not a reliable approach to quantifying T_1 . It is meant to highlight the errors that can be expected if spoiling of transients is not properly done. We currently do not have the ability to quantify T_1 or T_2 in these samples, and it would be important to properly measure T_1 using an appropriate spoiling scheme. This would be a good application for randomized spoiling.

5.3.2 B_1^+ Shimming

A prime application of flip angle mapping techniques is as a calibration for and a validation of B_1^+ shimming techniques [2–5]. These require a map of the B_1^+ field for all of the elements in the transmit array. The excitation profile is then flattened by adjusting the phase and/or the amplitude of the pulses applied to each coil, or by applying custom pulses to each coil to overcome the non-uniform B_1^+ field.

Flattening the excitation profile is particularly important at 7 Tesla, and the hardware for doing this excitation is still relatively rare. Most MRI scanners below 7 Tesla do not have the parallel transmit coils and amplifiers required for these techniques. Still, a rapid B_1^+ shimming technique remains one of the major obstacles that will need to be overcome before 7 Tesla scanners become viable in the clinical environment.

References

- [1] Saekho S, Boada FE, Noll DC, and Stenger VA. Small tip angle three-dimensional tailored radiofrequency slab-select pulse for reduced B_1 inhomogeneity at 3 T. *Magn Reson Med* 2005;53:479–484.
- [2] Ibrahim TS, Lee R, Baertlein BA, Abduljalil AM, Zhu H, and Robitaille PML. Effect of RF coil excitation on field inhomogeneity at ultra high fields: a field optimized TEM resonator. *Magn Reson Imaging* 2001;19:1339–1347.
- [3] Vaughan T, DelaBarre L, Snyder C, Tian J, Akgun C, Shrivastava D, Liu W, Olson C, Adriany G, Strupp J, Andersen P, Gopinath A, van de Moortele P, Garwood M, and Ugurbil K. 9.4T human MRI: Preliminary results. *Magn Reson Med* 2006;56:1274–1282.
- [4] Katscher U, Börnert P, Leussler C, and van den Brink JS. Transmit SENSE. *Magn Reson Med* 2003;49:144–150.
- [5] Ullmann P, Junge S, Wick M, Seifert F, Ruhm W, and Hennig J. Experimental analysis of parallel excitation using dedicated coil setups and simultaneous RF transmission on multiple channels. *Magn Reson Med* 2005;54:994–1001.
- [6] Lin W and Song HK. Improved signal spoiling in fast radial gradient-echo imaging: Applied to accurate T_1 mapping and flip angle correction. *Magn Reson Med* 2009;62:1185–1194.
- [7] Yarnykh VL. Optimal radiofrequency and gradient spoiling for improved accuracy of T_1 and B_1 measurements using fast steady-state techniques. *Magn Reson Med* 2010;63:1610–1626.
- [8] Nehrke K. On the steady-state properties of actual flip angle imaging (AFI). *Magn Reson Med* 2009;61:84–92.

- [9] Kiselev V. Calculation of diffusion effect for arbitrary pulse sequences. *J Magn Reson* 2003;164:205–221.
- [10] Woessner DE. Effects of diffusion in nuclear magnetic resonance spin-echo experiments. *J Chem Phys* 1961;34:2057–2061.
- [11] Deoni SC, Rutt BK, and Peters TM. Rapid combined T_1 and T_2 mapping using gradient recalled acquisition in the steady state. *Magn Reson Med* 2003;49:515–526.
- [12] Friesen Waldner L, Scholl T, Chen A, Rutt B, and McKenzie C. The effects of contrast agents on hyperpolarized [1- ^{13}C]-pyruvic acid. Proceedings of the 18th Annual Meeting of ISMRM, Stockholm, Sweden, 2010 ;:(Abstract 3263).

Appendix A

Error Propagation

When investigating the noise propagation in different flip angle imaging techniques for the purposes of comparison and optimization, it is useful to define the dimensionless noise propagation factor:

$$b = \frac{\sigma_\alpha/\alpha}{\sigma_0/S_0} \quad (\text{A.1})$$

Where σ_0 is the noise in the raw images, and S_0 is a measure of the maximum possible signal using the desired imaging resolution and bandwidth. The flip angle and the noise in the flip angle are α and σ_α . The advantage of this approach is that the b value can be determined from a propagation of noise analysis of the signal equation or fitting required to measure the tip angle in the given technique.

Least square propagation of noise statistics gives [1]:

$$\sigma_\alpha^2 = \sum_i \left(\frac{\partial \alpha}{\partial S_i} \right)^2 \sigma_i^2 \quad (\text{A.2})$$

Where S_i are the signals that are used in the calculation of the flip angle, and σ_i are the noise in each of those images. If each image is acquired using the same imaging parameters, the noise will be constant ($\sigma_i = \sigma_0$). Since the signals can be expressed as $S_i = S_0 S'_i$, Equation A.2 becomes:

$$\sigma_\alpha^2 = \left(\frac{\sigma_0}{M_0} \right)^2 \sum_i \left(\frac{\partial \alpha}{\partial S'_i} \right)^2 \quad (\text{A.3})$$

and the noise propagation factor can be expressed as:

$$b^2 = \frac{1}{\alpha^2} \sum_i \left(\frac{\partial \alpha}{\partial S'_i} \right)^2 \quad (\text{A.4})$$

All that remains is to calculate the partial derivatives for the desired methods.

A.1 Double Angle Method

The flip angle in the Double Angle Method [2,3], whether it involves a saturation preparation or not, is given by:

$$\alpha = \arccos \left(\frac{S_{2\alpha}}{2S_\alpha} \right) \quad (\text{A.5})$$

In the conventional, fully relaxed DAM, the signals would be given by:

$$S_\alpha = S_0 \sin \alpha \quad (\text{A.6})$$

$$S_{2\alpha} = S_0 \sin 2\alpha \quad (\text{A.7})$$

and in the saturated DAM by:

$$S_\alpha = S_0 (1 - \exp(-T_{SR}/T_1)) \sin \alpha \quad (\text{A.8})$$

$$S_{2\alpha} = S_0 (1 - \exp(-T_{SR}/T_1)) \sin 2\alpha \quad (\text{A.9})$$

and thus for both DAM and satDAM:

$$\alpha = \arccos \left(\frac{S'_{2\alpha}}{2S'_\alpha} \right) \quad (\text{A.10})$$

If we set $a = S'_{2\alpha}/2S'_\alpha$, then Equation A.4 can be expanded as follows:

$$b^2 = \frac{1}{\alpha^2} \left(\frac{\partial \alpha}{\partial a} \right)^2 \left[\left(\frac{\partial a}{\partial S'_\alpha} \right)^2 + \left(\frac{\partial a}{\partial S'_{2\alpha}} \right)^2 \right] \quad (\text{A.11})$$

$$= \frac{1}{\alpha^2} \left(\frac{-1}{\sqrt{1-a^2}} \right)^2 \left[\left(\frac{-S'_{2\alpha}}{2S'^2_\alpha} \right)^2 + \left(\frac{1}{2S'_\alpha} \right)^2 \right] \quad (\text{A.12})$$

$$= \frac{1}{\alpha^2} \frac{1}{1 - (S'_{2\alpha}/2S'_\alpha)^2} \frac{1}{4S'_\alpha} \left[\left(\frac{S'_{2\alpha}}{S'_\alpha} \right)^2 + 1 \right] \quad (\text{A.13})$$

$$= \frac{1}{\alpha^2} \frac{1}{4S'^2_\alpha - S'^2_{2\alpha}} \left[\frac{S'^2_\alpha + S'^2_{2\alpha}}{S'^2_\alpha} \right] \quad (\text{A.14})$$

Substituting the expressions $S'_\alpha = \sin \alpha$ and $S'_{2\alpha} = \sin 2\alpha$ from above for the DAM, b^2 becomes:

$$b_{DAM}^2 = \frac{1}{\alpha^2} \left(\frac{1}{4 \sin^2 \alpha - \sin^2 2\alpha} \right) \left[\frac{\sin^2 \alpha + \sin^2 2\alpha}{\sin^2 \alpha} \right] \quad (\text{A.15})$$

For the saturated DAM, both S'_α and $S'_{2\alpha}$ are scaled by $(1 - \exp(-T_{SR}/T_1))$ and thus the b^2 value for satDAM is given by:

$$b_{satDAM}^2 = \frac{1}{\alpha^2} \frac{1}{(1 - \exp(-T_{SR}/T_1))^2} \frac{1}{4 \sin^2 \alpha - \sin^2 2\alpha} \left[\frac{\sin^2 \alpha + \sin^2 2\alpha}{\sin^2 \alpha} \right] \quad (\text{A.16})$$

$$= b_{DAM}^2 \frac{1}{(1 - \exp(-T_{SR}/T_1))^2} \quad (\text{A.17})$$

A.2 AFI

The tip angle in the actual flip angle imaging technique [4] is given by:

$$\alpha = \arccos \left(\frac{rn - 1}{n - r} \right) \quad (\text{A.18})$$

where $r = S_2/S_1 = S'_2/S'_1$ and $n = TR_2/TR_1$. TR_1 and TR_2 are the two interleaved repetition times, and S_1 and S_2 are the signals acquired in them.

The dimensionless noise propagation term, Equation A.4, can be expanded by setting $a = (rn - 1)/(n - r)$ as follows:

$$b^2 = \frac{1}{\alpha^2} \left(\frac{\partial \alpha}{\partial a} \frac{\partial a}{\partial r} \right)^2 \left[\left(\frac{\partial r}{\partial S'_1} \right)^2 + \left(\frac{\partial r}{\partial S'_2} \right)^2 \right] \quad (\text{A.19})$$

It is more convenient to break this down piecewise:

$$\frac{\partial \alpha}{\partial a} = \frac{-1}{\sqrt{1 - a^2}} \quad (\text{A.20})$$

$$= - \left[1 - \frac{(rn - 1)^2}{(n - r)^2} \right]^{-1/2} \quad (\text{A.21})$$

$$= - \left[\frac{n^2 - 2nr + r^2 - r^2 n^2 + 2rn - 1}{(n - r)^2} \right]^{-1/2} \quad (\text{A.22})$$

$$= - \left[\frac{(n^2 - 1)(1 - r^2)}{(n - r)^2} \right]^{-1/2} \quad (\text{A.23})$$

$$= \frac{-(n - r)}{\sqrt{(n^2 - 1)(1 - r^2)}} \quad (\text{A.24})$$

$$\frac{\partial a}{\partial r} = \left(\frac{n}{n - r} + \frac{rn - 1}{(n - r)^2} \right) \quad (\text{A.25})$$

$$= \frac{n^2 - 1}{(n - r)^2} \quad (\text{A.26})$$

$$\frac{\partial r}{\partial S'_1} = -\frac{S'_2}{S_1'^2} \quad (\text{A.27})$$

$$\frac{\partial r}{\partial S'_1} = \frac{1}{S'_1} \quad (\text{A.28})$$

and thus b^2 becomes:

$$b^2 = \frac{1}{\alpha^2} \left(\frac{-(n - r)}{\sqrt{(n^2 - 1)(1 - r^2)}} \frac{n^2 - 1}{(n - r)^2} \right)^2 \left[\left(-\frac{S'_2}{S_1'^2} \right)^2 + \left(\frac{1}{S'_1} \right)^2 \right] \quad (\text{A.29})$$

$$= \frac{1}{\alpha^2} \left(-\frac{1}{(n - r)} \sqrt{\frac{(n^2 - 1)}{(1 - r^2)}} \right)^2 \frac{1}{S_1'^2} \left[\left(\frac{S'_2}{S'_1} \right)^2 + 1 \right] \quad (\text{A.30})$$

$$= \frac{1}{\alpha^2} \frac{(r^2 + 1)(n^2 - 1)}{(n^2 - 1)(n - r)^2} \frac{1}{S_1'^2} \quad (\text{A.31})$$

where substituting the following terms:

$$r = \frac{S'_2}{S'_1} \quad (\text{A.32})$$

$$n = \frac{TR_2}{TR_1} \quad (\text{A.33})$$

$$S'_1 = \frac{1 - E_2 + (1 - E_1) E_2 \cos \alpha}{1 - E_1 E_2 \cos^2 \alpha} \sin \alpha \quad (\text{A.34})$$

$$S'_2 = \frac{1 - E_1 + (1 - E_2) E_1 \cos \alpha}{1 - E_1 E_2 \cos^2 \alpha} \sin \alpha \quad (\text{A.35})$$

$$E_1 = \exp(-TR_1/T_1) \quad (\text{A.36})$$

$$E_2 = \exp(-TR_2/T_1) \quad (\text{A.37})$$

$$(\text{A.38})$$

gives an expression for b that will depend only on the imaging parameters; TR_1 , TR_2 , α and T_1 .

A.3 Error Matrix

Statistical analysis of least squares fitting [1] yields the error matrix , $\epsilon = \beta^{-1}$, where the elements of β are given by:

$$\beta_{jk} = \sum_i \left[\frac{1}{\sigma_i^2} \frac{\partial y(x_i)}{\partial a_j} \frac{\partial y(x_i)}{\partial a_k} \right] \quad (\text{A.39})$$

where y is the function that is fit, x_i are the locations of the data points used in the fitting, σ_i is the noise in the data point at x_i and a are the parameters in the function.

For inversion recovery imaging it is convenient to express the signal equation as $y(x_i) = S(t_i) = S_0 (A + DR \exp(-t_i/T_1^*))$, and if we set $a_1 = T_1^*$, $a_2 = DR$ and $a_3 = A$, then $\sigma_{T_1^*}^2 = \epsilon_{1,1}$. Thus the partial derivatives are [5]:

$$\frac{\partial y(x_i)}{\partial a_1} = \frac{\partial S(t_i)}{\partial T_1^*} = S_0 DR \frac{t_i}{T_1^{*2}} \exp\left(-\frac{t_i}{T_1^*}\right) \quad (\text{A.40})$$

$$\frac{\partial y(x_i)}{\partial a_2} = \frac{\partial S(t_i)}{\partial DR} = S_0 \exp\left(-\frac{t_i}{T_1^*}\right) \quad (\text{A.41})$$

$$\frac{\partial y(x_i)}{\partial a_3} = \frac{\partial S(t_i)}{\partial A} = S_0 \quad (\text{A.42})$$

and by defining the terms:

$$c_{m,n} = \sum_i \left(\frac{t_i}{T_1^*} \right)^m \exp\left(-\frac{nt_i}{T_1^*}\right) \quad m, n = 0, 1, 2 \quad (\text{A.43})$$

the elements of $\beta_{i,j} = (S_0/\sigma_0)^2 \beta'_{i,j}$ are give by:

$$\begin{aligned} \beta'_{1,1} &= (DR/T_1^*)^2 c_{2,2} & \beta'_{2,2} &= c_{0,2} \\ \beta'_{1,2} = \beta'_{2,1} &= (DR/T_1^*) c_{1,2} & \beta'_{2,3} = \beta'_{3,2} &= c_{0,1} \\ \beta'_{1,3} = \beta'_{3,1} &= (DR/T_1^*) c_{2,1} & \beta'_{3,3} &= c_{0,0} \end{aligned} \quad (\text{A.44})$$

The noise in the T_1^* measurement is found by inverting the β matrix and is thus given by:

$$\sigma_{T_1^*}^2 = \left(\frac{\sigma_0 T_1^*}{S_0 DR} \right)^2 \frac{c_{0,0} c_{0,2} - c_{0,1}^2}{c_{0,0} c_{0,2} c_{2,2} + 2c_{0,1} c_{1,2} c_{2,1} - c_{0,0} c_{1,2}^2 - c_{0,1}^2 c_{2,2} - c_{0,2} c_{2,1}^2} \quad (\text{A.45})$$

From this, it is clear where the dimensionless T_1 noise propagation factor in [5], $b' = (\sigma_{T_1}/T_1) / (\sigma_0/DR)$, comes from:

$$b^* = \frac{\sigma_{T_1}/T_1}{\sigma_0/(S_0DR)} \quad (\text{A.46})$$

$$= \left(\frac{c_{0,0}c_{0,2} - c_{0,1}^2}{c_{0,0}c_{0,2}c_{2,2} + 2c_{0,1}c_{1,2}c_{2,1} - c_{0,0}c_{1,2}^2 - c_{0,1}^2c_{2,2} - c_{0,2}c_{2,1}^2} \right)^{1/2} \quad (\text{A.47})$$

A.4 Double Angle Look-Locker

The standard double angle Look Locker approach involves fitting 3 parameters to the recovery measured using a train of α pulses (A_1 , B_1 and $T_{1,1\alpha}^*$) and another 3 to the recovery measured using a train of 2α pulses (A_2 , B_2 and $T_{1,2\alpha}^*$). The the inversion recovery equation ($S(t) = A + (B - A) \exp(-t/T_1^*)$) is fit using non-linear least squares, and values $T_{1,1\alpha}^*$ and $T_{1,2\alpha}^*$ can be combined to solve for the flip angle:

$$\alpha = \arccos\left(\frac{1}{4}\left(E_\Delta + \sqrt{E_\Delta^2 + 8}\right)\right) \quad (\text{A.48})$$

with

$$E_\Delta = \exp\left(-\tau\left(\frac{1}{T_{1,2\alpha}^*} - \frac{1}{T_{1,1\alpha}^*}\right)\right) \quad (\text{A.49})$$

By setting $a = \left(\frac{1}{4}\left(E_\Delta + \sqrt{E_\Delta^2 + 8}\right)\right)$, the noise in the flip angle is given by:

$$\sigma_\alpha^2 = \left(\frac{\partial\alpha}{\partial a}\right)^2 \left[\left(\frac{\partial E_\Delta}{\partial T_{1,1\alpha}^*}\right)^2 \sigma_{T_{1,1\alpha}^*}^2 + \left(\frac{\partial E_\Delta}{\partial T_{1,2\alpha}^*}\right)^2 \sigma_{T_{1,2\alpha}^*}^2\right] \quad (\text{A.50})$$

These differentials are calculated as follows:

$$\frac{\partial\alpha}{\partial a} = \frac{-1}{\sqrt{1-a^2}} \quad (\text{A.51})$$

$$= \frac{-4}{\left(16 - \left(E_\Delta + \sqrt{E_\Delta^2 + 8}\right)^2\right)^{1/2}} \quad (\text{A.52})$$

$$= \frac{-4}{\left(8 - 2\left(E_\Delta^2 + E_\Delta\sqrt{E_\Delta^2 + 8}\right)\right)^{1/2}} \quad (\text{A.53})$$

$$\frac{\partial a}{\partial E_\Delta} = \frac{1}{4} \left(1 + \frac{E_\Delta}{\sqrt{E_\Delta^2 + 8}} \right) \quad (\text{A.54})$$

$$\frac{\partial E_\Delta}{\partial T_{1,1\alpha}^*} = \frac{-\tau}{T_{1,1\alpha}^{*2}} E_\Delta \quad (\text{A.55})$$

$$\frac{\partial E_\Delta}{\partial T_{1,2\alpha}^*} = \frac{\tau}{T_{1,2\alpha}^{*2}} E_\Delta \quad (\text{A.56})$$

And the noise in the T_1^* values can be estimated using the dimensionless T_1 noise propagation factor (b^*) from above:

$$\sigma_{T_{1,1\alpha}^*} = \frac{b_{T_{1,1\alpha}^*}^* T_{1,1\alpha}^* \sigma_0}{S_0 DR_1} \quad (\text{A.57})$$

$$\sigma_{T_{1,2\alpha}^*} = \frac{b_{T_{1,2\alpha}^*}^* T_{1,2\alpha}^* \sigma_0}{S_0 DR_2} \quad (\text{A.58})$$

Thus the noise propagation factor for the flip angle in the DALL methods is given by:

$$b^2 = \left(\frac{\sigma_\alpha / \alpha}{\sigma_0 / S_0} \right)^2 \quad (\text{A.59})$$

$$= \frac{1}{\alpha^2} \left(\frac{\partial \alpha}{\partial a} \frac{\partial a}{\partial E_\Delta} \right)^2 (\tau E_\Delta)^2 \left[\left(\frac{b_{T_{1,1\alpha}^*}^*}{DR_1 T_{1,1\alpha}^*} \right)^2 + \left(\frac{b_{T_{1,2\alpha}^*}^*}{DR_2 T_{1,2\alpha}^*} \right)^2 \right] \quad (\text{A.60})$$

with

$$\left(\frac{\partial \alpha}{\partial a} \frac{\partial a}{\partial E_\Delta} \right)^2 = \frac{\left(E_\Delta + \sqrt{E_\Delta^2 + 8} \right)^2}{2 \left(4 - E_\Delta^2 - E_\Delta \sqrt{E_\Delta^2 + 8} \right) (E_\Delta^2 + 8)} \quad (\text{A.61})$$

Where E_Δ , and the relaxation times, $T_{1,1\alpha}^*$ and $T_{1,2\alpha}^*$, are determined by τ , α , and T_1 , the relaxation times. The T_1 propagation factors, $b_{T_{1,1\alpha}^*}^*$, and $b_{T_{1,2\alpha}^*}^*$, are determined by $T_{1,1\alpha}^*$ and $T_{1,2\alpha}^*$, and times of the samples along the recovery curve. The dynamic ranges, DR_1 and DR_2 , are in turn determined by the sampling along the transient, as well as any additional relaxation times between transients and the order in which they are acquired.

A.5 Dual τ Look-Locker

The approach to D τ LL error propagation is much the same as DALL. Instead of acquiring two T_1^* values with two different flip angles, two different values for τ are used to sample the recovery, so that $\tau_2 = n\tau_1$. The flip angle is thus given by:

$$\alpha = \arccos(E_\Lambda) \quad (\text{A.62})$$

with:

$$E_\Lambda = \exp\left(-\frac{n\tau}{n-1}\left(\frac{1}{T_{1,\tau}^*} - \frac{1}{T_{1,n\tau}^*}\right)\right) \quad (\text{A.63})$$

The noise in the flip angle is thus given by:

$$\sigma_\alpha^2 = \left(\frac{\partial\alpha}{\partial E_\Lambda}\right)^2 \left[\left(\frac{\partial E_\Lambda}{\partial T_{1,\tau}^*}\right)^2 \sigma_{T_{1,\tau}^*}^2 + \left(\frac{\partial E_\Lambda}{\partial T_{1,n\tau}^*}\right)^2 \sigma_{T_{1,n\tau}^*}^2 \right] \quad (\text{A.64})$$

where the differentials are given by:

$$\frac{\partial\alpha}{\partial E_\Lambda} = \frac{-1}{\sqrt{1-E_\Lambda^2}} \quad (\text{A.65})$$

$$\frac{\partial E_\Lambda}{\partial T_{1,\tau}^*} = E_\Lambda \frac{n\tau}{n-1} \frac{1}{T_{1,\tau}^{*2}} \quad (\text{A.66})$$

$$\frac{\partial E_\Lambda}{\partial T_{1,n\tau}^*} = E_\Lambda \frac{-n\tau}{n-1} \frac{1}{T_{1,n\tau}^{*2}} \quad (\text{A.67})$$

And, as in the DALL method, the noise in the T_1^* values can be estimated using the dimensionless T_1 noise propagation factor (b^*) from error matrix approach:

$$\sigma_{T_{1,\tau}^*} = \frac{b_{T_{1,\tau}^*}^* T_{1,\tau}^* \sigma_0}{S_0 DR_1} \quad (\text{A.68})$$

$$\sigma_{T_{1,n\tau}^*} = \frac{b_{T_{1,n\tau}^*}^* T_{1,n\tau}^* \sigma_0}{S_0 DR_2} \quad (\text{A.69})$$

Combining the above, the noise propagation factor for the flip angle is given by:

$$b^2 = \frac{1}{\alpha^2} \frac{E_\Lambda^2}{1-E_\Lambda^2} \left(\frac{n\tau}{n-1}\right)^2 \left[\left(\frac{b_{T_{1,\tau}^*}^*}{DR_1 T_{1,\tau}^*}\right)^2 + \left(\frac{b_{T_{1,n\tau}^*}^*}{DR_2 T_{1,n\tau}^*}\right)^2 \right] \quad (\text{A.70})$$

Where, as in the DALL case, the parameters in b depend only on T_1 , α , τ , and n , and via the DR and b^* parameters, on the particular choice of the sampling of the transient.

A.6 Interleaved, Non-Inverted DALL

The niDALL approach to flip angle mapping differs from the conventional approaches in that rather than fitting exponentials to the two recovery curves independently, they are fit simultaneously. This requires using the error matrix approach from the start to investigate the propagation of noise into the flip angle map.

The signals from the 1α and 2α transients are:

$$S_1(t_i) = S_0 \left(A_1 + (B_1 - A_1) \exp(-t_i/T_{1,1\alpha}^*) \right) \quad (\text{A.71})$$

$$S_2(t_i) = S_0 \left(A_2 + (B_2 - A_2) \exp(-t_i/T_{1,2\alpha}^*) \right) \quad (\text{A.72})$$

with

$$\frac{1}{T_{1,1\alpha}^*} = \frac{1}{T_1} - \frac{\ln(\cos \alpha)}{\tau} \quad (\text{A.73})$$

$$\frac{1}{T_{1,2\alpha}^*} = \frac{1}{T_1} - \frac{\ln(\cos 2\alpha)}{\tau} \quad (\text{A.74})$$

$$A_1 = \frac{1 - E_\tau}{1 - E_\tau \cos \alpha} \sin \alpha \quad (\text{A.75})$$

$$A_2 = \frac{1 - E_\tau}{1 - E_\tau \cos 2\alpha} \sin 2\alpha \quad (\text{A.76})$$

$$B_1 = \frac{(\sin \alpha / \sin 2\alpha) A_2 (1 - E_{2\alpha}) + A_1 E_{2\alpha} (1 - E_{1\alpha})}{(1 - E_{1\alpha} E_{2\alpha})} \quad (\text{A.77})$$

$$B_2 = \frac{(\sin 2\alpha / \sin \alpha) A_1 (1 - E_{1\alpha}) + A_2 E_{1\alpha} (1 - E_{2\alpha})}{(1 - E_{1\alpha} E_{2\alpha})} \quad (\text{A.78})$$

$$E_{1\alpha} = \exp\left(-\frac{N_\alpha \tau}{T_{1,1\alpha}^*}\right) \quad (\text{A.79})$$

$$E_{2\alpha} = \exp\left(-\frac{N_\alpha \tau}{T_{1,2\alpha}^*}\right) \quad (\text{A.80})$$

$$E_\tau = \exp(-\tau/T_1) \quad (\text{A.81})$$

Fitting the two recovery curves simultaneously involves the minimization:

$$\min_{\alpha, T_1, S_0} = \sum_{i=1}^N \left[(S_1(t_i) - S_{i,1\alpha})^2 + (S_2(t_i) - S_{i,2\alpha})^2 \right] \quad (\text{A.82})$$

with respect to the parameters α , T_1 , and S_0 . The error matrix is thus described by:

$$\beta_{jk} = \frac{1}{\sigma_0^2} \sum_i^N \left[\frac{\partial S_1(t_i)}{\partial a_j} \frac{\partial S_1(t_i)}{\partial a_k} + \frac{\partial S_2(t_i)}{\partial a_j} \frac{\partial S_2(t_i)}{\partial a_k} \right] \quad (\text{A.83})$$

where the parameters are $a_1 = \alpha$, $a_2 = T_1$ and $a_3 = S_0$. It is impractical to solve the above by hand, and this is best done using the Symbolic Math Toolbox of Matlab.

The results are presented below:

$$\begin{aligned} \frac{\partial S_1}{\partial \alpha} = & S_0 (\cos \alpha A_1 / \sin \alpha - \sin \alpha A_1 E_\tau / (1 - \cos \alpha E_\tau)) + \\ & S_0 \left[\left\{ \cos \alpha A_2 (1 - E_{2\alpha}) / \sin 2\alpha - 2 \sin \alpha A_2 (1 - E_{2\alpha}) E_\tau / (1 - \cos 2\alpha E_\tau) + \right. \right. \\ & 2 \sin \alpha A_2 N_\alpha E_{2\alpha} / \cos 2\alpha + \cos \alpha A_1 E_{2\alpha} (1 - E_{1\alpha}) / \sin \alpha - \\ & \sin \alpha A_1 E_{2\alpha} (1 - E_{1\alpha}) E_\tau / (1 - \cos \alpha E_\tau) - \\ & 2 A_1 N_\alpha \sin 2\alpha E_{2\alpha} (1 - E_{1\alpha}) / \cos 2\alpha + \\ & \left. \left. \sin \alpha A_1 E_{2\alpha} N_\alpha / \cos \alpha E_{1\alpha} \right\} / (1 - E_{1\alpha} E_{2\alpha}) - \right. \\ & (\sin \alpha A_2 (1 - E_{2\alpha}) / \sin 2\alpha + A_1 E_{2\alpha} (1 - E_{1\alpha})) \times \\ & (N_\alpha \sin \alpha / \cos \alpha E_{1\alpha} E_{2\alpha} + 2 E_{1\alpha} N_\alpha \sin 2\alpha / \cos 2\alpha E_{2\alpha}) / (1 - E_{1\alpha} E_{2\alpha})^2 - \\ & \left. \cos \alpha A_1 / \sin \alpha + \sin \alpha A_1 E_\tau / (1 - \cos \alpha E_\tau) \right] \exp(-t_i / T_{1,1\alpha}^*) - \\ & S_0 \left\{ (\sin \alpha A_2 (1 - E_{2\alpha}) / \sin 2\alpha + A_1 E_{2\alpha} (1 - E_{1\alpha})) / (1 - E_{1\alpha} E_{2\alpha}) - A_1 \right\} \times \\ & t_i \exp(-t_i / T_{1,1\alpha}^*) \sin \alpha / \cos \alpha / \tau \end{aligned} \quad (\text{A.84})$$

$$\begin{aligned} \frac{\partial S_1}{\partial T_1} = & S_0 \left(A_1 \cos \alpha \tau E_\tau / (1 - \cos \alpha E_\tau) / T_1^2 - \sin \alpha \tau E_\tau / T_1^2 / (1 - \cos \alpha E_\tau) \right) + \\ & S_0 \left[\left\{ - \sin \alpha \tau E_\tau (1 - E_{2\alpha}) / T_1^2 / (1 - \cos 2\alpha E_\tau) + \right. \right. \\ & \sin \alpha A_2 (1 - E_{2\alpha}) \cos 2\alpha \tau E_\tau / (1 - \cos 2\alpha E_\tau) / T_1^2 / \sin 2\alpha - \\ & \sin \alpha A_2 N_\alpha \tau E_{2\alpha} / T_1^2 / \sin 2\alpha - \sin \alpha \tau E_\tau E_{2\alpha} (1 - E_{1\alpha}) / T_1^2 / (1 - \cos \alpha E_\tau) + \\ & A_1 E_{2\alpha} (1 - E_{1\alpha}) \cos \alpha \tau E_\tau / (1 - \cos \alpha E_\tau) / T_1^2 + \\ & \left. \left. A_1 N_\alpha \tau / T_1^2 E_{2\alpha} (1 - E_{1\alpha}) - A_1 E_{2\alpha} N_\alpha \tau / T_1^2 E_{1\alpha} \right\} / (1 - E_{1\alpha} E_{2\alpha}) + \right. \\ & \left. 2 (\sin \alpha A_2 (1 - E_{2\alpha}) / \sin 2\alpha + A_1 E_{2\alpha} (1 - E_{1\alpha})) N_\alpha \tau E_{1\alpha} E_{2\alpha} / (1 - E_{1\alpha} E_{2\alpha})^2 / T_1^2 + \right. \end{aligned}$$

$$\begin{aligned}
& \left. \sin \alpha \tau E_\tau / T_1^2 / (1 - \cos \alpha E_\tau) - A_1 \cos \alpha \tau E_\tau / (1 - \cos \alpha E_\tau) / T_1^2 \right] \times \\
& \exp(-t_i / T_{1,1\alpha}^*) + \\
& S_0 \left\{ (\sin \alpha A_2 (1 - E_{2\alpha}) / \sin 2\alpha + A_1 E_{2\alpha} (1 - E_{1\alpha})) / (1 - E_{1\alpha} E_{2\alpha}) - A_1 \right\} \times \\
& t_i \exp(-t_i / T_{1,1\alpha}^*) / T_1^2 \tag{A.85}
\end{aligned}$$

$$\begin{aligned}
\frac{\partial S_1}{\partial S_0} &= A_1 + ((\sin \alpha A_2 (1 - E_{2\alpha}) / \sin 2\alpha + A_1 E_{2\alpha} (1 - E_{1\alpha})) / (1 - E_{1\alpha} E_{2\alpha}) - A_1) \times \\
& \exp(-t_i / T_{1,1\alpha}^*); \tag{A.86}
\end{aligned}$$

$$\begin{aligned}
\frac{\partial S_2}{\partial \alpha} &= S_0 (2A_2 - 2 \sin 2\alpha A_2 E_\tau / (1 - \cos 2\alpha E_\tau)) + \\
& S_0 \left[\left\{ 2 \cos 2\alpha A_1 (1 - E_{1\alpha}) / \sin \alpha - \sin 2\alpha A_1 (1 - E_{1\alpha}) E_\tau / (1 - \cos \alpha E_\tau) + \right. \right. \\
& \sin 2\alpha A_1 N_\alpha E_{1\alpha} / \cos \alpha + 2A_2 E_{1\alpha} (1 - E_{2\alpha}) - \\
& 2 \sin 2\alpha A_2 E_{1\alpha} (1 - E_{2\alpha}) E_\tau / (1 - \cos 2\alpha E_\tau) - \\
& A_2 N_\alpha \sin \alpha E_{1\alpha} (1 - E_{2\alpha}) / \cos \alpha + \\
& \left. \left. 2 \sin 2\alpha A_2 E_{1\alpha} N_\alpha E_{2\alpha} / \cos 2\alpha \right\} / (1 - E_{1\alpha} E_{2\alpha}) - \right. \\
& (\sin 2\alpha A_1 (1 - E_{1\alpha}) / \sin \alpha + A_2 E_{1\alpha} (1 - E_{2\alpha})) \times \\
& (N_\alpha \sin \alpha / \cos \alpha E_{1\alpha} E_{2\alpha} + 2E_{1\alpha} N_\alpha \sin 2\alpha / \cos 2\alpha E_{2\alpha}) / (1 - E_{1\alpha} E_{2\alpha})^2 - \\
& \left. 2A_2 + 2 \sin 2\alpha A_2 E_\tau / (1 - \cos 2\alpha E_\tau) \right] \exp(-t_i / T_{1,2\alpha}^*) - \\
& 2S_0 \left\{ (\sin 2\alpha A_1 (1 - E_{1\alpha}) / \sin \alpha + A_2 E_{1\alpha} (1 - E_{2\alpha})) / (1 - E_{1\alpha} E_{2\alpha}) - A_2 \right\} \times \\
& t_i \sin 2\alpha \exp(-t_i / T_{1,2\alpha}^*) / \cos 2\alpha / \tau \tag{A.87}
\end{aligned}$$

$$\begin{aligned}
\frac{\partial S_2}{\partial T_1} &= S_0 \left(A_2 \cos 2\alpha \tau E_\tau / (1 - \cos 2\alpha E_\tau) / T_1^2 - \sin 2\alpha \tau E_\tau / T_1^2 / (1 - \cos 2\alpha E_\tau) \right) + \\
& S_0 \left[\left\{ - \sin 2\alpha \tau / T_1^2 E_\tau / (1 - \cos \alpha E_\tau) (1 - E_{1\alpha}) + \right. \right. \\
& \left. \left. \sin 2\alpha A_1 (1 - E_{1\alpha}) \cos \alpha \tau E_\tau / (1 - \cos \alpha E_\tau) / T_1^2 / \sin \alpha - \right. \right.
\end{aligned}$$

$$\begin{aligned}
& \sin 2\alpha A_1 N_\alpha \tau E_{1\alpha} / T_1^2 / \sin \alpha - \sin 2\alpha \tau / T_1^2 E_\tau / (1 - \cos 2\alpha E_\tau) E_{1\alpha} (1 - E_{2\alpha}) + \\
& A_2 E_{1\alpha} (1 - E_{2\alpha}) \cos 2\alpha \tau E_\tau / (1 - \cos 2\alpha E_\tau) / T_1^2 + \\
& A_2 N_\alpha \tau E_{1\alpha} (1 - E_{2\alpha}) / T_1^2 - A_2 E_{1\alpha} N_\alpha \tau E_{2\alpha} / T_1^2 \} / (1 - E_{1\alpha} E_{2\alpha}) + \\
& 2(\sin 2\alpha A_1 (1 - E_{1\alpha}) / \sin \alpha + A_2 E_{1\alpha} (1 - E_{2\alpha})) N_\alpha \tau E_{1\alpha} E_{2\alpha} / (1 - E_{1\alpha} E_{2\alpha})^2 / T_1^2 + \\
& \left. \sin 2\alpha \tau / T_1^2 E_\tau / (1 - \cos 2\alpha E_\tau) - A_2 \cos 2\alpha \tau E_\tau / (1 - \cos 2\alpha E_\tau) / T_1^2 \right] \times \\
& \exp(-t_i / T_{1,2\alpha}^*) + \\
& \left\{ (\sin 2\alpha A_1 (1 - E_{1\alpha}) / \sin \alpha + A_2 E_{1\alpha} (1 - E_{2\alpha})) / (1 - E_{1\alpha} E_{2\alpha}) - A_2 \right\} \times \\
& t_i \exp(-t_i / T_{1,2\alpha}^*) / T_1^2 \tag{A.88}
\end{aligned}$$

$$\begin{aligned}
\frac{\partial S_2}{\partial S_0} &= A_2 + ((\sin 2\alpha A_1 (1 - E_{1\alpha}) / \sin \alpha + A_2 E_{1\alpha} (1 - E_{2\alpha})) / (1 - E_{1\alpha} E_{2\alpha}) - A_2) \times \\
& \exp(-t_i / T_{1,2\alpha}^*) \tag{A.89}
\end{aligned}$$

From the above, the error matrix $\epsilon = \beta^{-1}$ can be found with the $\epsilon_{1,1}$ term being the noise in the flip angle, σ_α :

$$\sigma_\alpha^2 = \epsilon_{1,1} \tag{A.90}$$

$$= \frac{\beta_{2,2}\beta_{3,3} - \beta_{2,3}\beta_{3,2}}{\beta_{1,1}(\beta_{2,2}\beta_{3,3} - \beta_{2,3}\beta_{3,2}) - \beta_{1,2}(\beta_{2,1}\beta_{3,3} - \beta_{2,3}\beta_{3,1}) + \beta_{1,3}(\beta_{2,1}\beta_{3,2} - \beta_{2,2}\beta_{3,1})} \tag{A.91}$$

Upon inspection, it can be seen that a term σ_0^2 / S_0^2 can be factored out of the above, so that $\epsilon_{1,1} = \epsilon'_{1,1} \sigma_0^2 / S_0^2$. Thus the flip angle noise propagation factor can be expressed as:

$$b = \frac{\sigma_\alpha / \alpha}{\sigma_0 / S_0} \tag{A.92}$$

$$= \frac{\sqrt{\epsilon'_{1,1}}}{\alpha} \tag{A.93}$$

Thus b will depend on the sequence timings, T_1 , α and τ , and not require any *a priori* knowledge of σ_0 or S_0 .

References

- [1] Bevington PR and Robinson DK. Data Reduction and Error Analysis for the Physical Sciences. McGraw-Hill, New York, 2003.
- [2] Insko E and Bolinger L. Mapping of the radiofrequency field. J Magn Reson A 1993;103:82–85.
- [3] Cunningham CH, Pauly JM, and Nayak KS. Saturated double-angle method for rapid B_1+ mapping. Magn Reson Med 2006;55:1326–1333.
- [4] Yarnykh VL. Actual flip-angle imaging in the pulsed steady state: A method for rapid three-dimensional mapping of the transmitted radiofrequency field. Magn Reson Med 2007;57:192–200.
- [5] Crawley AP and Henkelman RM. A comparison of one-shot and recovery methods in T1 imaging. Magn Reson Med 1988;7:23–43.

Appendix B

Ethics Approval



Office of Research Ethics

The University of Western Ontario
 Room 00045 Dental Sciences Building, London, ON, Canada N6A 5C1
 Telephone: (519) 661-3036 Fax: (519) 850-2466 Email: ethics@uwo.ca
 Website: www.uwo.ca/research/ethics

Use of Human Subjects - Ethics Approval Notice

Principal Investigator: Dr. B.K. Rutt

Review Number: 10854E

Revision Number: 2

Review Date: September 24, 2007

Review Level: Expedited

Protocol Title: 3.0T MRI Software and RF Hardware Development

Department and Institution: Diagnostic Radiology & Nuclear Medicine, Robarts Research Institute

Sponsor:

Ethics Approval Date: September 24, 2007

Expiry Date: December 31, 2010

Documents Reviewed and Approved: Additional co-investigators

Documents Received for Information:

This is to notify you that The University of Western Ontario Research Ethics Board for Health Sciences Research Involving Human Subjects (HSREB) which is organized and operates according to the Tri-Council Policy Statement: Ethical Conduct of Research Involving Humans and the Health Canada/ICH Good Clinical Practice Practices: Consolidated Guidelines; and the applicable laws and regulations of Ontario has reviewed and granted approval to the above referenced revision(s) or amendment(s) on the approval date noted above. The membership of this REB also complies with the membership requirements for REB's as defined in Division 5 of the Food and Drug Regulations.

The ethics approval for this study shall remain valid until the expiry date noted above assuming timely and acceptable responses to the HSREB's periodic requests for surveillance and monitoring information. If you require an updated approval notice prior to that time you must request it using the UWO Updated Approval Request Form.

During the course of the research, no deviations from, or changes to, the protocol or consent form may be initiated without prior written approval from the HSREB except when necessary to eliminate immediate hazards to the subject or when the change(s) involve only logistical or administrative aspects of the study (e.g. change of monitor, telephone number). Expedited review of minor change(s) in ongoing studies will be considered. Subjects must receive a copy of the signed information/consent documentation.

Investigators must promptly also report to the HSREB:

- changes increasing the risk to the participant(s) and/or affecting significantly the conduct of the study;
- all adverse and unexpected experiences or events that are both serious and unexpected;
- new information that may adversely affect the safety of the subjects or the conduct of the study.

If these changes/adverse events require a change to the information/consent documentation, and/or recruitment advertisement, the newly revised information/consent documentation, and/or advertisement, must be submitted to this office for approval.

Members of the HSREB who are named as investigators in research studies, or declare a conflict of interest, do not participate in discussion related to, nor vote on, such studies when they are presented to the HSREB.

Chair of HSREB: Dr. John W. McDonald

Ethics Officer to Contact for Further Information

Jennifer McEwen (jmcewen4@uwo.ca) Denise Grafton (dgrafton@uwo.ca) Grace Kelly (gkelly2@uwo.ca)

cc: ORE File

This is an official document. Please retain the original in your files.

Curriculum Vitae

Name: Trevor P. Wade

Education

- 2006- Ph.D. Biomedical Engineering
The University of Western Ontario
London, Ontario, Canada
- 2003-2005 M.Sc. Physics
The University of British Columbia
Vancouver, British Columbia, Canada
- 1999-2003 B.Sc. Engineering Physics
Queen's University
Kingston, Ontario, Canada

Awards and Scholarships

- 2008-2010 Natural Sciences and Engineering Research Council (NSERC),
Postgraduate Scholarship, (PGS-D, \$24000/yr)
- 2006-2010 Western Graduate Research Scholarship (WGRS),
Biomedical Engineering, University of Western Ontario (\$6600/yr)
- 2003-2005 Natural Sciences and Engineering Research Council (NSERC),
Postgraduate Scholarship, (PGS-A, \$17300/yr)
- 2003 NSERC Undergraduate Student Research Award (USRA, \$4500),
Dept. of Physics, The University of British Columbia
- 2002 NSERC Undergraduate Student Research Award (USRA, \$4500),
Dept. of Chemistry, Royal Military College of Canada
- 2001 NSERC Undergraduate Student Research Award (USRA, \$4000),
Dept. of Physics, Queen's University

Related Work Experience

- 2006-2010 Graduate Teaching Assistant and Marking Coordinator (ES 1050)
Introductory Engineering Design
Dept. of Electric and Computer Engineering
The University of Western Ontario, London, Ontario
- 2009 Graduate Teaching Assistant (BME 9601)
Advanced Scientific Communication for Biomedical Engineers
Dept. of Biomedical Engineering
The University of Western Ontario, London, Ontario
- 2009 Course Designer (Phys 6001)
Physics of MRI
School of Health Sciences
Fanshawe College, London, Ontario
- 2003-2005 Graduate Teaching Assistant (Phys 100)
Introductory Physics
Dept. of Physics
The University of British Columbia, Vancouver, BC

Publications

- Vidal, A., Bureau, Y., **Wade, T.**, Spence, J.D., Rutt, B.K., Fenster, A., Parraga, G., (2008) Scan-rescan and intra-observer variability of magnetic resonance imaging of carotid atherosclerosis at 1.5 T and 3.0 T. *Phys. Med. Biol.* 53: 6821-6835 (Research Technician, before starting Ph.D.)
- Wade, T.**, and Kozlowski, P. (2007) Longitudinal Studies of Angiogenesis in Hormone-Dependent Shionogi Tumors. *Neoplasia.* 9:563-568 (M.Sc. work).

Peer Reviewed Conference Presentations

- Wade, T.**, McKenzie, C., and Rutt, B. (2010) No Inversion Double Angle Look-Locker (NiDALL) for Flip Angle. *Proceedings of the International Society for Magnetic Resonance in Medicine.* 18; 2837 (International, Poster, PhD research)
- Wade, T.**, McKenzie, C. and Rutt, B. (2010) Transient RF Spoiling for 3D Look-Locker. *Proceedings of the International Society for Magnetic Resonance in Medicine.* 18; 147 (International, Oral, PhD research)
- Wade, T.** and Rutt, B. (2009) B1 Correction Using Dual Tau Look-Locker (DLL). *Proceedings of the International Society for Magnetic Resonance in Medicine.* 17; 1246 (International, Oral, PhD research)

- Wade, T.** and Rutt, B. (2008) B1 Correction using Double Angle Look-Locker (DALL). Proceedings of the International Society for Magnetic Resonance in Medicine. 16; 1246 (International, Poster, PhD research)
- Wade, T.** and Rutt, B. (2007) Comparison of Current B1-Mapping Techniques. Proceedings of the International Society for Magnetic Resonance in Medicine. 15; 354 (International, Presentation, PhD research)
- Wade, T.**,** Heyn, C., Rutt, D., Foster, P., Rutt, B., (2006) Diffusion is a Major Determinant of Contrast in SSFP-Based Single Cell MRI: A Theoretical and Experimental Study. Proceedings of the International Society for Magnetic Resonance in Medicine. 14; 1807 (International, Poster, Research Technician at Robarts Research Institute)
- Wade, T.**** and Kozlowski, P., (2006) Longitudinal studies of angiogenesis in hormone dependent Shionogi tumours. Proceedings of the International Society for Magnetic Resonance in Medicine. 14; 2908 (International, Poster, MSc work)